NTNU – Trondheim
Norwegian University of
Science and Technology

Rock Mechanical Anisotropy, and its Impact on Borehole Stability

Thomas Paz

Petroleum Geoscience and Engineering (2 year)
Submission date: June 2014
Supervisor: Erling Fjær, IPT

Norwegian University of Science and Technology
Department of Petroleum Engineering and Applied Geophysics

Abstract

In drilling operations, small margins between wellbore collapse and hydraulic fracturing can become aggravated in anisotropic formations. A stuck pipe resulting from borehole failure can give serious economic consequences, as it may require sidetracking or even abandoning the well. The prediction of the minimum mudweight to prevent hole collapse is a complex process affected by rock properties, stress configuration and wellbore orientation. An understanding of the underlying physics, in particular on the failure models for anisotropic strength is required to combat wellbore collapse. In addition, understanding the behavior of elastic stresses for wellbore geometry is of high importance.

Existing models show that the predicted mudweight to prevent failure increases if anisotropic formation strength is assumed. The motivation and goal for this study is to achieve a greater understanding of how rock anisotropy may influence the wellbore stability.

Three strength and two stiffness models predicting behavior in transversely isotropic material have been investigated. Data from 171 compression tests on a selection of mudrocks was used to calibrate the parameters in each model. Goodness of fit analyses were conducted to determine the preferred model. Further, this model was used in predictions of shear failure in borehole stability analyses. The impact of isotropic and anisotropic stress configurations on borehole stability were studied. In addition, mudweight limits for intrinsic and structural strength anisotropy, and the difference between using strength anisotropic and strength isotropic criteria was investigated.

The mudrock selection consisted of four shales and one mudstone displaying directional anisotropy. The models in Fjær et al. (2014) were found to be preferred for the rock selection. They predicted the trends in stiffness and strength for both intrinsic and weakplane failure. The borehole stability analyses predicted higher minimum mudweight when accounting for anisotropic stresses. This effect became more pronounced when accounting for intrinsic and structural strength anisotropy.

Conclusions drawn from the study include Fjær & Nes' model being the preferred model for anisotropic strength and stiffness prediction for this rock

selection. The model was able to predict the trends in both intrinsic and structural anisotropy, suggesting that it may be used for a variety of transversely isotropic rocks. Strength anisotropy in stability analyses displayed up to 32 % higher minimum mudweight limit compared to prediction based on strength isotropy. This emphasizes the importance of accounting for rock anisotropy to prevent hole collapse in drilling operations.

Sammendrag

I boreoperasjoner kan små marginer mellom brønnkollaps og hydraulisk frakturering forverres i anisotrope formasjoner. Stuck-pipe som et resultat av brønnkollaps kan gi store økonomiske konsekvenser da dette ofte krever sidesteg eller forlating av brønnen. Prediksjon av minste slamvekt for å unngå kollaps er en kompleks prosess som påvirkes av formasjonsegenskaper, spenningskonfigurasjon og brønnens orientering. For å motvirke brønnkollaps, er det nødvendig med en dypere forståelse av den underliggende fysikken, spesielt for bruddmodellene. I tillegg er forståelse for hvordan elastiske spenninger oppfører seg for borehullsgeometri viktig.

Eksisterende modeller viser at den predikerte tillatte slamvekten øker dersom styrke anisotropi er antatt. Motivasjonen og målet med oppgaven er å undersøke hvordan formasjonsanisotropi påvirker hullstabilitet.

Tre modeller for styrke- og to modeller for stivhetsanisotropi for transversalt isotrope bergarter har blitt undersøkt. 171 kompressjonstester fra et utvalg av leirbergarter ble brukt til å kalibrere hver enkelt model. Analyser på prediksjonsnøyaktighet har blitt utført for finne en fortrukket modell. Denne modellen ble videre brukt i beregning av skjærbrudd i hullstabilitetsanalyser. Virkningen av isotrope og anisotrope spenningskonfigurasjoner på hullstabilitet har blitt studert. I tillegg har stabilitetsgrenser for indre- og strukturell styrkeanisotropi, og forskjellene mellom bruk av styrkeisotropt og -anisotropt kriterium blitt undersøkt.

Utvalget av leirbergarter bestod av fire skifer- og en leirstein som viste retningsanisotropi. Modellene i Fjær et al. (2014) ble fastslått til å være foretrukket for dette utvalget. Disse predikerte tendensen i stivhet og styrke for både indre- og strukturelle brudd. Hullstabilitetsanalysen viste forhøyet slamvektgrense for anisotrope formasjonsspenninger. Denne effekten ble mer utpreget ved inkludering av indre- og strukturell styrkeanisotropi i beregningene.

Konklusjoner fra studien inkluderer Fjær & Nes' som foretrukket prediksjonsmodell for styrke- og stivhetsanisotropi for disse leirbergartene. Modellen reproduserte tendensen for både indre og strukturelle skjærbrudd. Dette tyder på at modellen kan brukes for et vidt spekter av transversalt

isotrope bergarter. Styrkeanisotropi i hullstabilitetsanalyser viste opptil 32 % høyere minste slamvektgrense sammenlignet med prediksjon basert på styrkeisotropi. Dette understreker viktigheten av å regne med styrkeanisotropi for å unngå hullkollaps i boreoperasjoner.

Acknowledgements

The author wishes to extend his sincere gratitude to his supervisor Erling Fjær (SINTEF Petroleum Research) for the opportunity to work on this master's thesis. His patient guidance, enthusiastic encouragement and useful critiques of this work are highly appreciated.

In addition, advice given by Arnt Grøver (SINTEF Petroleum Research) on the geology related topics of this thesis has been of great help.

Finally, the author wishes to thank Katrine Paz Rossebø for the encouragement to pursue higher education. Your motivation and persistence, which has lead to the finalization of this degree and thesis, has been invaluable.

Contents

List of Figures

List of Tables

1 Introduction

When drilling a petroleum well, the borehole may collapse if the pressure in the well is too low. The collapse of a well can have serious economic consequences for the drilling operation. A stuck pipe may require cutting of the drillstring and sidetracking, increasing the cost significantly. The prediction of the minimum mudweight to prevent hole collapse is a complex process affected by rock properties, stress configuration and wellbore orientation. The complexity is increased when strength anisotropy and planes of weakness are added to the model. An understanding of the underlying physics, in particular on the rock mechanical failure models is required to combat wellbore collapse.

The motivation and goal for this study is to achieve a greater understanding of how anisotropic formation strength may influence the wellbore stability. Inverse problem theory has been used to determine parameters in anisotropic strength and stiffness criteria. The author has developed a procedure in Matlab determining the fit between an anisotropic model and experimental data. In addition, analyses on borehole stability were conducted with a new anisotropic strength model developed by SINTEF Petroleum Research. Utilizing general solutions for elastic stress with this new model, the minimum mudweight with varying wellbore inclination has been investigated. The author has developed an automated Excel spreadsheet with Visual Basics for this purpose.

Data from 171 compression tests on five mud rock samples were used to determine the parameters in five different prediction models. Three were failure criteria for anisotropic rock and two were models for prediction of stiffness. Goodness of fit analyses were used to aid in the classifying of the models according to the rock type they best described. Further, the effects of stress configuration and orientation of weak planes on wellbore collapse due to shear failure were investigated. Three cases of different stress configuration and bedding plane orientations were studied with well inclination as the variable of interest. The first case was based on isotropic stress and horizontal bedding planes. The second case included stress anisotropy, and the third case combined inclined bedding planes and stress anisotropy.

Through goodness of fit analyses, one model stood out as the preferred model for predicting strength and stiffness anisotropy. The effect of including anisotropic stresses was revealed when predicting the minimum mudweight. This effect became more pronounced when strength anisotropy and inclined weakplanes were accounted for.

A literature study was conducted prior to writing this thesis. A summary of this study is included to provide the reader insight on the models and governing equations used.

2 Theory

In this section, governing equations are presented to provide the reader insight in the models used. First, theory on Hooke's law for anisotropic material and symmetry is included. Then the selected strength and stiffness anisotropy models are introduced followed by equations used for predicting borehole stability.

2.1 Rock anisotropy

A material is said to be anisotropic if its elastic response is dependent on the material's orientation for a given stress configuration (Fjær et al. (2008), p.37). This is opposed to isotropic materials, which have the same properties in all directions. Most rocks are anisotropic both in strength and stiffness. The anisotropy is caused by rock heterogeneity on smaller scale than the rock volume in question. Its origin is usually attributed to several sub-causes like intrinsic, structural and stress induced anisotropy. Intrinsic anisotropy is associated with deposition and the preferred orientation of grains, crystal properties and variation in grain size resulting in micro structures. Structural anisotropy relates to localized, discontinuous fractures or planes of weakness. External stress anisotropy may result in micro fractures and cracks, which also can cause the rock to behave anisotropic. (Crawford et al., 2012)

2.2 Hooke's law for anisotropic material

In linear elasticity, the stress σ and strain ϵ for a material are related by Hooke's law, and is described in Equation 1.

$$\sigma_{ij} = \sum_{k,l} C_{ijkl}\epsilon_{kl} \tag{1}$$

where C_{ijkl} are elastic constants. Expanding Equation 1 will produce nine equations with nine terms each, creating a total of 81 elastic constants. The stress and

strain tensors are symmetric and is referred to as the minor symmetries (Ugural and Fenster, 1995). Voigt notaion is a way to represent a symmetric tensors (Fjær et al. (2008), p. 457). Pairs of indices are mapped into single indices, reducing the order of the tensor and improving computational efficiency. $\boldsymbol{\sigma}$ and $\boldsymbol{\epsilon}$ may be reduced to a first order tensor, and is represented using Voigt notation in Equations 2 and 3

$$\boldsymbol{\sigma} = \begin{bmatrix} \sigma_x \\ \sigma_y \\ \sigma_z \\ \tau_{yz} \\ \tau_{xz} \\ \tau_{xy} \end{bmatrix} \tag{2}$$

$$\boldsymbol{\epsilon} = \begin{bmatrix} \epsilon_x \\ \epsilon_y \\ \epsilon_z \\ 2\,\Gamma_{yz} \\ 2\,\Gamma_{xz} \\ 2\,\Gamma_{xy} \end{bmatrix} \tag{3}$$

where σ_i and τ_{ij} represent the normal and the shear stress components respectively. Similarly, ϵ_i and $2\,\Gamma_{ij}$ represent the normal and the shear strain components respectively. The arbitrariness of which the order is differentiated is called the major symmetries (Ugural and Fenster, 1995). These general symmetries require that (Fjær et al. (2008), p.38)

$$C_{ijkl} = C_{jikl} = C_{ijlk} = C_{klij} \tag{4}$$

This reduces the elastic constants to 21. The independent elastic constants may be reduced still further by assuming a type of symmetry for the material being investigated.

2.2.1 Transverse isotropy

Transverse isotropy implies that a material possesses full rotational symmetry for one axis. Any plane perpendicular to this unique axis is transversely isotropic. This means that material properties within that plane are the same in all directions. Consider the three-dimensional coordinate system for a transversely isotropic medium provided in Figure 1.

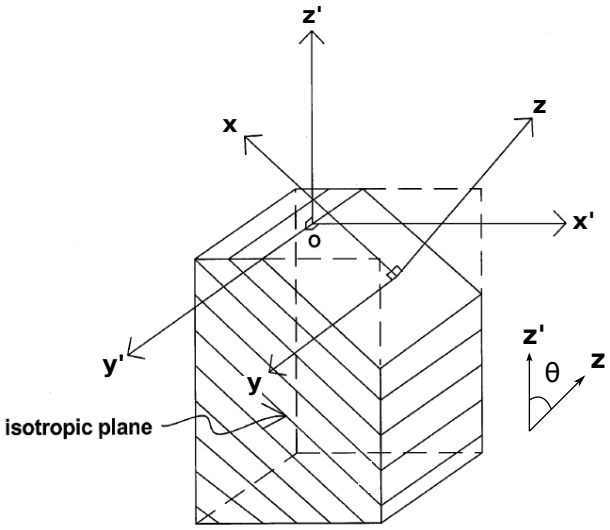

Figure 1: Coordinate systems for a transversely isotropic material. (From Tien and Kuo (2001))

The inclination θ is the angle between the major principal stress and the unique axis, represented by z' and z respectively. The principal stress coordinate system (z', y', x') is assumed to align in such a way that the intermediate principle stress y' is parallel to y. By rotating the body around y, the inclination θ is varied.

For transverse isotropy to be possible it is required that $C_{11} = C_{22}$, $C_{13} = C_{23}$, $C_{12} = C_{11} - 2\,C_{66}$ and $C_{44} = C_{55}$. This reduces the independent elastic constants to five. The stiffness tensor for a transversely isotropic material with the z-axis as the unique axis is expressed with Voigt notation in Equation 5 (Fjær et al. (2008), p. 41).

$$\boldsymbol{C} = \begin{bmatrix} C_{11} & C_{11} - 2\,C_{66} & C_{13} & 0 & 0 & 0 \\ C_{11} - 2\,C_{66} & C_{11} & C_{13} & 0 & 0 & 0 \\ C_{13} & C_{13} & C_{33} & 0 & 0 & 0 \\ 0 & 0 & 0 & C_{44} & 0 & 0 \\ 0 & 0 & 0 & 0 & C_{44} & 0 \\ 0 & 0 & 0 & 0 & 0 & C_{66} \end{bmatrix} \tag{5}$$

2.3 Transformation of the stiffness tensor

Imagine that the transversely isotropic medium described in Figure 1 is rotated around the y'-axis by the angle θ. This operation results in rotation of the structural coordinate system (x,y,z) relative to the fixed stress coordinate system (x',y',z'). The rotation of reference frames is called an elementary or basic rotation (Purdue University). For a positive elementary rotation, the right hand rule can be applied, illustrated in Figure 2 (a).

A positive rotation means that if the thumb of the right hand is pointed along the positive direction of the rotation axis, the fingers curl in the positive direction (counterclockwise). The (x,z) coordinates expressed by the (x',z') coordinates can be determined by inspection of Figure 2 (b).

$$\begin{aligned} x &= x' \cos\theta - z' \sin\theta \\ z &= z' \cos\theta + z' \cos\theta \end{aligned} \tag{6}$$

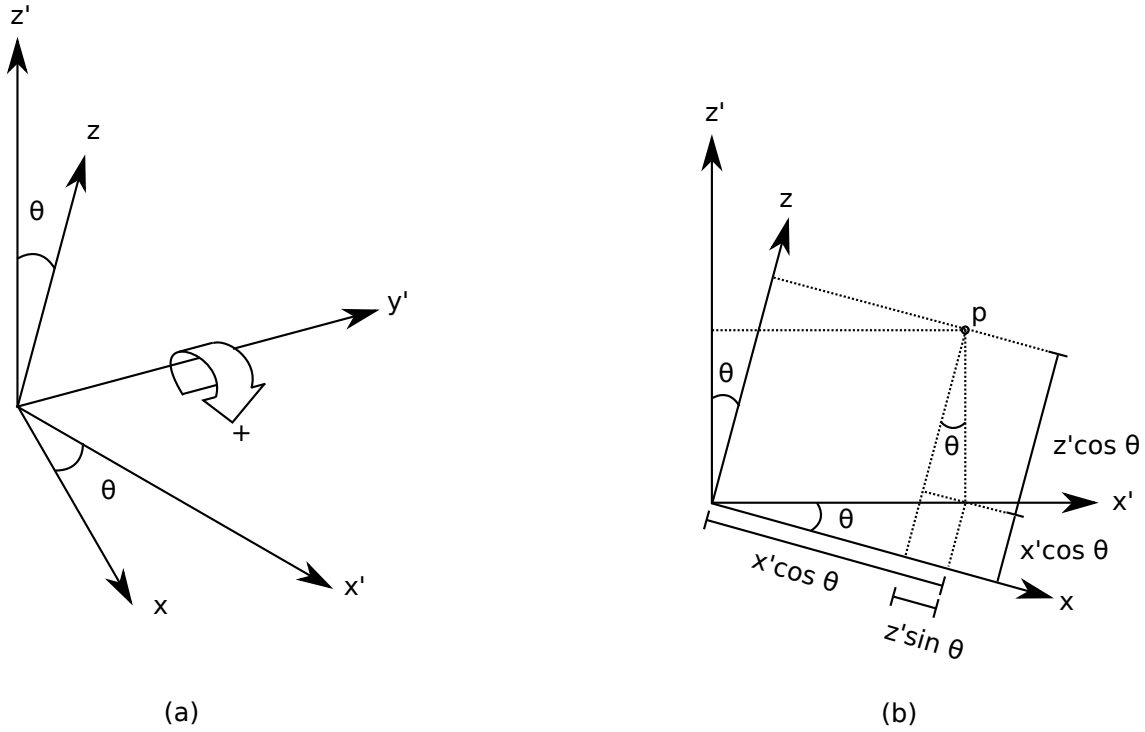

Figure 2: Elementary clockwise rotation around the y-axis using the right hand rule. (a) shows the three dimensional coordinate system and (b) shows the x-z-plane.

In matrix form, Equation 6 becomes

$$\begin{bmatrix} x \\ z \end{bmatrix} = \begin{bmatrix} \cos\theta & -\sin\theta \\ \sin\theta & \cos\theta \end{bmatrix} \begin{bmatrix} x' \\ z' \end{bmatrix} \tag{7}$$

Multiplying on the left hand side with the inverse of the matrix yields

$$\begin{bmatrix} x' \\ z' \end{bmatrix} = \begin{bmatrix} \cos\theta & -\sin\theta \\ \sin\theta & \cos\theta \end{bmatrix} \begin{bmatrix} x \\ z \end{bmatrix} \tag{8}$$

An identity transformation for the y'-coordinate is added, because it will remain unchanged during the rotation. The complete rotation matrix $\boldsymbol{R_y(\theta)}$ is now obtained as

$$\boldsymbol{R_y(\theta)} = \begin{bmatrix} \cos\theta & 0 & -\sin\theta \\ 0 & 1 & 0 \\ \sin\theta & 0 & \cos\theta \end{bmatrix} = \begin{bmatrix} l_{xx} & l_{xy} & l_{xz} \\ l_{yx} & l_{yy} & l_{yz} \\ l_{zx} & l_{zy} & l_{zz} \end{bmatrix} \tag{9}$$

where, l_{ij} are called the direction cosines. Similarly, rotation around the x' and z'-axes by the angles ϕ and β yields $\boldsymbol{R_x(\phi)}$ and $\boldsymbol{R_z(\beta)}$ respecitvely, expressed in Equations 10 and 11 (Fjær et al. (2008), p.454).

$$\boldsymbol{R_x(\phi)} = \begin{bmatrix} 1 & 0 & 0 \\ 0 & \cos\phi & \sin\phi \\ 0 & -\sin\phi & \cos\phi \end{bmatrix} \tag{10}$$

$$\boldsymbol{R_z(\beta)} = \begin{bmatrix} \cos\phi & \sin\phi & 0 \\ -\sin\phi & \cos\phi & 0 \\ 0 & 0 & 1 \end{bmatrix} \tag{11}$$

The transformation of stress $\boldsymbol{\sigma}$ and strain $\boldsymbol{\epsilon}$ tensors to a new coordinate system may be performed by the use of $\boldsymbol{R}_\sigma$ and $\boldsymbol{R}_\epsilon$. This is expressed in Equations 12 and 13 respectively.

$$\boldsymbol{\sigma}^* = \boldsymbol{R}_\sigma \boldsymbol{\sigma} \tag{12}$$

$$\boldsymbol{\epsilon}^* = \boldsymbol{R}_\epsilon \boldsymbol{\epsilon} \tag{13}$$

Substituting Equations 12 and 13 into Equation 1 and rearranging, yields the transformed stiffness tensor, expressed in Equation 14.

$$\boldsymbol{C}^* = \boldsymbol{R}_\sigma \boldsymbol{C} \boldsymbol{R}_\epsilon^{-1} \tag{14}$$

For the transformation from the coordinate system defined by $\hat{X}_j$ to the system defined by $\hat{X}_i^*$, $\boldsymbol{R}_\sigma$ becomes [1]

$$\boldsymbol{R}_\sigma = \begin{bmatrix} {l_{xx}}^2 & {l_{xy}}^2 & {l_{xz}}^2 & 2\,l_{xy}l_{xz} & 2\,l_{xx}l_{xz} & 2\,l_{xx}l_{xy} \\ {l_{yx}}^2 & {l_{yy}}^2 & {l_{yz}}^2 & 2\,l_{yy}l_{yz} & 2\,l_{yx}l_{yz} & 2\,l_{yx}l_{yy} \\ {l_{zx}}^2 & {l_{zy}}^2 & {l_{zz}}^2 & 2\,l_{zy}l_{zz} & 2\,l_{zx}l_{zz} & 2\,l_{zx}l_{zy} \\ l_{yx}l_{zx} & l_{yy}l_{zy} & l_{yz}l_{zz} & l_{yy}l_{zz}+l_{yz}l_{zy} & l_{yx}l_{zz}+l_{yz}l_{zx} & l_{yx}l_{zy}+l_{yy}l_{zx} \\ l_{xx}l_{zx} & l_{xy}l_{zy} & l_{xz}l_{zz} & l_{xy}l_{zz}+l_{xz}l_{zy} & l_{xx}l_{zz}+l_{xz}l_{zx} & l_{xx}l_{zy}+l_{xy}l_{zx} \\ l_{xx}l_{yx} & l_{xy}l_{yy} & l_{xz}l_{yz} & l_{xy}l_{yz}+l_{xz}l_{yy} & l_{xx}l_{yz}+l_{xz}l_{yx} & l_{xx}l_{yy}+l_{xy}l_{yx} \end{bmatrix} \tag{15}$$

and $\boldsymbol{R}_\epsilon$ becomes

$$\boldsymbol{R}_\epsilon = \begin{bmatrix} {l_{xX}}^2 & {l_{xY}}^2 & {l_{xZ}}^2 & 2\,l_{xY}l_{xZ} & 2\,l_{xX}l_{xZ} & 2\,l_{xX}l_{xY} \\ {l_{yX}}^2 & {l_{yY}}^2 & {l_{yZ}}^2 & 2\,l_{yY}l_{yZ} & 2\,l_{yX}l_{yZ} & 2\,l_{yX}l_{yY} \\ {l_{zX}}^2 & {l_{zY}}^2 & {l_{zZ}}^2 & 2\,l_{zY}l_{zZ} & 2\,l_{zX}l_{zZ} & 2\,l_{zX}l_{zY} \\ l_{yX}l_{zX} & l_{yY}l_{zY} & l_{yZ}l_{zZ} & l_{yY}l_{zZ}+l_{yZ}l_{zY} & l_{yX}l_{zZ}+l_{yZ}l_{zX} & l_{yX}l_{zY}+l_{yY}l_{zX} \\ l_{xX}l_{zX} & l_{xY}l_{zY} & l_{xZ}l_{zZ} & l_{xY}l_{zZ}+l_{xZ}l_{zY} & l_{xX}l_{zZ}+l_{xZ}l_{zX} & l_{xX}l_{zY}+l_{xY}l_{zX} \\ l_{xX}l_{yX} & l_{xY}l_{yY} & l_{xZ}l_{yZ} & l_{xY}l_{yZ}+l_{xZ}l_{yY} & l_{xX}l_{yZ}+l_{xZ}l_{yX} & l_{xX}l_{yY}+l_{xY}l_{yX} \end{bmatrix} \tag{16}$$

Equation 9 displays the l_{ij}-components needed in the stiffness matrix transformation. $\boldsymbol{R}_\epsilon^{-1}$ may be obtained by replacing θ with $-\theta$ for the l_{ij}-components in Equation16.

[1] Erling Fjær (SINTEF Petroleum Research). Private communication, 5^{th} of February 2014.

2.4 Failure criteria

Duveau et al. (1998) proposed a classification of different anisotropic failure criteria into three categories. The first category is the mathematical continuous models. These are based on mathematical techniques together with material symmetry where a continuous material body and continuous variation in strength is assumed. Strength tensors of different order are used to account for the anisotropy. In the second category are the empirical continuous models. They describe strength anisotropy by letting material parameters from an isotropic criterion vary with the loading orientation. Calibration with experimental data is used to determine the parameters in these criteria. The third category is the discontinuous models. These criteria are based on physical mechanisms triggering the failure of the material. It is assumed that fracture occurs either along a bedding plane or in the rock matrix. In the next sections, one model from each of the three respective categories is presented; namely the models from Cazacu et al. (1998), McLamore and Gray (1967) and Fjær and Nes (2014).

2.4.1 Cazacu et al.'s model

Cazacu et al. (1998) developed a mathematical continuous model which utilizes an isotropic criterion together with a transformed stress tensor to account for the anisotropy. In the principal stress space (σ_1,σ_2,σ_3), the criterion assumes the shape of a paraboloid. The stress tensor is based on a fourth order strength tensor, as described in Equation 17.

$$\Sigma_{ij} = A_{ijkl}\,\sigma_{kl} \tag{17}$$

Σ' is the deviatoric stress of the second order tensor Σ, expressed in Equation 18.

$$\frac{3}{2}tr(\Sigma')^2 - \frac{m}{3}tr(\Sigma) = 1 \tag{18}$$

The deviatoric stress may be obtained by subtracting the mean normal stress from the normal stress components (Fjær et al. (2008), p. 11). The strength tensor A has the general symmetry properties expressed in Equation 19.

$$A_{ijkl} = A_{klij} = A_{jikl} = A_{ijlk} \tag{19}$$

For a transversely isotropic material the strength tensor is A, expressed in Equation 20

$$\boldsymbol{A} = \begin{bmatrix} a & b & b & 0 & 0 & 0 \\ b & d & e & 0 & 0 & 0 \\ b & e & d & 0 & 0 & 0 \\ 0 & 0 & 0 & (d-e)/2 & 0 & 0 \\ 0 & 0 & 0 & 0 & c/2 & 0 \\ 0 & 0 & 0 & 0 & 0 & c/2 \end{bmatrix} \tag{20}$$

where a, b, c, d and e are independent material constants. The criterion may be expressed in terms of principal stresses, shown in Equation 21.

$$A_{11}^{'}\sigma_3^{'2} + 2\,A_{12}^{'}\sigma_3^{'}\sigma_2^{'} + 2\,A_{13}^{'}\sigma_3^{'}\sigma_1^{'} + A_{22}^{'}\sigma_2^{'2} + 2\,A_{23}^{'}\sigma_2^{'}\sigma_1^{'} + A_{33}^{'}\sigma_1^{'2} + a_1^{'}\sigma_3^{'} + a_2^{'}\sigma_2^{'} + a_3^{'}\sigma_1^{'} = 1 \tag{21}$$

Although not stated in Cazacu et al. (1998), it is implicit that the stresses are effective stresses acting on the rock's framework. The effective stress σ' is a function of Biot's coefficient α and the pore pressure p_p, given in Equation 22.

$$\sigma' = \sigma - \alpha p_p \tag{22}$$

The coefficients $A_{ij}^{'}$ and $a_{i}^{'}$ in Equation 21 are expressed in 23

$$
\begin{aligned}
A_{11}^{'} &= A_{11}\cos^4\beta + A_{22}\sin^4\beta + (2\,A_{12} + A_{55})\,\sin^2\beta\cos^2\beta \\
A_{22}^{'} &= A_{22} \\
A_{33}^{'} &= A_{11}\sin^4\beta + A_{22}\cos^4\beta + (2\,A_{12} + A_{55})\sin^2\beta\cos^2\beta \\
A_{12}^{'} &= A_{23}\sin^2\beta + A_{12}\cos^2\beta \\
A_{13}^{'} &= (A_{11} + A_{22} - A_{55} - 2\,A_{12})\sin^2\beta\cos^2\beta + A_{12} \\
A_{23}^{'} &= A_{12}\sin^2\beta + A_{23}\cos^2\beta \\
a_{1}^{'} &= a_1\cos^2\beta + a_2\sin^2\beta \\
a_{2}^{'} &= a_2 \\
a_{3}^{'} &= a_1\sin^2\beta + b_2\cos^2\beta
\end{aligned}
\tag{23}
$$

where β is the angle between the major principal stress the layers (β= $90^\circ - \theta$). The coefficients A_{ij} and a_i in 23 are expressed in 24

$$
\begin{aligned}
a_1 &= \frac{1}{X_C} - \frac{1}{X_T} \\
a_2 &= \frac{1}{Y_C} - \frac{1}{Y_T} \\
A_{11} &= \frac{1}{X_T X_C} \\
A_{22} &= \frac{1}{Y_T Y_C} \\
A_{44} &= 4A_{22} - A_{11} \\
A_{55} &= 3c^2 \\
A_{23} &= -A_{22} + \frac{A_{11}}{2} \\
A_{12} &= -\frac{1}{2}A_{11}
\end{aligned}
\tag{24}
$$

where Y_c and Y_t are the uniaxial compressive and tensile strength at $\theta = 90^\circ$.

Similarly, X_c and X_t are the uniaxial compressive and tensile strength at $\theta = 0°$.

The five parameters Y_c, X_c, Y_t, X_t and c are required in the criterion by Cazacu et al. To determine the parameters, uniaxial compression and tensile tests together with shear tests may be performed. Shear tests can be difficult to conduct and interpret. Cazacu et al. (1998) therefore recommend estimating the parameter c by least squares fit with the compression strength data for a given confining pressure. Further, since uniaxial tensile test data often is unavailable, their approach is to assume values for tensile strength seen for similar rocks. Y_c and X_c are fixed values of compressive strengths. This approach leaves c as the only free variable to be fitted to the data.

2.4.2 McLamore & Gray's model

In the empircal model by McLamore and Gray (1967), the failure envelope is described by Mohr-Coulomb shear failure theory. Strength anisotropy is described by empirical variation of material cohesion as a function of the loading angle. This criterion also utilizes continuously variable friction angle with the loading direction. The variation laws for cohesion and friction coefficient are expressed in Equations 25, 26, 27 and 28.

For $0° \leq \beta \leq \alpha_1$

$$S_0 = A_1 - B_1 \cos\,(2\,\alpha_1 - 2\,\beta)^n \tag{25}$$

For $\alpha_1 < \beta \leq 90°$

$$S_0 = A_2 - B_2 \cos\,(2\,\alpha_1 - 2\,\beta)^n \tag{26}$$

For $0° \leq \beta \leq \alpha_2$

$$\tan\,\varphi = C_1 - D_1 \cos\,(2\,\alpha_2 - 2\,\beta)^m \tag{27}$$

For $\alpha_2 < \beta \leq 90°$

$$\tan\,\varphi = C_2 - D_2 \cos\,(2\,\alpha_2 - 2\,\beta)^m \tag{28}$$

S_0 is the cohesion, $\tan\varphi$ is the coefficient of internal friction and φ is the friction angle. α_1 and α_2 are referring to the orientation β ($=90° - \theta$) where S_0 and $\tan\varphi$ are at their respective minimum. A_1, B_1, A_2 and B_2 are parameters describing the variation of cohesion with loading orientation for their respective loading intervals. Similarly, the parameters C_1, D_1, C_2 and D_2 describe the variation of the friction coefficient. m and n are called the exponents of anisotropy type.

The yield strength is predicted by the intrinsic (rock matrix) Mohr-Coulomb failure criterion, expressed in Equation 29.

$$\sigma_1' = \sigma_3' + 2\,\frac{S_0 + \sigma_3' \tan\varphi}{\sqrt{1+\tan^2\varphi} - \tan\varphi} \tag{29}$$

Substituting S_0 and $\tan\varphi$ into Equation 29 yields different expressions for the ranges of β.

The model involves a total of 10 parameters. McLamore and Gray (1967) recommend using linear extrapolation in σ_1'-σ_3' plots to obtain S_0 and $\tan\varphi$ data. Further, it is suggested to determine eight of the parameters ($A_{1,2}$, $B_{1,2}$, $C_{1,2}$ and $D_{1,2}$) by using the S_0 and $\tan\varphi$ data to calibrate Equations 25, 26, 27 and 28. Ultimately, the two remaining parameters m and n can be adjusted to account for anisotropy type. This approach leaves eight free variables to be calibrated to the data.

2.4.3 Fjær & Nes' model

The plane of patchy weakness model proposed by Fjær and Nes (2014) is a discontinuous criterion based on Mohr-Coulomb shear failure theory. Imagine that a plane of weakness is not homogenous, but contains patches of weakness. The presence of these patches results in global failure at a lower stress than if the patches did not exist. To provide a physical basis, it is assumed that the rock contains a set of closed cracks oriented parallel to the weak planes. The local stress is the critical parameter for local failure and fracture growth, which eventually causes global failure. The criteria are obtained by replacing global stress with local stress

in the failure criteria for intact rock and for the weakplanes (Fjær and Nes, 2014) (Fjær and Nes, 2013). The criterion for intrinsic failure is given in Equation 30.

$$\sigma_1' = \sigma_3' + 2(1 - \eta \sin^2 2\theta) \frac{S_0 \cos\varphi + \sigma_3' \sin\varphi}{1 - \sin\varphi} \tag{30}$$

Failure due to weakplanes is expressed with the cohesion S_{0w} and friction angle φ_w for a weak plane, and is described in Equation 31.

$$\sigma_1' = \sigma_3' + 2(1 - \eta \sin^2 2\theta) \frac{S_{0w} \cos\varphi_w + \sigma_3' \sin\varphi_w}{\sin 2\theta \cos\varphi_w - (\cos 2\theta + 1) \sin\varphi_w} \tag{31}$$

The patchiness parameter η represents the amount of weak patches in the weak plane. Because the probability for mobilization of the cracks is expected to reduce with increasing confining pressure, Equation 32 is introduced (Fjær et al., 2014).

$$\eta = \eta_0 \, e^{-\sigma_3'/\sigma_c} \tag{32}$$

η_0 is the patchiness parameter for uniaxial conditions and σ_c is a characteristic stress representing the necessary confinement for immobilization of the patches

The six parameters involved in this model are S_0, S_{0w}, φ, φ_w, η_0 and σ_c. Fjær and Nes (2013) suggest to estimate the four first parameters by linear extrapolation in σ_1'-σ_3' plots. The intrinsic criterion parameters S_0 and φ can be estimated for loading orientations 0° and 90°. Further, the weakplane criterion parameters S_{0w} and φ_w may be determined from the failure envelope where the peak strenght is lowest. This approach leaves η_0 and σ_c as free variables to be calibrated to the data.

2.5 Stiffness models

The next sections include two models for prediction of stiffness in an anisotropic material. One is offered in the plane of patchy weakness model by Fjær and Nes

(2014), and the other is the model by Backus (1962).

2.5.1 Fjær & Nes' model

Fjær and Nes (2014) also offers anisotropic stiffness prediction in the plane of patchy weakness model presented in Section 2.4.3. The proposed relationship between the effective stiffness E_{eff} and the inclination θ is described in Equation 33

$$E_{eff} = (1 - \eta \, sin^2 \, 2\theta - \rho \, cos^4 \, \theta) \, E_0 \tag{33}$$

where E_0 is the stiffness at $\theta = 90°$, and ρ is a measure of excessive normal compliance in the weak patches. Fjær and Nes (2014) suggest to use ρ as a free variable to calibrate the model with experimental data.

2.5.2 Backus' model

Backus (1962) offers a model for prediction of deformation in a horizontally layered material. Imagine a sample with i layers, each with thickness L_i. The total thickness of sample L is then the sum of each individual layer, $\sum_{i=1}^{N} L_i$. By applying an external load σ_z in a direction perpendicular to the layers, all layers must carry the same load. The deformation of layer i becomes

$$\epsilon_{z,i} = \frac{\sigma_z}{E_i} \tag{34}$$

where E_i is the stiffness of the layer i. The strain in the entire sample was defined by Backus, and is described in Equation 35.

$$\epsilon_z = \sigma_z \left\langle \frac{1}{E} \right\rangle \tag{35}$$

The angular brackets in $\langle \frac{1}{E} \rangle$ represents the average of the quantity of $\frac{1}{E}$ weighted by the volumetric portion of each layer (Backus' average). By combining Equation 35 with Hooke's law in Equation 1, the effective stiffness E_{eff} of the layered sample becomes (Fjær et al. (2008), p. 220)

$$E_{eff} = \left\langle \frac{1}{E} \right\rangle^{-1} \tag{36}$$

The sample possesses transverse isotropy, implying that the effective stress will vary with the loading orientation. The elastic constants of the material in Equation 5 then becomes (Fjær et al. (2008), p. 220-221)

$$\begin{aligned}
C_{11} &= C_{22} = \left\langle \frac{4\,G\,(\lambda + G)}{\lambda + 2\,G} \right\rangle + \left\langle \frac{1}{\lambda + 2\,G} \right\rangle^{-1} \left\langle \frac{\lambda}{\lambda + 2\,G} \right\rangle^{2} \\
C_{33} &= \left\langle \frac{1}{\lambda + 2\,G} \right\rangle^{-1} \\
C_{12} &= \left\langle \frac{2\,G\lambda}{\lambda + 2\,G} \right\rangle + \left\langle \frac{1}{\lambda + 2\,G} \right\rangle^{-1} \left\langle \frac{\lambda}{\lambda + 2\,G} \right\rangle^{2} \\
C_{13} &= C_{23} = \left\langle \frac{1}{\lambda + 2\,G} \right\rangle^{-1} \left\langle \frac{\lambda}{\lambda + 2\,G} \right\rangle \\
C_{44} &= C_{55} = \left\langle \frac{1}{G} \right\rangle^{-1} \\
C_{66} &= \langle G \rangle = \frac{1}{2}(C_{11} - C_{22})
\end{aligned} \tag{37}$$

where λ and G are elastic moduli, also called Lamé's parameters. Further, two layers with different Lamé's parameters are introduced. The parameters are related by f and g, described in Equations 38 and 39 respectively.

$$f = \frac{\lambda_2}{\lambda_1} \tag{38}$$

$$g = \frac{G_2}{G_1} \tag{39}$$

The volumetric portion x_i is related by the thickness in layer i and the total thickness $\sum_{i=1}^{n} L_i$, expressed in Equation 40.

$$x_i = \frac{L_i}{\sum_{i=1}^{n} L_i} \tag{40}$$

No suggested procedure to calibrate the model to experimental data was available.

2.6 Goodness of fit

To quantitatively determine the goodness of fit, the Residual Sum of Squares (RSS) and the degree of mismatch M may be used. In both cases, lower values indicate better fit. RSS is a measure of the error, and is expressed in Equation 41.

$$RSS = \frac{1}{N} \sum_{i=1}^{N} \left(\sigma_i^{meas} - \sigma_i^{mod} \right)^2 \tag{41}$$

The degree of mismatch is described in Equation 42 (Fjær et al. (2014))

$$M = \frac{1}{N - p - 1} \sum_{i=1}^{N} \left(\sigma_i^{meas} - \sigma_i^{mod} \right)^2 \tag{42}$$

The σ_i^{meas} and σ_i^{mod} are the measured and modelled peak stresses for observation i respectively. N is the number of observations made and p is the number of parameters used in the model. Involving the number of parameters, M indicates the relevance of the physics in a model.

2.7 Equations for borehole stability prediction

A transformation from the coordinate system (x', y', z') to (x, y, z) can be achieved by utilizing Euler's angles method. The method builds upon the rotation matrices introduced in Section 2.3. These elementary matrices may be combined to represent any three-dimensional orientation.

Using the rotation sequence z-y'-z'', the orientation of a wellbore can be related to a fixed reference frame, in this case the formation stresses (x',y',z'). z-y'-z''-rotation implies that the first rotation is around the original z-axis, and the second rotation is around the new y-axis. Similarly, the third rotation is around the new z-axis (Fjær et al. (2008), p.453). The angles corresponding to the rotation sequence z-y'-z'' are a, i and θ_B respectively, illustrated in Figure 3.

a and i are the azimuth and the inclination of the well relative to x' (σ_H) and z' (σ_V) respectively. θ_B is the azimuthal angle relative to the lowermost point on the borehole perimeter.

The full rotation is achieved by utilizing the elementary matrices in sequence, expressed in Equation 43.

$$\boldsymbol{R} = \boldsymbol{R_z}(\boldsymbol{\theta_B})\boldsymbol{R_y}(\boldsymbol{i})\boldsymbol{R_z}(\boldsymbol{a}) \tag{43}$$

For θ_B to be the azimuthal angle at the lowermost point on the borehole perimeter, θ_B must be 0. If $\theta_B = 0$, the directional matrix from Equation 43 becomes (derivation of the full rotation matrix is included in Appendix B)

$$\boldsymbol{l} = \begin{bmatrix} \cos a \cos i & \sin a \cos i & -\sin i \\ -\sin a & \cos a & 0 \\ \cos a \sin i & \sin a \sin i & \cos i \end{bmatrix} \tag{44}$$

The l_{ij}-components can now be used for determination of the stresses required in the failure criteria. The expressions for *in-situ* stresses are given in Equation 45 (Fjær et al. (2008), p.148).

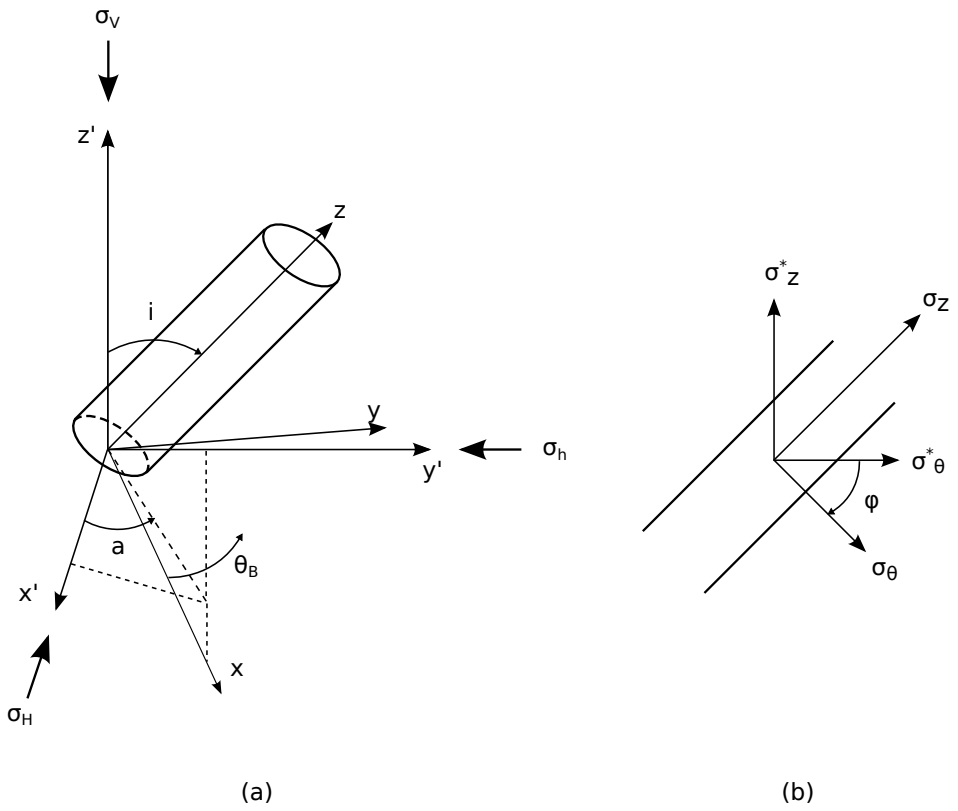

Figure 3: Illustrations of the wellbore rotated using Euler rotation matrices. Figure (a) shows the wellbore transformed from (x', y', z') to (x, y, z). (b) illustrates the rotation φ around x.

$$
\begin{aligned}
\sigma_x^o &= {l_{xx}}^2\sigma_H + {l_{xy}}^2\sigma_h + {l_{xz}}^2\sigma_V \\
\sigma_y^o &= {l_{yx}}^2\sigma_H + {l_{yy}}^2\sigma_h + {l_{yz}}^2\sigma_V \\
\sigma_z^o &= {l_{zx}}^2\sigma_H + {l_{zy}}^2\sigma_h + l_{zz}^2\sigma_V \\
\tau_{xy}^o &= l_{xx}l_{yx}\sigma_H + l_{xy}l_{yy}\sigma_h + l_{xz}l_{yz}\sigma_V \\
\tau_{yz}^o &= l_{yx}l_{zx}\sigma_H + l_{yy}l_{zy}\sigma_h + l_{yz}l_{zz}\sigma_V \\
\tau_{zx}^o &= l_{zx}l_{xx}\sigma_H + l_{zy}l_{xy}\sigma_h + l_{zz}l_{xz}\sigma_V
\end{aligned}
\tag{45}
$$

The elastic stresses at the borehole wall (Fjær et al. (2008), p.148) are expressed

in 46

$$
\begin{aligned}
\sigma_r &= p_w \\
\sigma_\theta &= \sigma_x^o + \sigma_y^o - 2\,(\sigma_x^o - \sigma_y^o)\cos(2\,\theta_B) - 4\,\tau_{xy}^o \sin(2\,\theta_B) - p_w \\
\sigma_z &= \sigma_z^o - v_{fr}[2\,(\sigma_x^o - \sigma_y^o)\cos(2\,\theta_B) + 4\,\tau_{xy}^o \sin(2\,\theta_B)] \\
\tau_{\theta z} &= 2(\,-\tau_{zx}^o \sin\theta_B + \,\tau_{yz}^o \cos\theta_B) \\
\tau_{r\theta} &= 0 \\
\tau_{rz} &= 0
\end{aligned}
\tag{46}
$$

where ν_{fr} is the Poisson's ratio. The radial stress is a principal stress when assuming failure at the borehole wall. The two other principal stresses [2] are determined using Equation 47.

$$
\begin{aligned}
\sigma_\theta^* &= \sigma_z \sin^2\phi + \sigma_\theta \cos^2\phi - \tau_{\theta z} \sin\phi \cos\phi \\
\sigma_z^* &= \sigma_z \sin^2\phi + \sigma_\theta \cos^2\phi + \tau_{\theta z} \sin\phi \cos\phi
\end{aligned}
\tag{47}
$$

For $\sigma_z \neq \sigma_\theta$, ϕ is

$$
\phi = \frac{1}{2}\arctan\left[\frac{2\tau_{\theta z}}{\sigma_z - \sigma_\theta}\right] \tag{48}
$$

For $\sigma_z = \sigma_\theta$, ϕ becomes

$$
\phi = \frac{\pi}{4} sgn\left[\tau_{\theta z}\right] \tag{49}
$$

The quasi-principal stresses used in the failure criteria may now be determined by finding the maximum and the minimum stresses, shown in 50.

[2] Erling Fjær (SINTEF Petroleum Research). Private communication, 24^{th} of March 2014.

$$\begin{aligned} \sigma_1 &= \max\{\sigma_r, \sigma_\theta^*, \sigma_z^*\} \\ \sigma_3 &= \min\{\sigma_r, \sigma_\theta^*, \sigma_z^*\} \end{aligned} \tag{50}$$

Converting the collapse pressure to mudweight (MW) can be done using Equation 51

$$\text{MW} = \frac{p_w}{gD \cdot 10^3} \tag{51}$$

where p_w is the well pressure, g is the gravitational constant and D is the true vertical depth (TVD)

3 Methods

This section explains the experimental determination of anisotropy and the basis for the selection rocks in the study. Further, methods for acquiring data and comparing the different models are described. Finally, the methods used for predicting borehole stability are explained.

3.1 Determining anisotropy experimentally

To experimentally determine the strength and stiffness anisotropy, oriented plugs are usually extracted from a larger sample, illustrated in Figure 4 (a).

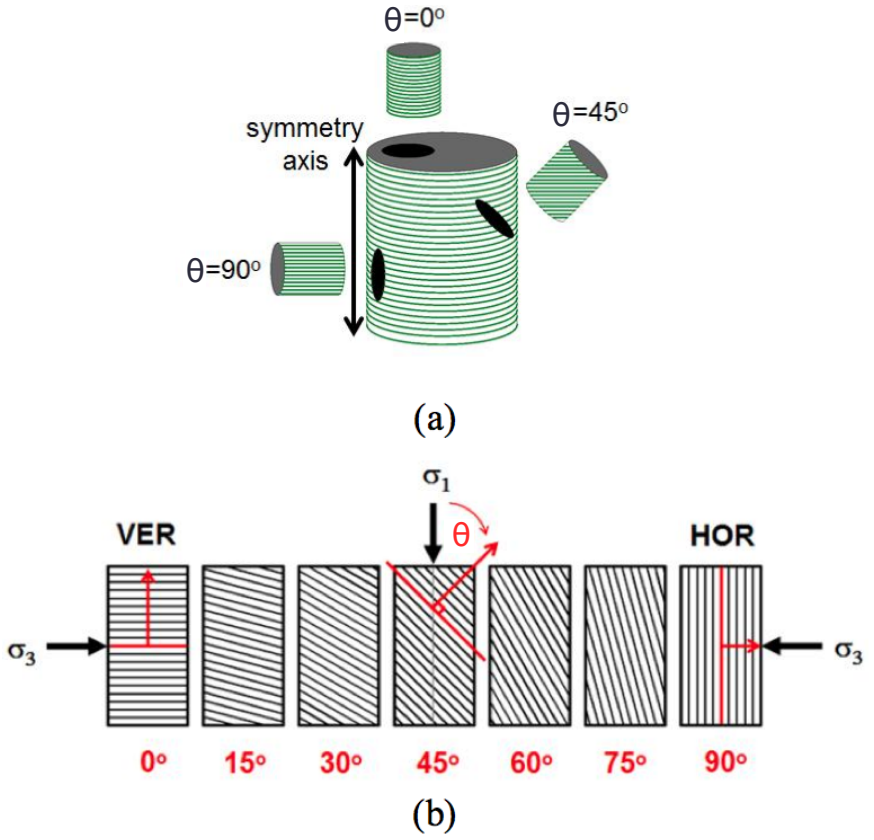

Figure 4: (a) illustrates extraction of test plugs from a larger sample. (b) shows typical compression tests with incremental weakplane inclinations of 15°. (From Crawford et al. (2012))

To quantitatively describe the strength and stiffness variation, the extracted plugs are subjected to stress at incremental angles relative to the normal of the bedding planes. 15° increments for θ are often used, requiring a total of 7 plugs, illustrated in Figure 4 (b). Increasing the confining pressure has a strengthening effect on the sample. Therefore, several sets of cored plugs may be needed to completely characterize the anisotropy.

3.2 Acquiring strength and stiffness anisotropy data

Mudrocks are likely highly abundant in the overburden of future prospects in the Norwegian Barents Sea [3]. In addition to often being weak, mudrocks display a significant strength anisotropy. Simplification by assuming isotropy can introduce unacceptable errors, which may cause inaccurate predictions of the collapse pressure. Mudrocks have for these reasons been chosen as the rock category for this study.

Test results from five different mudrock lithologies (four shales and one mudstone) were selected for investigation. The data was acquired from papers and books available in the public domain, and digitized using SINTEF Petroleum Research's Digitizer. A total of 171 compression tests were used in the anisotropic strength and stiffness analyses, and is summarized in Table 1 (The data is included in its entirety in Appendix D).

Table 1: The five lithologies used in the anisotropic strength and stiffness analyses. σ_3 is the confining presssure ranges tested, and E_0 is the stiffness for $\theta = 90°$.

Lithology	Source	Author	No. of tests [-]	σ_3 [MPa]	E_0 [GPa]
Green River shale 1	mine	McLamore & Gray	40	6.9-172	25.1
Green River shale 2	mine	McLamore & Gray	35	6.9-172	11.5
Tournemire shale	outcrop	Niandou et al.	36	5-50	33.9
Mancos shale	outcrop	Fjær & Nes	18	0-12	18.2
Mudstone	mine	Attewell & Farmer	42	0-43	-

[3] Arnt Grøver (SINTEF Petroleum Research). Private communication, 5^{th} of April 2014.

The next paragraphs include summarized rock descriptions offered in each author's work, and the respective test methods. It should be noted that test type (drained/undrained) for the anisotropic strength data is inconsistent. The implications of conducting undrained test type are discussed in Section 3.3.

The Green River shales were investigated by McLamore and Gray (1967). Green River shale 1 is described as a competent shale with a lower organic content than Green River shale 2. 40 and 35 consolidated drained tests were conducted on Green River shale 1 and 2 respectively. Both were tested with confining pressures ranging from 6.9 to 172 MPa. The tests were conducted in drained conditions and the pore pressure was set to atmospheric pressure.

Niandou (1994) studied Tournemire shale with about 8 % porosity. Its mineralogical composition was 27.5 wt% kaolinite, 16.5 wt% illite, 19 wt% quartz, 15 wt% calcite, 2.7 wt% chlorite, 8.3 wt% interstratifier and 11 wt% others. A total of 36 consolidated tests with confining pressures ranging from 5 to 50 MPa were conducted. No record of whether the tests were drained or undrained could be found.

The Mancos shale is an organic rich Cretaceous shale studied by Fjær and Nes (2013). The porosity of the rock was about 8% and the clay mineral fraction was 24%. The quartz and carbonates fractions were 43 wt% and 20 wt% respectively. A total of 18 tests were carried out, where eight plugs were tested with uniaxial conditions. In addition, some inclinations were tested with confining pressures ranging from 2 to 12 MPa. The confined tests were drained, and the pore pressure was set to be equal to atmospheric pressure.

The only mudstone included in this study was investigated by Attewell and Farmer (1976). This Carboniferous rock is described as a laminated and silty mudstone. 35 plugs were tested with confining pressure range of 3.9 to 43 MPa. Seven plugs were tested with uniaxial conditions. However, it could not be determined if the consolidated tests were conducted in drained or undrained conditions.

3.3 Failure prediction methodology

When calibrating the failure criteria to the experimental data, one should be aware of the differences in the notation and terminology used by the authors mentioned. Some define the loading orientation as the angle β between the sample layers and the principal stress. Others define the loading orientation as the angle θ between principal stress and the direction normal to the sample layers, as described in Figure 1. Another consideration is the differences in convention regarding major and minor principal stress which also varies throughout the literature. The use of σ_1 as the major principal stress has been adapted for this study.

While collecting data from the different authors, it was found that the test conditions were inconsistent. Some tests were conducted in undrained conditions and others in drained conditions. For drained conditions it means that the pore pressure in the sample can be controlled, making it an independent variable (Fjær et al. (2008), p.264). When testing with undrained conditions, the pore pressure becomes a dependent variable. The pore pressure, and consequently the effective stress can be determined using the Skempton coefficients (Fjær et al. (2008), p.35).

All the parameters in each model were used as free variables. This implies that the parameters involved were calibrated to produce the best fit with the compression data. The calibration was was done by minimizing the sum of squares using Excel's solver function.

For the criterion by Cazacu et al., the major principal stress was derived using Maple, and is included in Appendix B. Least squares fitting in Excel was used to calibrate the parameters to the data.

The McLamore & Gray model required some additional control regarding the ranges of orientation. A Matlab procedure was for this reason developed to calibrate the parameters with least squares method. The script is included in Appendix C. This model required S_0 and $\tan\varphi$ as input data. Extrapolation in peak stress and confining pressure data was done for each orientation. The intercepts and slopes $\frac{\Delta y}{\Delta x}$ of each failure envelope represent the uniaxial compressive strength C_0 and $\tan\gamma$ respectively. This is illustrated with data for Green River shale 1 in

Figure 5.

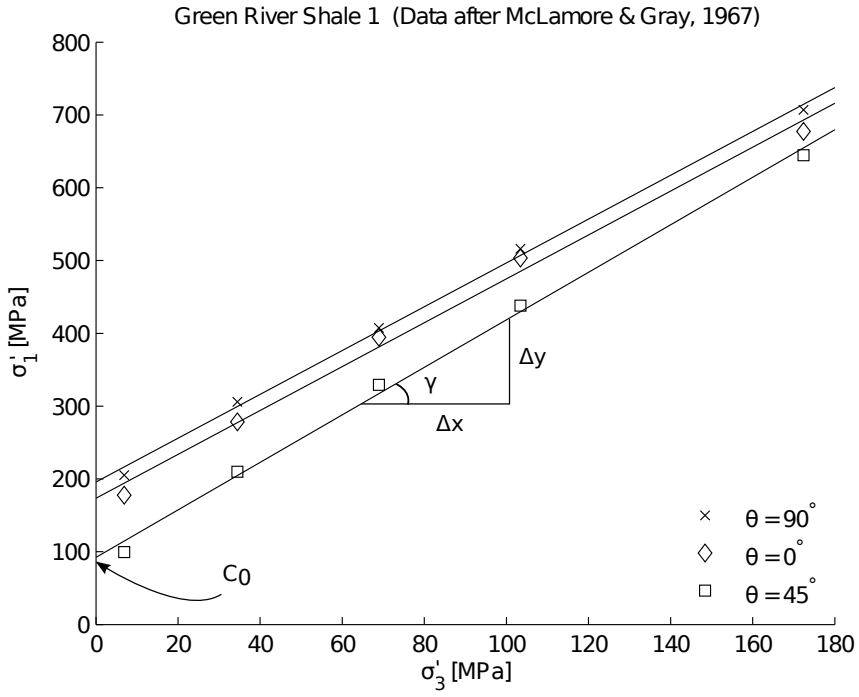

Figure 5: Extrapolation in peak stress versus confining pressure using linear least squares method exemplified for three orientations. C_0 is the intersection with σ_1 and γ is the angle between the envelope and σ_3.

S_0 and φ may be calculated using their respective relationships with C_0 and γ given in Mohr-Coulomb failure theory (Fjær et al. (2008), p.64). Their relationships are described in Equations 52 and 53 respectively.

$$S_0 = \frac{C_0(1 - \sin\varphi)}{2\cos\varphi} \tag{52}$$

$$\varphi = \arcsin\left[\frac{\tan\gamma - 1}{\tan\gamma + 1}\right] \tag{53}$$

The results were graphically reproduced using Matlab, and the scripts used are included in Appendix C. To quantitatively determine the goodness of fit between the models and the data, equations in Section 2.6 were used.

3.4 Stiffness prediction methodology

In addition to minding the authors' differences in notation for the loading direction, the effective stiffness in Backus' model had to be derived. The derivation required rotating the stiffness tensor as described in Section 2.3. The derivation of the effective stiffness was done using Maple, and is included in Appendix B.

For the Green River shales and the Tournemire shale, the anisotropic stiffness data was averaged for their respective confining pressures. For the Mancos shale, the data included was from uniaxial loading conditions. In the case of the mudstone, no data could be found. All parameters in the models were used as free variables. Least squares fitting with Excel's solver function was utilized for calibrating the models. The results were graphically reproduced using the Matlab procedures included in Appendix C. Like with the failure criteria, equations in Section 2.6 were used to determine the goodness of fit.

3.5 Borehole stability prediction methodology

Wellbore inclination is often built in or continues through mudrocks acting as the cap rock of a hydrocarbon reservoir. As the inclination increases, the effect of the overburden stress on the wellbore wall increases too, making the wellbore less stable. Consequently, higher mudweight to prevent borehole failure is required. This effect can become more pronounced when accounting for intrinsic and structural anisotropy in laminated rocks. Therefore it is be relevant to consider strength anisotropy when predicting the collapse pressure.

The anisotropic plane of patchy weakness model by Fjær et al. (2014) was selected for prediction of shear failure in borehole stability. The model was under development at the time of writing, and was redefined to account for the intermediate principal stress. The intrinsic and weakplane criteria [4] used in predicting borehole stability are given in Equations 54 and 55 respectively.

[4] Erling Fjær (SINTEF Petroleum Research). Private communication, 26^{th} of May 2014.

$$\Delta\sigma_{F,intrinsic}^{shear} = \sigma_1' - \sigma_3' - \Big[2(1-\eta\sin^2 2\theta)\frac{S_0\cos\varphi + \sigma_3'\sin\varphi}{1-\sin\varphi} + \eta\sin^2 2\theta\cos^2\Phi(\sigma_2' - \sigma_3')\Big] \tag{54}$$

$$\Delta\sigma_{F,wp}^{shear} = \sigma_1' - \sigma_3' - \Big[2(1-\eta\sin^2 2\theta)\frac{S_{0w}\cos\varphi_w + \sigma_3'\sin\varphi_w}{\sin 2\theta\cos\varphi_w - (\cos 2\theta + 1)\sin\varphi_w} + \eta\sin^2 2\theta\cos^2\Phi(\sigma_2' - \sigma_3')\Big] \tag{55}$$

Φ is the angle between $\hat{\boldsymbol{\sigma}}_{\mathbf{3}}$ and the intercept between the weak planes and the $\hat{\boldsymbol{\sigma}}_{\mathbf{2}}$,$\hat{\boldsymbol{\sigma}}_{\mathbf{3}}$-plane, illustrated in Figure 6.

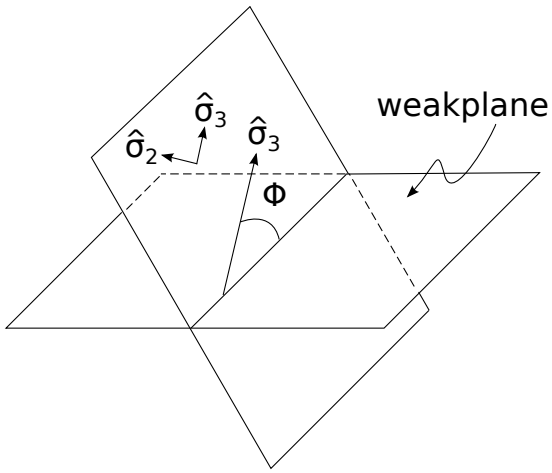

Figure 6: Illustration showing the angle Φ and a weakplane intercepting with the intermediate and minor principal axis plane.

Shear failure occurs if $\Delta\sigma_F^{shear} \geq 0$. $\cos\Phi$ is the inner product of $\hat{\boldsymbol{s}}$ and $\hat{\boldsymbol{\sigma}}_{\mathbf{3}}$, expressed in Equation 56.

$$\cos\Phi = \hat{\boldsymbol{s}} \cdot \hat{\boldsymbol{\sigma}}_{\mathbf{3}} \tag{56}$$

$\hat{\boldsymbol{s}}$ is the cross product of the $\hat{\boldsymbol{\sigma}}_{\mathbf{1}}$ and the normal unit vector $\hat{\boldsymbol{n}}$ of the weakplane,

given in Equation 57.

$$\hat{\boldsymbol{s}} = \hat{\boldsymbol{\sigma}}_{\mathbf{1}} \times \hat{\boldsymbol{n}} \tag{57}$$

The normal unit vector $\hat{\boldsymbol{n}}$ of the weakplane is expressed in Equation 58

$$\hat{\boldsymbol{n}} = \begin{bmatrix} \sin i_w \cos a_w & \sin i_w \sin a_w & \cos i_w \end{bmatrix} \tag{58}$$

where i_w and a_w are inclination and azimuth of the weakplane relative to the horizontal plane and σ_H respectively. $\hat{\boldsymbol{\sigma}}_{\mathbf{1}}$ can be either of the unit vectors $\hat{\boldsymbol{\sigma}}_{\boldsymbol{\theta}}$ or $\hat{\boldsymbol{\sigma}}_{\boldsymbol{z}}$, depending on which one is the major principal stress (see Equation 50). The respective $\cos\Phi_\theta$ and $\cos\Phi_z$ are expressed in Equations 59 and 60.

$$\begin{aligned}\cos\Phi_\theta = {} & (\sin a \sin a_w + \cos a \cos a_w)[\cos\phi \sin i \sin i_w - \sin\theta_B \cos i \sin\phi \sin i_w] \\ & + \sin\phi \cos\theta_B \sin i_w (\cos a \sin a_w - \sin a \cos a_w) \\ & + \cos i_w (\sin\theta_B \sin\phi \sin i + \cos\phi \cos i)\end{aligned} \tag{59}$$

$$\begin{aligned}\cos\Phi_z = {} & (\sin a \sin a_w + \cos a \cos a_w)[\cos\phi \sin\theta_B \cos i \sin i_w + \sin\phi \sin i \sin i_w] \\ & + \cos\phi \cos\theta_B \sin i_w (\sin a \cos a_w - \cos a \sin a_w) \\ & + \cos i_w (\cos i \sin\phi - \cos\phi \sin\theta_B \sin i)\end{aligned} \tag{60}$$

$\cos\theta$ is the inner product of $\hat{\boldsymbol{\sigma}}_{\mathbf{1}}$ and the normal unit vector $\hat{\boldsymbol{n}}$ of the weakplane, shown in Equation 61.

$$\cos\theta = \hat{\boldsymbol{\sigma}}_{\mathbf{1}} \cdot \hat{\boldsymbol{n}} \tag{61}$$

Similar to $\cos\Phi$, $\hat{\boldsymbol{\sigma}}_{\mathbf{1}}$ can either be $\hat{\boldsymbol{\sigma}}_{\boldsymbol{\theta}}$ or $\hat{\boldsymbol{\sigma}}_{\boldsymbol{z}}$. To avoid confusion, the angle between the major principal stress and the normal of the weakplane θ is substituted with Ψ. The respective $\cos\Psi_\theta$ and $\cos\Psi_z$ are expressed in Equations 62 and 63.

$$\begin{aligned}\cos\Psi_\theta = &-\sin i_w \cos a_w[\cos a(\sin\phi\sin i + \cos\phi\sin\theta\cos i) + \sin a\cos\phi\cos\theta] \\ &-\sin i_w \sin a_w[\sin a(\sin\phi\sin i + \cos\phi\sin\theta\cos i) - \cos a\ \cos\phi\cos\theta] \\ &+\cos i_w(\cos\phi\sin\theta\sin i - \sin\phi\cos i)\end{aligned} \tag{62}$$

$$\begin{aligned}\cos\Psi_z = &\sin i_w \cos a_w[\cos a(\cos\phi\sin i - \sin\phi\sin\theta\cos i) - \sin a\sin\phi\cos\theta] \\ &+\sin i_w \sin a_w[\sin a(\cos\phi\sin i - \sin\phi\sin\theta\cos i) + \cos a\ \sin\phi\cos\theta] \\ &+\cos i_w(\sin\phi\sin\theta\sin i + \cos\phi\cos i)\end{aligned} \tag{63}$$

The derivations of $\cos\Phi_\theta$, $\cos\Phi_z$, $\cos\Psi_\theta$ and $\cos\Psi_z$ was done in Maple using Euler's angles (Fjær et al. (2008), p.453) and is included in Appendix B. At the time of this study, the plane of patchy weakness model did not include a tensile failure criterion. The borehole stability analyses are for this reason only based on shear failure.

3.5.1 Case assumptions

The cases used when predicted borehole stability with the plane of patchy weakness model were based on the calibrated parameters for the Mancos shale, presented in Table 2.

Table 2: Mancos shale's calibrated parameters for the plane of patchy weakness model.

S_0 [MPa]	φ [°]	S_{0w} [MPa]	φ_w [°]	η_0 [-]	σ_c [MPa]
18.5	30.8	16.1	25.7	0.22	26.8

The other required parameters were formation stresses, pore pressure, angles for wellbore and weakplane orientation, Biot's coefficient, Poisson's ratio and the investigation depth. Their values are presented in Table 3.

Table 3: Summary of case parameters assumed in the prediction of borehole stability.

	σ_H [MPa]	σ_h [MPa]	σ_V [MPa]	p_p [MPa]	i_w [°]	a_w [°]	a [°]	α [-]	ν_{fr} [-]	D [mTVD]
Case A	52.0	52.0	52.0	20.2	0	0	0	1	0.25	2000
Case B	52.0	52.0	52.0	20.2	30	0	0	1	0.25	2000
Case C	43.4	39.8	52.0	20.2	30	0	0	1	0.25	2000

The well pressure, and consequently the mudweight required to prevent shear failure with increasing wellbore inclination was investigated. Three cases were studied, whereas Case A assumed isotropic stresses and horizontal weakplanes. Case B included inclined bedding planes, and Case C combined anisotropic stresses and inclined weakplanes. The pore pressure gradient was assumed to be normal ($\rho = 1030$ kg/m^3). Typical pressure gradients for formation stresses were utilized (Paiaman et al., 2008).

Equations in 2.7 were used to find the quasi-principal stresses. The patchy weakness model expressed in Equations 54 and 55 could then be utilized to predict failure. The well pressure required to prevent shear failure was computed using Excel. Least squares method was applied to minimize $\Delta\sigma^{shear}_{F,intrinsic}$ and $\Delta\sigma^{shear}_{F,wp}$ for θ_B between 0° and 180°. This was repeated for wellbore inclinations 0° to 105° using Visual Basics for Applications (VBA) in Excel. The procedure consequently yielded the minimum mudweight as a function of the wellbore inclination.

4 Results

This section presents results from the failure and stiffness predictions. The behavior of the models are exemplified with results for one lithology. The complete sets of results from the calibration are included in Appendix A. Further, the borehole stability analyses are presented. The results are later discussed in Section 5.

4.1 Failure prediction

The error RSS and mismatch M between the failure criteria and the experimental data for the rock selection are shown in Table 4.

Table 4: Summary of the error and mismatch between the failure model predictions and experimental data. Values in bold indicate the lowest error and degree of mismatch.

	Cazacu et al.		McLamore & Gray		Fjær & Nes	
Lithology	M	RSS	M	RSS	M	RSS
Green River shale 1	2760	2346	465.0	337.0	**263.9**	**217.7**
Green River shale 2	232.6	192.7	**109.2**	**74.89**	136.8	109.4
Tournemire shale	**11.67**	**9.739**	32.02	22.24	30.84	24.84
Mancos shale	**32.70**	**8.174**	-	-	76.27	9.533
Mudstone	298.5	255.8	**95.82**	**70.72**	128.5	107.1
Overall	721.0	694.1	140.0	129.9	**116.9**	**111.8**

The model by Cazacu et al. had the lowest M and RSS values for the Tournemire and Mancos shale. The Tournemire shale displayed a smooth variation in strength, which the criterion reproduced well, illustrated in Figure 7.

The criterion also managed to replicate the reduction in the degree of anisotropy ($\sigma_{1max}/\sigma_{1min}$) with increasing confining pressures. However, the criterion failed to predict the sudden reduction in strength seen for the other rocks.

McLamore & Gray's model reproduced the trends seen in the experimental data. The criterion had the lowest M and RSS values for the Green River shale 2 and the mudstone. For the Green River 1 and the Tournemire shales, it predicted

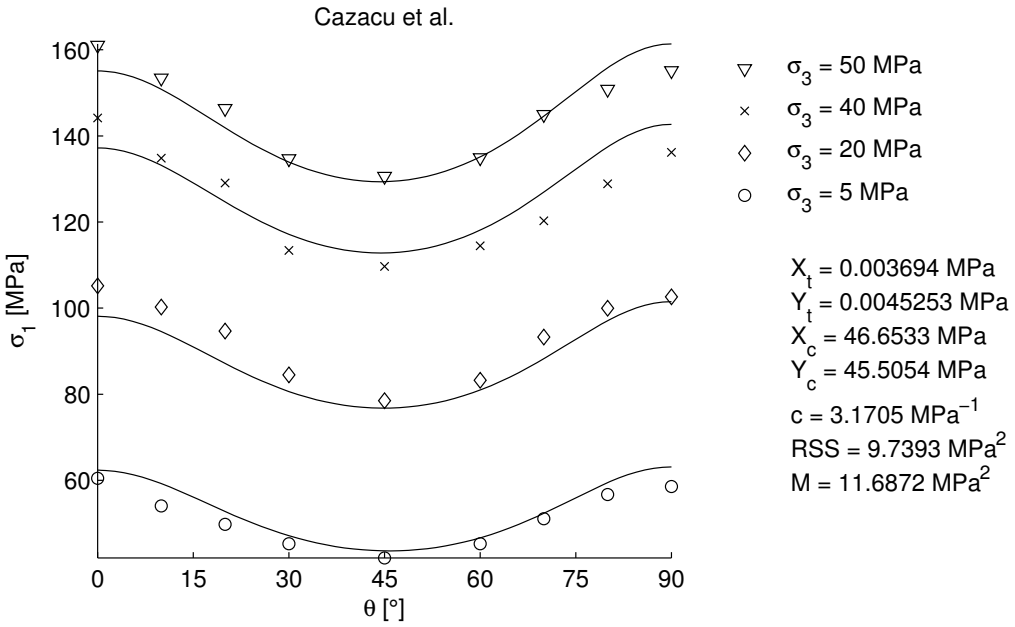

Figure 7: Comparison failure criteria by Cazacu et al. with experimental data for Tournemire shale. The model's calibrated parameters, the error RSS and the mismatch M are listed on the right hand side.

the shoulder type anisotropy seen for the lower inclinations. Green River shale 1 displays this for the inclinations 0-45°, illustrated in Figure 8.

For the first four confining pressures, the model replicated the sudden decrease in strength around 60°. However, for the highest confining pressure, it still predicted a shoulder type anisotropy rather than the smooth strength variation displayed.

The model required $\tan\varphi$ and S_0 as input data to define the orientations at which these parameters were at their minimum (α_1 and α_2). It also required sufficient amount of data for each range to determine the parameters in Equations 25, 26, 27 and 28. For these reasons, the model could not be tested for the Mancos shale.

Fjær & Nes' model reproduced the trends displayed by the experimental data. The criterion had the lowest values of M and RSS for the Green River shale 1. For Green River shale 2, a transition from weakplane to intrinsic failure was clearly replicated, illustrated in Figure 9.

For increasing confining pressures, the range and magnitude of the weakplane cri-

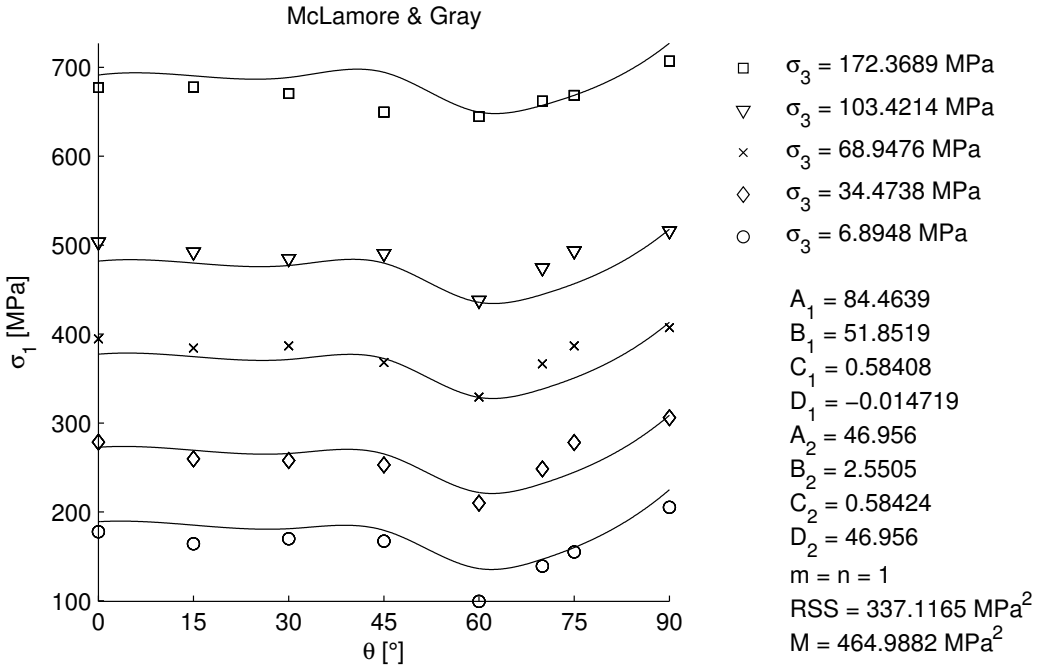

Figure 8: Comparison of McLamore & Gray's failure criteria with experimental data for Green River shale 1. The model's calibrated parameters, the error RSS and the mismatch M are listed on the right hand side.

terion were gradually replaced by the intrinsic criterion. For the Tournemire shale, both the cohesion and friction angle were higher for the weakplane criterion than the intrinsic criterion. The physical validity of these solutions will be discussed in Section 5.

The minimum strength in each rock occured at different orientations. For Green River shale 1 and 2 and the mudstone, the sudden decrease in strength occured at 60°. The Mancos shale displayed its minimum strength at 53°. These sudden decreases in strength suggest that the yielding occurred due to weakplane failure. The maximum strength for Green River shale 1 and 2 and the Mancos shale occurred at 90°. For the Tournemire shale and the mudstone, the maximum strength was observed at 0°.

A remark was made in particular on the large mismatch and error for Cazacu et al. and Fjær & Nes's models and the mudstone. A large mismatch and error was also seen between predictions by Cazacu et al. and the data for the Green River

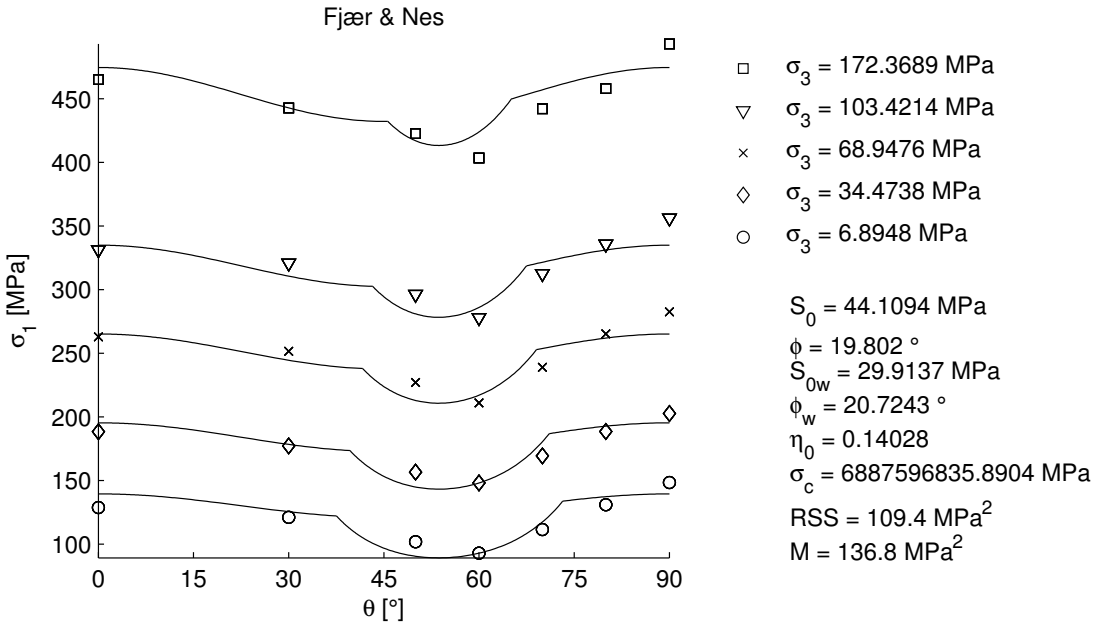

Figure 9: Comparison of Fjær & Nes's failure criteria with experimental data for Green River shale 2. The model's calibrated parameters, the error RSS and the mismatch M are listed on the right hand side.

shale 1. These observations will be discussed in Section 5.

The overall error and mismatch in Table 4 describes the fit between all observations and predictions by a model. In this comparison, the model by Cazacu et al. had the highest values. McLamore & Gray placed second, and Fjær & Nes' model had the lowest error and degree of mismatch.

4.2 Stiffness prediction

The error RSS and mismatch M between the stiffness models and the experimental data for the rocks are shown in Table 5.

Backus' and Fjær & Nes' stiffness prediction models reproduced the trends seen for some of the rocks. Backus' model had the lowest values for M and RSS for the Green River shale 2. The plane of patchy weakness model had the lowest degree of mismatch and error for the Green River shale 1 and the Tournemire shale.

Table 5: Summary of the error and mismatch between the stiffness model predictions and experimental data. Values in bold indicate the lowest error and degree of mismatch.

	Backus		Fjær & Nes	
Lithology	M	RSS	M	RSS
Green River shale 1	32.30	8.074	**8.006**	**4.003**
Green River shale 2	**2.991**	**0.427**	12.16	5.210
Tournemire shale	-63.64	12.73	**25.74**	**5.148**
Mancos shale	4.609	**0.6584**	**4.111**	1.762
Mudstone	-	-	-	-
Overall	6.920	5.382	**4.633**	**3.947**

For the Mancos shale, the Backus model had the lowest error of the two. However, the patchy weakness model still achieved a lower degree of mismatch due to its few parameters. The negative M-value seen for Tournemire shale resulted from the number of observations being lower than $(p-1)$ in Equation 42. The two models with data from the uniaxial tests for Mancos shale are illustrated in Figure 10.

For Backus' model, the volumetric portion x is the relative thickness of one layer in the sample, and must be between 0 and 1. Still, $x > 1$ was returned when fitting the parameters for the Mancos shale. Another observation was made on Backus' parameters for the Green River shale 1 and the Tournemire shale. For these rocks the Lamé coefficient λ_1 was returned as zero when calibrating the parameters. This results in division by zero for $f = \frac{\lambda_2}{\lambda_1}$. Constraints were put on these parameters, enforcing Excel to find solutions within the limits of physical validity. This only resulted in the parameters converging towards the new constraining value rather than the best value.

The calibration of the models was done with stiffness data averaged over the respective confining pressures, with the exception of Mancos shale. A general remark was made on the increase of the stiffness with loading direction.

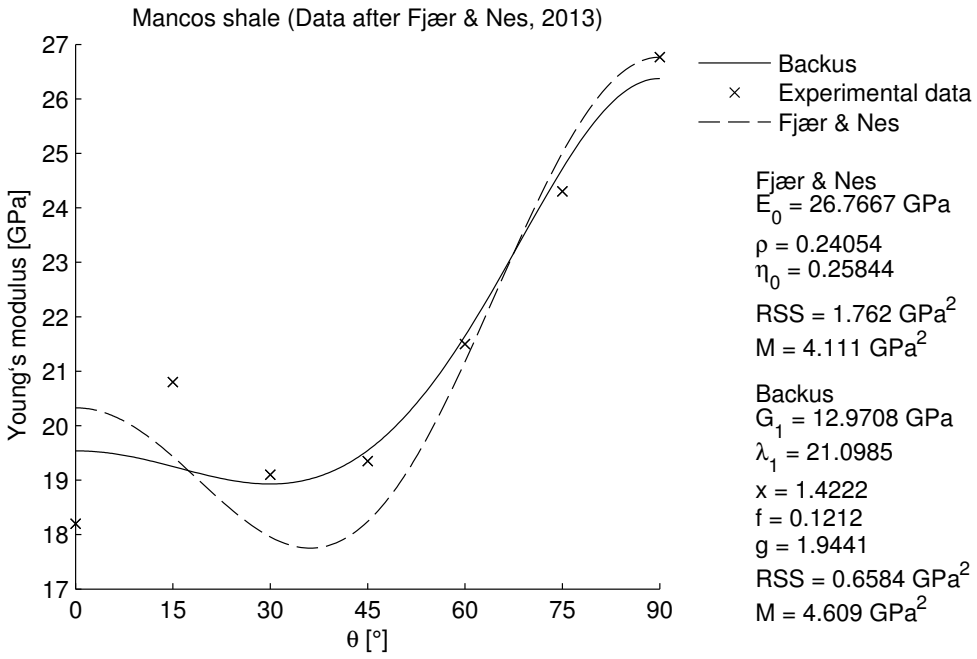

Figure 10: Comparison of Fjær & Nes's and Backus' stiffness models with experimental data for Mancos shale. The models' calibrated parameters, the error RSS and the mismatch M are listed on the right hand side.

4.3 Borehole stability prediction

The patchy weakness model by Fjær & Nes was utilized to predict shear failure as a function of borehole inclination. The maximum predicted mudweight as a function of the azimuthal angle θ_B relative to the largest horizontal stress had to be located. The procedure for this is discussed in more detail in Section 5. For low wellbore inclinations, the weakplane criterion was not activated. However, for higher wellbore inclinations, intersections between weakplane and intrinsic failure was observed, shown in Figure 11.

The minimum mudweight for a given wellbore inclination was consequently the maximum of either the weakplane or the intrinsic criterion. Calculating for multiple wellbore inclinations yielded the minimum mudweight as a function of this variable. The results for isotropic stresses and horizontal weakplane in Case A are shown in Figure 12.

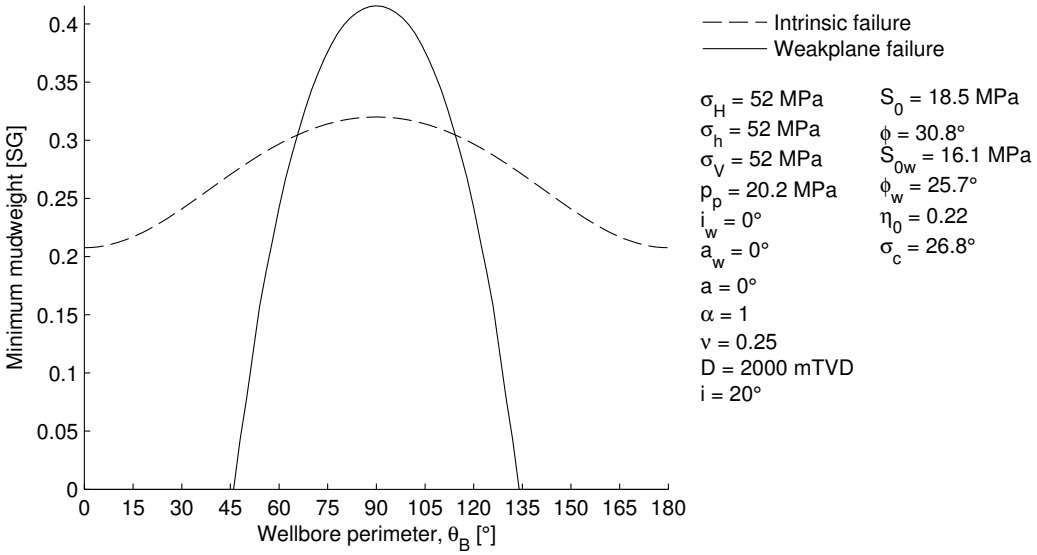

Figure 11: Typical intersection between intrinsic and weakplane failure curves for a borehole perimeter analysis. The intersection is exemplified with 20° borehole inclination.

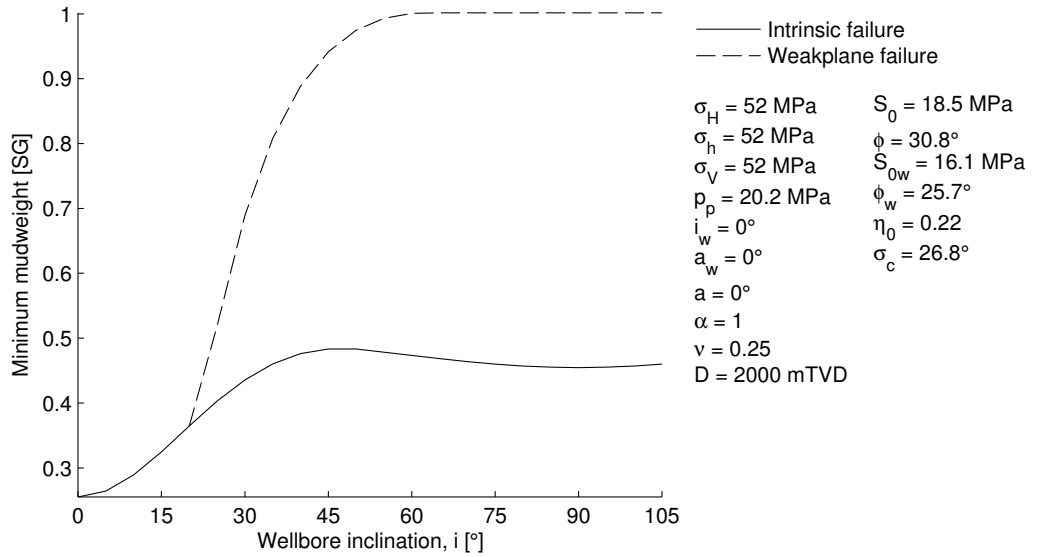

Figure 12: The minimum mudweight as a function of the borehole inclination for horizontal weakplane and isotropic stresses in Case A. The case parameters are listed on the right hand side

The intrinsic criterion predicted the mudweight limit for borehole inclinations be-

tween 0° and 20°. It was intersected by the weakplane criterion at 20°, which predicted the minimum mudweight for the higher inclinations.

The results for isotropic stresses and 30° inclined weakplane in Case B are shown in Figure 13.

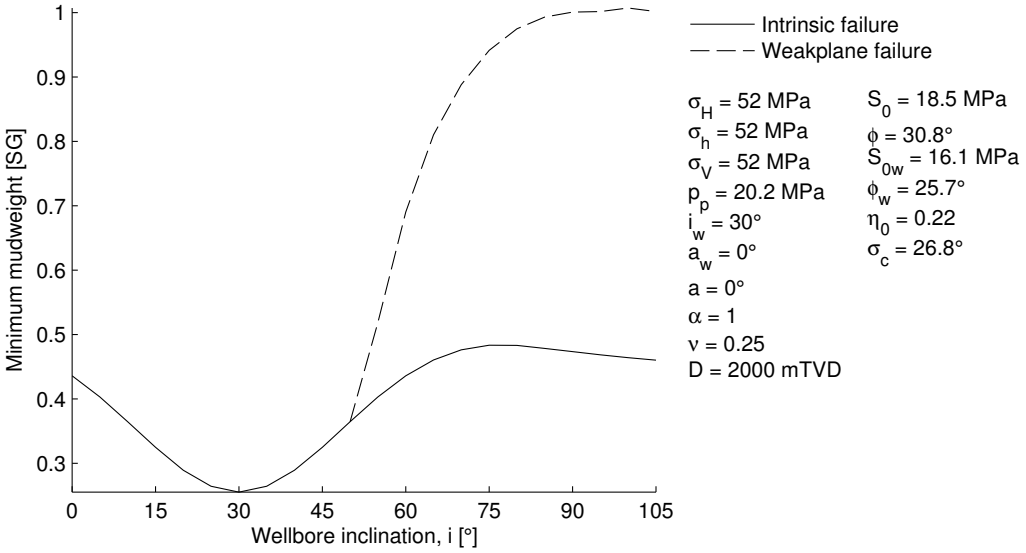

Figure 13: The minimum mudweight as a function of the borehole inclination for 30° weakplane inclination and isotropic stresses in Case B. The case parameters are listed on the right hand side

A 30° displacement was seen for the intrinsic and weakplane failure curves relative to the previous case. This was expected because 0° wellbore inclination now represented a loading angle 30° relative to the weakplane. Increasing the wellbore inclination to 30° meant that the loading direction was normal to the weakplane. As in Case A, the weakplane criterion produced a much higher required mudweight than the intrinsic criterion.

The minimum mudweight with anisotropic stresses and 30° inclined weakplane in Case C was predicted. The result, together with prediction using isotropic settings in the plane of patchy weakness model is shown in Figure 14.

In this case, the intrinsic criterion had its minimum around 15°. The maximum was displayed at 90° by the weakplane criterion. The combination of anisotropic

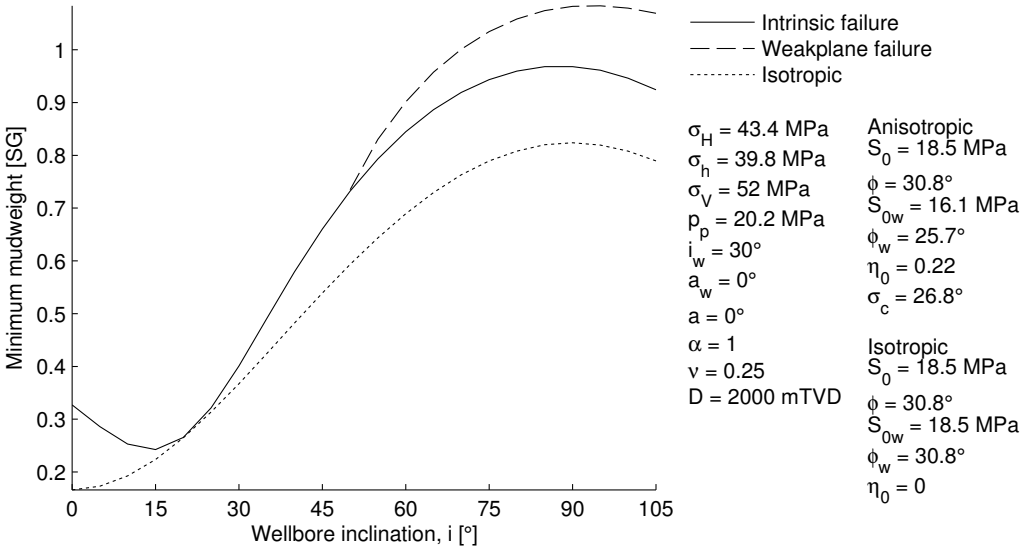

Figure 14: The minimum mudweight as a function of the borehole inclination for 30° weakplane inclination and anisotropic stresses in Case C. The isotropic curve was produced by turning of the anisotropy, shown on the right hand side

stresses and weakplane inclination resulted in increased required mudweight for higher inclinations, than for the other cases.

Strength anisotropy may be neglected by setting $S_0 = S_{0w}$, $\varphi = \varphi_w$ and $\eta_0 = 0$ in Fjær & Nes' model. The difference between the isotropic and anisotropic predictions illustrates the impact of accounting for rock strength anisotropy. The maximum of both predictions occurred for 90° wellbore inclination. The maximum of the isotropic and the intrinsic anisotropic curves were 0.82 SG and 0.97 SG respectively. This suggests an 18 % increase when accounting for intrinsic anisotropy. For the anisotropic weakplane prediction, the maximum value was 1.08 SG, indicating a 32 % increase for the weakplane relative to the isotropic curve.

5 Discussion

In this section, the results from the optimization of the models in the study are discussed. The section includes recommendations on using the different prediction models and consideration of physical validity, followed by sources of uncertainty. Last, a model classification and the results on borehole stability predictions with Fjær & Nes' failure model are discussed.

5.1 Failure criteria

5.1.1 Failure criteria recommendation

Cazacu et al. offers a mathematically based criterion, meaning that it does not model physical failure modes. Because it is continuous, it has the advantage of easily avoiding numerical instabilities when used in computer codes. The criterion assumes failure if the stress state is beyond the perimeter of its paraboloid failure surface. This is demonstrated by its smooth variation in strength with loading direction. The data for Tournemire shale displayed such a variation. For this rock, the criterion produced the best fit of the three models. Studies show that the model accurately predicts failure in other transversely isotropic rocks such as slate and diatomite (Cazacu and Cristescu, 1998) (Cazacu et al., 1998). However, sedimentary lithologies like mudrocks usually possess planes of weakness, which the model failed to predict. This was expressed by the largest overall error (RSS=694) and mismatch (M=721) of the failure models. Therefore, the model by Cazacu et al. is not recommended for these rock types.

McLamore & Gray's model predicted the trends seen in the data, and had the second largest overall error (RSS=130) and mismatch (M=140) . It reproduced a shoulder type behavior seen in some of the data as well as the decrease in strength for weakplane failure. On the other hand, this model involves many parameters. It also requires a large number of triaxial tests to be fitted. In addition, the variation of cohesion and friction factor is purely empirical. This is disadvantageous because it does not relate to the physical failure process.

The patchy weakness model is the recommended model for predicting failure for the mudrocks investigated. This discontinuous criterion had the lowest overall error (RSS=112) and mismatch (M=117) of the models in the study. In addition, the criterion is based on physical failure processes with a low number of parameters. Because the parameters have physical interpretation, the validity of the solution may be considered. The model reproduced both smooth strength variation and failure due to weakplanes. Its behavior was clearly demonstrated for the Green River shale 2. For this rock, the range and magnitude of the weakplane criterion was gradually replaced by the intrinsic criterion. At inclinations where the intrinsic criterion predicted the lowest yield strength, the patchiness parameter created smooth variations which matched the data. For Tournemire shale, the weakplane criterion never intersected with the intrinsic one. This resulted in the model predicting a continuous smooth variation as displayed by the data.

5.1.2 Physical validity

An inverse problem implies converting the experimental data into physical or empirical parameters involved in a model. This form of problem solving will produce a mathematically optimized solution for a set of values, disregarding any physical constraints. Therefore, the output should be analyzed to confirm is the solution if physically possible.

The patchy weakness model had the friction angles of the weakplane and intrinsic failure as model parameters. It was for several rocks observed that $\varphi_w > \varphi$, as illustrated conceptually in the σ',τ-plane in Figure 15.

Intuitively, these solutions seem strange because it implies that the weakplane failure can occur at a higher stress than intrinsic failure. However, the model is not restricted to the weakplane criterion always being the lower one. A physical explanation to this is that the weakplanes are comprised of small parallel cracks. When compressed, the cracks may close and the weakplanes can yield higher strength. In addition, the real failure envelope may be a parabola in the σ',τ-plane, which can also cause this occurrence.

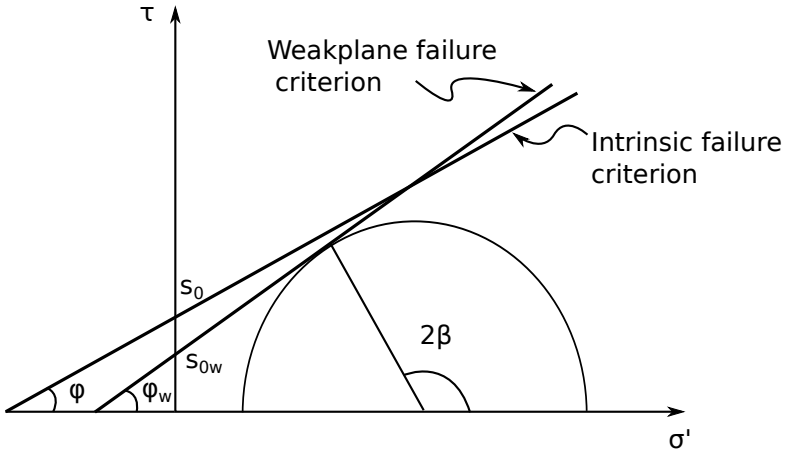

Figure 15: Illustration showing the intersection of weakplane and intrinsic criteria, and the Mohr-circle. β is in this case the failure angle.

For the Tournemire shale, both the cohesion and friction angle were higher for the weakplane than for intrinsic failure. For these optimized parameters, the weakplane failure envelope is always the highest one in the σ',τ-plane. This implies that the rock always yields due to intrinsic failure. Analytically, this solution is invalid for a rock failing due to weakplanes. However, the Tournemire shale displayed no sudden decrease in strength, suggesting intrinsic failure for all orientations. The model predicts no activation of weakplane failure, which agrees with the observations.

5.1.3 Uncertainties

When calibrating the anisotropic failure criteria to the experimental data, various factors may contribute to the error and mismatch. First, the three failure criteria are assuming transverse isotropy. Travel time measurements of seismic wave propagation in selected directions may describe the elastic response for a layer. However, this does not necessarily translate to strength anisotropy. This makes it difficult to confirm if the rock is transversely isotropic in strength. Nevertheless, this assumption is widely used, especially for shales. Shale consist of clay platelets that after deposition undergo compression due to the weight of the overburden. Like a deck of cards, the platelets align, constituting a physical basis that

is approximated with the transverse isotropy assumption.

The dominating physical effects differs for different failure modes. McLamore & Gray and Fjær & Nes's models both assume shear failure. The authors for the Green River, Tournemire and Mancos shales reported that the samples failed in shear. However, McLamore & Gray observed kinking and plastic slip for higher confining pressures for Green River shale 2. In the case of the mudstone, no descriptions on the failure mode were available. The differences in failure modes suggest that shear failure assumption was only satisfied at times. This may have been contributing to the errors and mismatch in the analyses.

Another potential source of error was the uncertainty in triaxial test method. The drained tests of the Green River shales and the Mancos shale had atmospheric pore pressure during compression. This means that the total stress was carried by the framework of the rock ($\sigma = \sigma'$). On the other hand, the test method for Tournemire shale and the mudstone was not stated. The Skempton coefficients (Fjær et al. (2008), p.29) may be used to account for the variable pore pressure. However, the bulk modulus K_{fr} required as input is not a representative material constant, as it is directionally dependent. In addition, no data on required input for determining an anisotropic K_{fr} was available. For the Tournemire shale, the fit was still good, suggesting that pore pressure did not affect the effective stress. However, the low degree of fit for the mudstone may be caused by pore pressure acting as a dependent variable in the effective stress.

For the McLamore & Gray model, linear extrapolation of the failure envelopes were conducted to provide necessary input data. As the failure envelopes tend to be non-linear for higher stresses (Fjær et al. (2008), p.20), this method may contribute towards the error and mismatch.

Another possible source of error may be the spread in the data itself. With the exception of Mancos shale, the spread in test data was not available, and was therefore not investigated.

The digitization of the data was based on placing the mouse cursor on the data points of interest. Even though its likely to have a low impact, this uncertainty may still have contributed towards the error in the analyses.

5.2 Stiffness models

5.2.1 Stiffness model recommendation

The plane of patchy weakness model achieved a lower error and degree of mismatch (RSS=3.9, M=4.6) compared to Backus' model (RSS=5.4, M=6.9). Both stiffness models were based on parameters which can be interpreted physically. Nevertheless, patchy weakness has the lowest number of parameters. This advantage is exemplified by the model achieving a lower degree of mismatch for the Mancos shale.

Involving the number of model parameters, the mismatch indicates the relevance of the physics in a model. A low number of parameters results in a lower degree of mismatch. For the Mancos shale, the plane of patchy weakness model achieved the lowest degree of mismatch, even though it displayed the larger error. This indicates a better relevance of the physical process.

5.2.2 Physical validity

Backus' model has the volumetric portion and Lamé's coefficients as model parameters. It was for several rocks observed that the volumetric portions x were larger than 1, and $\lambda_1 = 0$. $x > 1$ is an invalid solution because the volume of one layer can not be larger than the total sample volume. $\lambda_1 = 0$ implies divison by zero, but $\lambda = 0$ is not an unphysical value. This problem probably arises due to the definition of $f = \frac{\lambda_2}{\lambda_1}$. A solution to this might be to redefine f as the ratio between uniaxial compaction moduli H [5], expressed in Equation 64.

$$f = \frac{H_1}{H_2} = \frac{\lambda_1 + 2G_1}{\lambda_2 + 2G_2} \tag{64}$$

[5]Erling Fjær (SINTEF Petroleum Research). Private communication, 27^{th} of May 2014.

5.2.3 Uncertainties

For both models predicting the effective stiffness, the confining pressure is assumed to be zero. If the confining pressure was assumed to be an additional variable, the layers would experience different confining stress due to the different stiffness in the layers. For a horizontally layered sample, this would be possible to derive. However, if the sample was to be rotated, the derivation would become complex. It was therefore decided to neglect the confining pressure when deriving Backus' effective stiffness. Only the Mancos shale had zero confining pressure for the stiffness data, meaning that only this dataset satisfied the assumption. For the other rocks, the available stiffness data was averaged over the different confining pressures. The simplification may therefore affect the optimization of the parameters, causing inaccurate predictions.

Both stiffness criteria were based on linear elasticity. For rock materials in general, linear elasticity may sufficiently describe the elastic behavior for small stress changes. However, for larger stress changes, most rocks behave non-linearly. For instance, Niandou et al. (1997) concluded that the Tournemire shale should be described by plastic rather than linear elastic models. If the linear elasticity assumption is not satisfied, this becomes a potential source of uncertainty.

5.3 Model classification

For the rock selection used in this study, the plane of patchy weakness model is preferred. It proves its versatility when being able to predict trends of both weakplane failure and smooth strength variation due to intrinsic anisotropy. Sedimentary rocks tend to display drastically reduced strength for a range of inclinations due to structural anisotropy. Metamorphic rocks may no longer have weakplanes, but can still posses intrinsic anisotropy, yielding a smoother strength variation. These findings suggest that the plane of patchy weakness criterion may be used for a variety range of transversely isotropic rocks. The plane of patchy weakness model also has the benefit of being accompanied by an expression for stiffness prediction. This stiffness prediction model is also the preferred choice of the two

models investigated.

5.4 Borehole stability

5.4.1 Effect of stress and strength anisotropy

In the stability predictions, the Mancos shale's calibrated parameters together with Fjær & Nes' failure model were used. Emphasis was put on the observed trends because the cases were hypothetical.

Stress isotropy and horizontal weakplanes in Case A displayed a significant difference between the intrinsic and the weakplane failure predictions. When assuming inclined weakplane in Case B, the failure curves shifted according to the weakplane inclination as expected.

Case C combined stress anisotropy and inclined weakplane. This stress configuration utilized typical stress gradients, and represents therefore a more realistic case as it resembles *in-situ* stresses. The combination of the two effects resulted in increased mininum mudweight predicted by both criteria compared to the cases with isotropic stresses. A decreasing trend in the weakplane limit was observed for wellbore inclinations higher than 90° . This is expected due to the decrease in tangential stress after its maximum at this inclination. The intrinsic and the weakplane curves peaked at around 90°, yielding the highest required mudweight at this inclination.

The minimum value of the mudweight was found at 15° wellbore inclination. This minimum shows the effect of the patchiness parameter η's ability to predict the intrinsic anisotropy outside the weakplane failure region.

Intuitively, minimum at 15° seems strange because the weakplane inclination was 30° like in the cases of isotropic stress. The rock's intrinsic strength will still be at its maximum for 30°. However, the stress anisotropy and the intrinsic strength works in the same direction for inclinations between 0° and 30°. The strength of the rock and the stress acting on the borehole wall will increase when rotating towards

the weakplane's normal. Consequently, the location of the minimum mudweight shifts from 30° towards zero due to the stress anisotropy.

When comparing the predictions using anisotropic and isotropic strength in Fjær & Nes' model, significant differences were revealed. The results indicated up to 18 % increase in minimum mudweight when accounting for intrinsic anisotropy. This effect became more pronounced when accounting for weakplane failure, where 32 % increase in minimum mudweight was displayed. These differences underline the importance of accounting for strength anisotropy in borehole stability analyses.

5.4.2 Uncertainties

The solutions for stress around the wellbore used in this work are based on linear elasticity. Depending on the rock's behavior, this can become a source of error in the borehole stability predictions. Because of the linear elasticity assumption, the analyses are limited to the point of failure initiation. Post failure initiation behavior can be approximated with simple models such as the linear elastic/perfectly plastic model, described in Fjær et al. (2008). However, more accurate descriptions of plastic material often require advanced modeling through numerical simulations.

Another assumption made in these predictions was that the failure always occurred at the borehole wall. This is a pessimistic assumption, because failure happens at the borehole wall first. Development of near-wellbore plastic zones and pore pressure dissipation are factors which may cause wellbore failure some distance from the wall. Hence, predicitons assuming failure at the wellbore wall are mainly of academic interest.

5.4.3 Wellbore periphery analysis

The azimuthal angle θ_B that produced the highest mudweight was not constant. Variation in this angle influences the minimum predicted well pressure. Finding the point along the periphery where the limit is at its maximum is therefore necessary. Typical development of minimum mudweight as a function of the wellbore perimeter for intrinsic failure is shown in Figure 16.

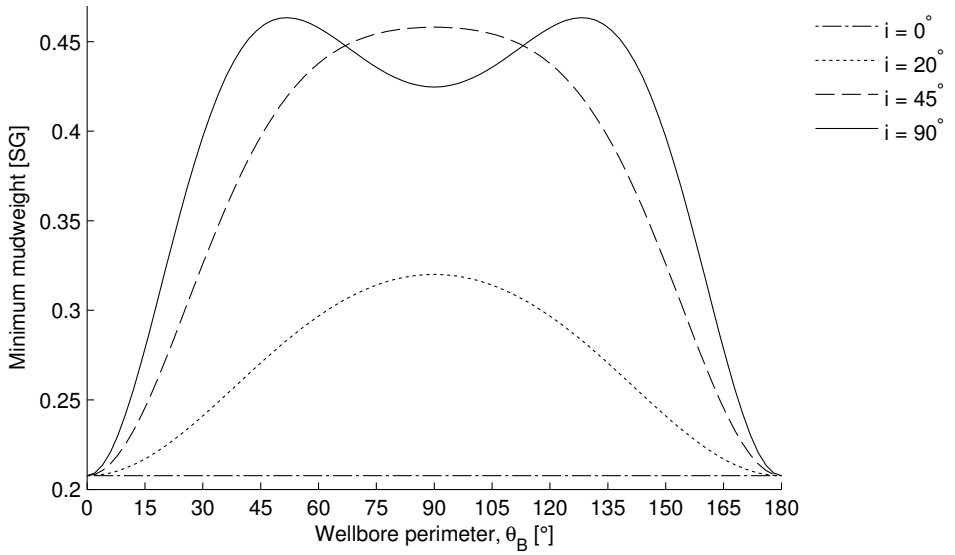

Figure 16: Typical development of minimum mudweight as a function of the borehole perimeter for intrinsic failure predicted by Fjær & Nes' model.

An increased borehole inclination resulted in increased magnitude of the mudweight required to prevent failure. Similarly, the weakplane failure was also affected by an increasing wellbore inclination, illustrated in Figure 17.

The figures also illustrate that the maximum values of mudweight shifted away from $\theta_B = 90°$ at higher wellbore inclinations.

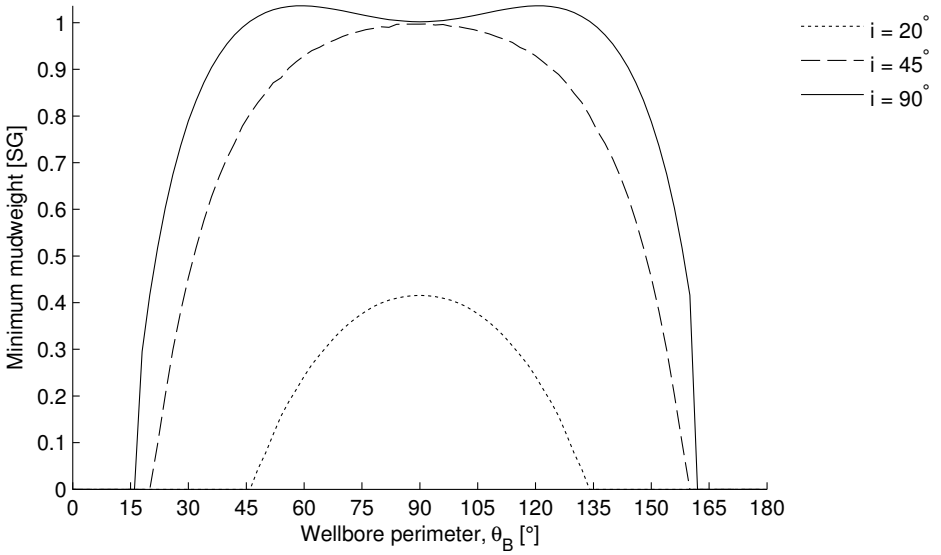

Figure 17: Typical development of minimum mudweight as a function of the borehole perimeter for weakplane failure predicted by Fjær & Nes' model.

5.4.4 Challenges

Numerical instabilities were encountered when predicting borehole stability with the weakplane criterion in the patchy weakness model. The criterion displayed asymptotic behavior when conducting the wellbore periphery analyses. This made it somewhat difficult to determine if the peak stress was correct. Investigations were carried out to confirm the results. Similar trends was seen in other studies accounting for anisotropic strength (Paiaman et al., 2008) (Bassey et al., 2013). PSI, a shale instability prediction software by SINTEF Petroleum Research produced the same behavior with the mudweight peaking for 90° wellbore inclination. However, the studies and PSI predictions were performed with the single plane of weakness model by Jaeger (1960). Hence, the results are not necessarily comparable with these findings.

For the purpose of simplification, the cases presented only considered elastic stresses, disregarding a range of other important factors contributing towards failure. Formation permeability, thermal effect, chemical activity and plastic strain are some of the effects left out. A more realistic setting could be studied by implementing

the plane of patchy weakness prediction model into the PSI software. Sensitivity analyses could in this program be conducted more easily than with the VBA based Excel approach.

6 Future work

The author encourages future studies to conduct inverse problem optimizations for the plane of patchy weakness model on other rock types. This might aid in determining which rocks the model can be applied to. Additionally, it is suggested to implement the patchy weakness model into PSI. The impact of strength anisotropy may then be monitored for a more realistic setting. The author also encourages future studies to investigate the effects of using coupled equations for stress and deformation in borehole stability prediction.

7 Conclusion

Three anisotropic failure criteria and two anisotropic stiffness prediction models have been tested against experimental data. Results from 171 compression tests for five different mudrocks were used to calibrate the models using inverse problem theory. In addition, Fjær & Nes' failure criterion was used to predict borehole stability in three different cases. The final result was compared with borehole stability analyses using strength isotropic conditions in the same criterion. The following conclusions were drawn from the results:

- Data from the rock selection showed significant strength anisotropy. Intrinsic failure was shown as a smooth strength variation with loading direction. Weakplane failure was displayed by the characteristic sudden decrease in strength for specific ranges of inclination.
- The data displayed pronounced stiffness anisotropy for all rocks in the selection. A general increase in the effective stiffness with loading direction was observed. However, the directional anisotropy for stiffness was not as systematic as the strength anisotropy.
- Fjær & Nes' plane of patchy weakness model predicted most accurately the strength and stiffness anisotropy displayed by the data. The failure criteria was found to reproduce the trends for both intrinsic and structural anisotropy. In addition, the model was able to predict the trend of only intrinsic anisotropy seen in one of the shales. This suggests that the model may be used for a variety of transversely isotropic rocks.
- The plane patchy weakness model's ability to predict intrinsic anisotropy was pronounced in the wellbore stability cases where the weakplane was inclined. The required mudweight had its minimum at 15° wellbore inclination. This was opposed to borehole stability predictions based on strength isotropy, which yielded its minimum for vertical wellbore.
- An increase in minimum mudweight was seen for the borehole stability predictions with strength anisotropy compared to with isotropic strength. The results suggested 18% increase due to intrinsic anisotropy, and 32 % increase

when accounting for structural anisotropy in Mancos shale. This result underlines the importance of considering strength anisotropy in borehole stability predictions.

Nomenclature

α	Biot's coefficient
α_1	The orientation where S_0 is at its minimum
α_2	The orientation where $\tan\varphi$ is at its minimum
β	Angle between major principal stress and weakplane
$\boldsymbol{C}$	Stiffness tensor
$\boldsymbol{l}_{ij}$	Directional components
$\boldsymbol{R}_{\epsilon}$	Rotation matrix for $\boldsymbol{\epsilon}$
$\boldsymbol{R}_{\sigma}$	Rotation matrix for $\boldsymbol{\sigma}$
$\hat{\boldsymbol{\sigma}}$	Principal axes
ϵ	Normal strain
ϵ_{kl}	Strain tensor
η	Patchiness parameter
η_0	Patchiness at zero confining pressure
Γ	Shear strain
λ	Lamé's coefficient
$\nu_f r$	Poisson's ratio
Φ	Angle between $\hat{\boldsymbol{\sigma}}_{\mathbf{3}}$ and the intercept between the weak planes and the $\hat{\boldsymbol{\sigma}}_{\mathbf{2}}$
ϕ	Rotation angle to obtain quasi-principal stresses
Ψ	Angle between the major principal stress and the normal of the weakplane
ρ	Excessive normal compliance
Σ	Transformed stress tensor
σ	Normal stress
Σ'	Deviatoric stress of the tensor Σ
σ'	Effective stress
σ_θ^*	Adjusted tangential stress
σ_z^*	Adjusted axial stress
σ^o	*In-situ* stress
σ_1	Major principal stress
σ_2	Intermediate principal stress

σ_3	Minor principal stress
σ_c	Characteristic stress
σ_H	Largest horizontal stress
σ_h	Smallest horizontal stress
σ_r	Radial stress
σ_V	Vertical stress
σ_z	Axial stress
σ_θ	Tangential stress
σ_{ij}	Stress tensor
$\tan\varphi$	Friction factor
τ	Shear stress
τ^o	*In-situ* shear stress
θ	Angle between major principal stress and normal of the weakplane
θ_B	Azimuthal angle relative to the lowermost point on the borehole perimeter
θ_B	Azimuthal angle relative to the lowermost point on the borehole perimeter
φ	Friction angle
a	Wellbore azimuth
a, b, c, d, e	Cazacu et al.'s material constants
a_w	Weakplane azimuth relative to the largest horizontal stress
$A_{1,2}, B_{1,2}, C_{1,2}, D_{1,2}$	McLamore & Gray's empirical parameters
A_{ijkl}	Cazacu et al.'s fourth order strength tensor
C	Stiffness tensor
C_{ijkl}	Elastic constants
D	Depth
E_0	Effective stiffness at $\theta = 90°$
E_i	Stiffness of layer i
E_{eff}	Effective stiffness
g	Gravitational constant
H	Uniaxial compaction modulus
i	Wellbore inclination

i_w	Weakplane inclination relative to the horizontal plane
L	Total sample thickness
L_i	Thickness of layer i
p	Number of parameters in a model
p_p	Pore fluid pressure
p_w	Well pressure
S_0	Cohesion
X_c	Uniaxial compressive strength at $\theta = 0°$.
X_t	Tensile strength at $\theta = 0°$.
Y_c	Uniaxial compressive strength at $\theta = 90°$.
Y_t	Tensile strength at $\theta = 90°$.
G	Shear modulus
M	Degree of mismatch
m	Cazacu et al.'s material constant
m,n	McLamore & Gray's exponents of anisotropy type
MW	Mudweight
N	Number of observations
RSS	Residual Sum of Squares
TVD	True Vertical Depth
x	Volumetric portion

Bibliography

Attewell, P. and Farmer, I. (1976). *Principles of Engineering Geology.* London: Chapman & Gall, p. 298.

Backus, G. E. (1962). Long-wave elastic anisotropy produced by horizontal layering. *Journal of Geophysics, Res. 67. 4427-4440.*

Bassey, A., Dosunmu, A., and Otutu, F. (2013). Modeling wellbore stability while drilling through a parallel weak bedding plane; case study of highly inclined and horizontal wells. *Society of Petroleum Engineers, SPE-167519-MS.*

Cazacu, O. and Cristescu, N. (1998). A paraboloid failure surface for transversely isotropic material. *Elsevier. Mechanics of Materials 31 , pp.381-393.*

Cazacu, O., Cristescu, N. D., Shao, J. F., and Henry, J. P. (1998). A new anisotropic failure criterion for transversely isotropic solids. *Elsevier. Mechanics of cohesive-frictional materials, Vol. 3, pp. 89-103.*

Crawford, B. R., DeDontney, N., Alramahi, B., and Ottesen, S. (2012). Shear strength anisotropy in fine-grained rocks. *American Rock Mechanics Association. ARMA 12-290.*

Duveau, G., Shao, J., and Henry, J. (1998). Assessment of some failure criteria for strongly anisotropic geomaterials. *Mechanics of cohesive-frictional materials vol 3. pp. 1-26.*

Fjær, E., Holt, R., Horsrud, P., Raaen, A., and Risnes, R. (2008). *Petroleum Related Rock Mechanics 2nd Edition.* Elsevier.

Fjær, E. and Nes, O. M. (2013). Strength anisotropy in mancos shale. *American Rock Mechanics Association, ARMA 13-519.*

Fjær, E. and Nes, O. M. (2014). The impact of heterogenity on the anisotropic strength of an outcrop shale. *Rock Mechanics and Rock Engineering, DOI 10.1007/s00603-014-0598-5.*

Fjær, E., Stenebråten, J., Holt, R., Bauer, A., Horsrud, P., and Nes, O. (2014).

Modeling strength anisotropy. *Rock mechanics for Natural Resources and Infrastructure.*

Jaeger, J. (1960). Shear failure of anisotorpic rock. *Geol. Mag. 97:65-72.*

McLamore, R. T. and Gray, K. E. (1967). A strength criterion for anisotropic rocks based upon experimental observations. *Society of Petroleum Engineers, SPE 1721.*

Niandou, H. (1994). *Etude de comportement reéologique et modélisation de l'argilite de Tournemire. Application à la stabilité des ouvrages souterrains.* PhD thesis, USTL, Univérsité de Lille 1.

Niandou, H., Shao, J. F., Henry, J. P., and Fourmaintraux, D. (1997). Laboratory investigation of the mechanical behavior of tournemire shale. *International Journal of Rock Mechanics & Mining Sciences Vol. 34, pp.3-16.*

Paiaman, A. M., Azadbakht, S., and Al-Anazi, B. D. (2008). Optimizing wellbore inclination and azimuth to minimize instability problems. *Oil and Gas Business.*

Purdue University. Course material, CE503 rotation matrices. URL: https://engineering.purdue.edu/ bethel/rot2.pdf. Last visited 8.6.2014.

Tien, Y. M. and Kuo, M. C. (2001). A failure criterion for transversely isotropic rocks. *International Journal of Rock Mechanics & Mining Sciences 38, pp. 399-412.*

Ugural and Fenster (1995). *Advanced Strength and Applied Elasticity, 4th ed.* Prentice Hall.

Appendix A Strength and stiffness analyses

A.1 Strength analyses

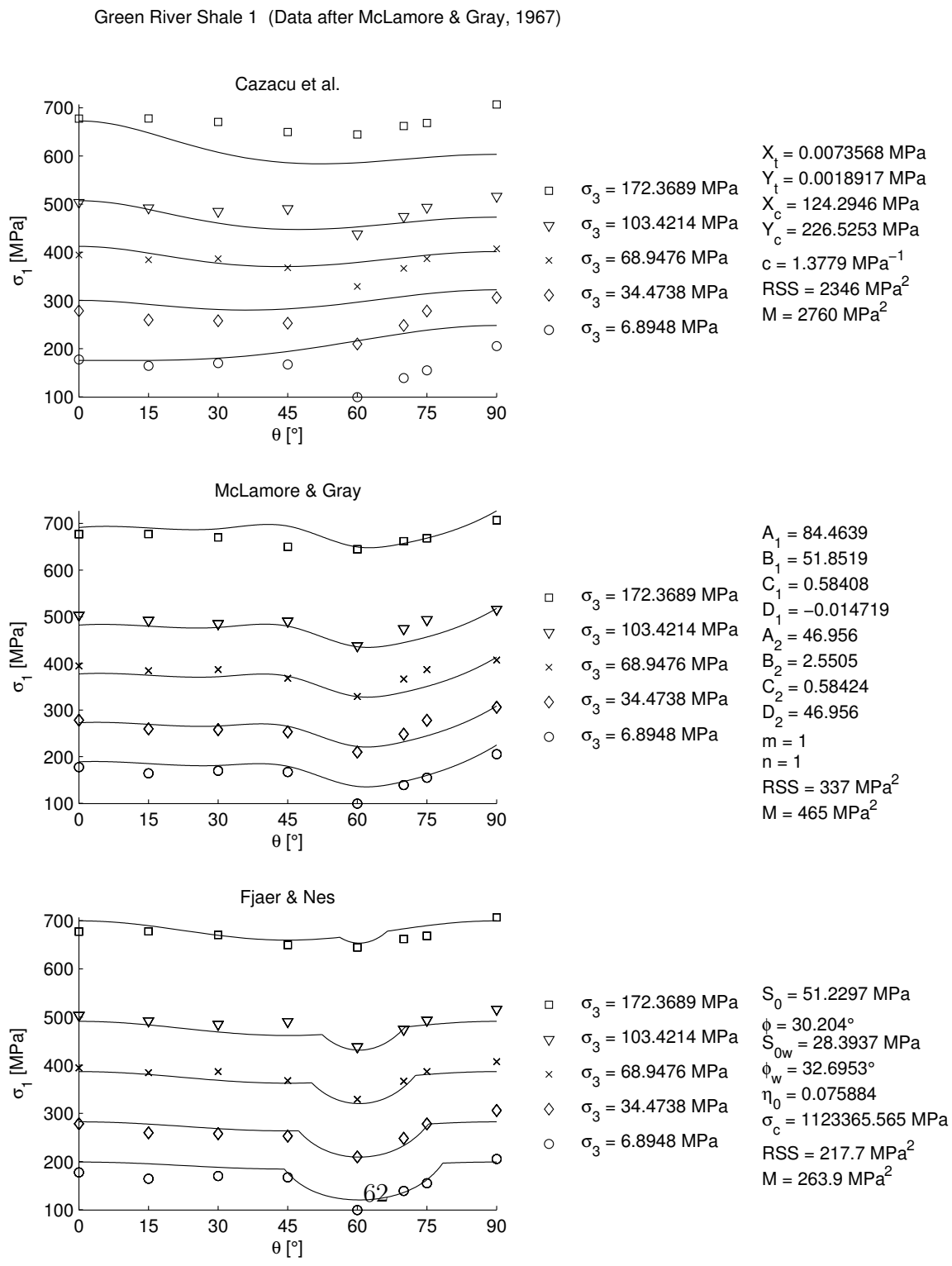

Green River Shale 2 (Data after McLamore & Gray, 1967)

Cazacu et al.

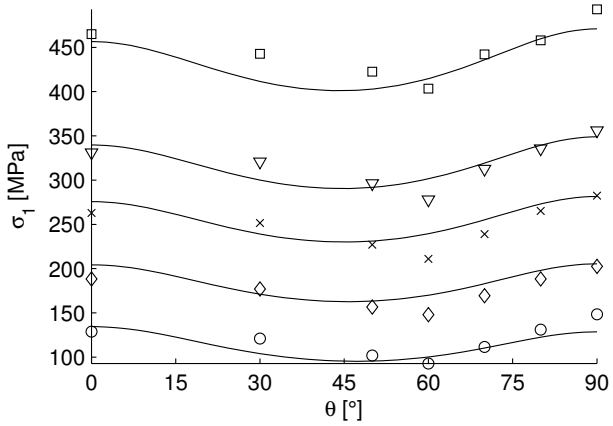

X_t = 0.023321 MPa
Y_t = 0.030655 MPa
X_c = 112.3388 MPa
Y_c = 102.4764 MPa
c = 0.76718 MPa^{-1}
RSS = 192.7 MPa^2
M = 232.6 MPa^2

McLamore & Gray

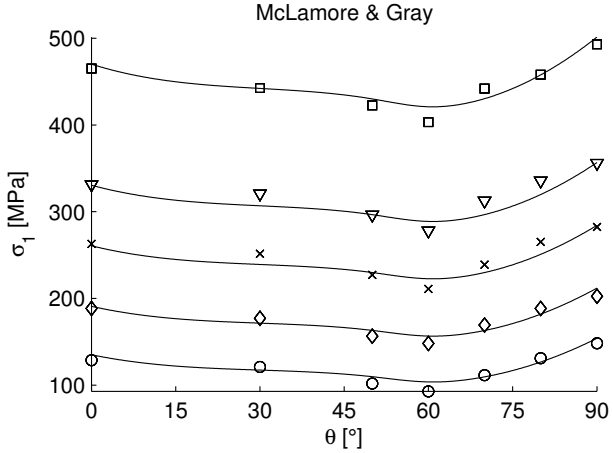

A_1 = 63.6126
B_1 = 30.9472
C_1 = 0.42746
D_1 = 0.096091
A_2 = 39.7999
B_2 = 5.4958
C_2 = 0.35194
D_2 = 39.7999
m = 1
n = 1
RSS = 74.9 MPa^2
M = 109.2 MPa^2

Fjær & Nes

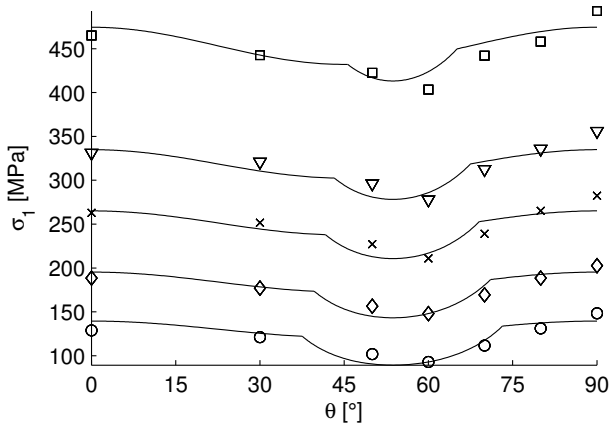

S_0 = 44.1094 MPa
ϕ = 19.802°
S_{0w} = 29.9137 MPa
ϕ_w = 20.7243°
η_0 = 0.14028
σ_c = 6887596835.8904 MPa
RSS = 109.4 MPa^2
M = 136.8 MPa^2

Tournemire shale (Data after Niandou et al., 1994)

Cazacu et al.

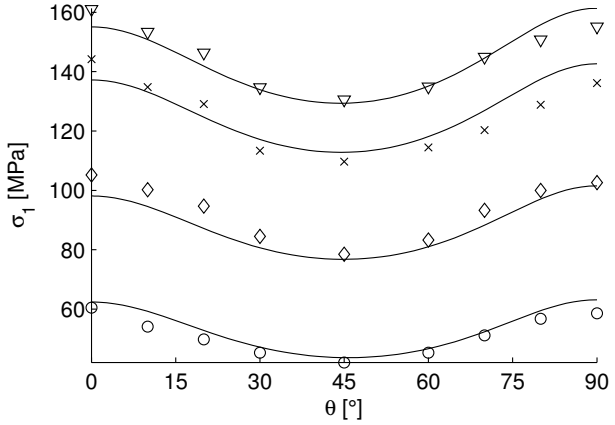

X_t = 0.003694 MPa
Y_t = 0.0045253 MPa
X_c = 46.6533 MPa
Y_c = 45.5054 MPa
c = 3.1705 MPa^{-1}
RSS = 9.739 MPa^2
M = 11.67 MPa^2

McLamore & Gray

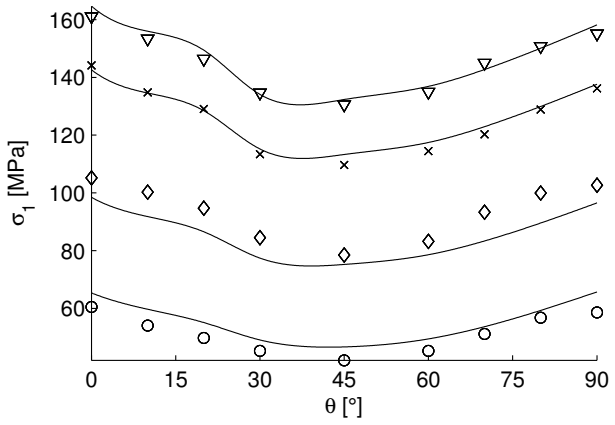

A_1 = 19.3202
B_1 = 5.8734
C_1 = 0.35336
D_1 = 0.029572
A_2 = 18.2727
B_2 = 4.4707
C_2 = 0.43807
D_2 = 18.2727
m = 1
n = 1
RSS = 22.24 MPa^2
M = 32.02 MPa^2

Fjær & Nes

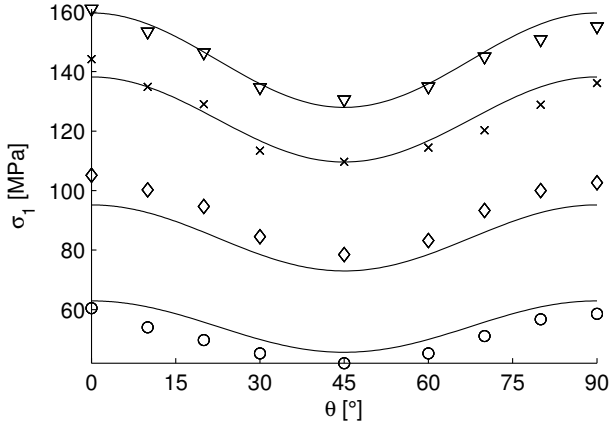

S_0 = 17.7879 MPa
ϕ = 21.4198°
S_{0w} = 20.1098 MPa
ϕ_w = 26.4017°
η_0 = 0.29916
σ_c = 1494.2396 MPa
RSS = 9.533 MPa^2
M = 76.27 MPa^2

Mancos shale (Data after Fjær & Nes, 2013)

Cazacu et al.

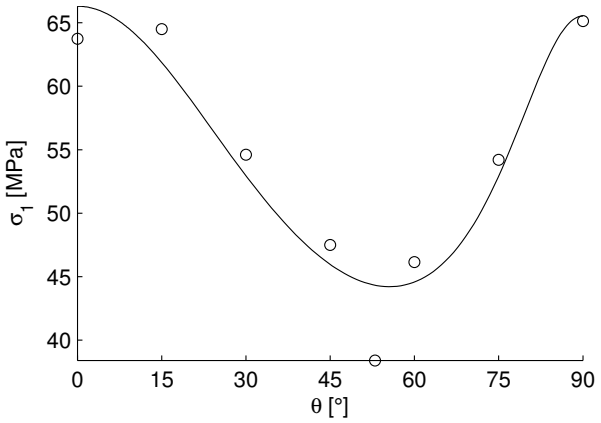

○ σ_3 = 0 MPa

X_t = 0.30006 MPa
Y_t = 1.3598 MPa
X_c = 66.3033 MPa
Y_c = 65.5337 MPa
c = 0.23549 MPa^{-1}
RSS = 8.174 MPa^2
M = 32.7 MPa^2

Fjær & Nes

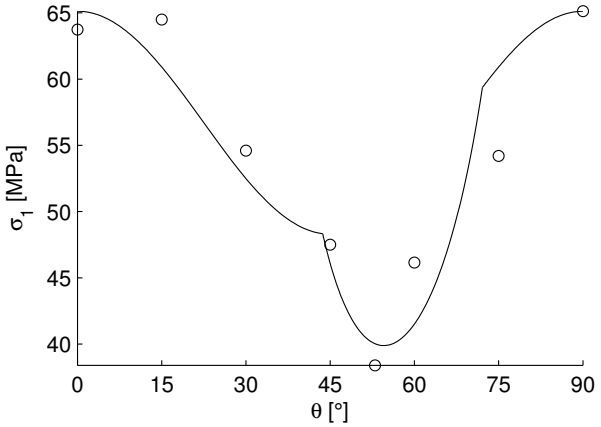

○ σ_3 = 0 MPa

S_0 = 18.5005 MPa
ϕ = 30.7918°
S_{0w} = 16.0865 MPa
ϕ_w = 25.7501°
η_0 = 0.25844
σ_c = 26.7942 MPa
RSS = 9.533 MPa^2
M = 76.27 MPa^2

Laminated silty mudstone (Data after Attewell & Farmer, 1976)

Cazacu et al.

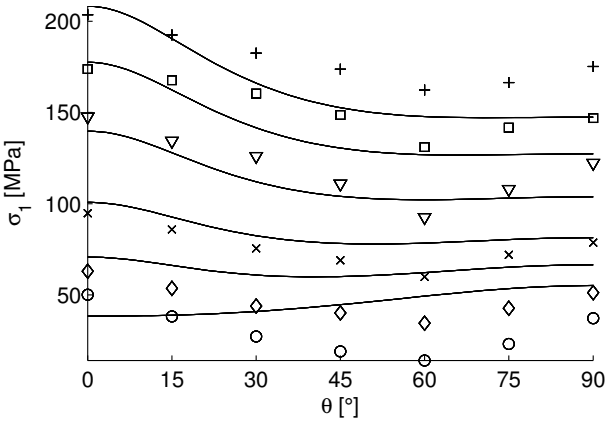

+ σ_3 = 43 MPa
□ σ_3 = 32 MPa
▽ σ_3 = 20 MPa
× σ_3 = 9.8 MPa
◇ σ_3 = 3.9 MPa
○ σ_3 = 0 MPa

X_t = 0.0030051 MPa
Y_t = 0.00051375 MPa
X_c = 38.3823 MPa
Y_c = 55.1475 MPa
c = 4.7193 MPa^{-1}
RSS = 255.8 MPa^2
M = 298.5 MPa^2

McLamore & Gray

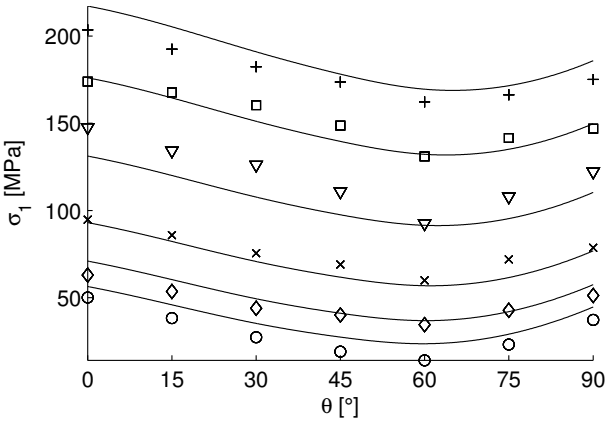

+ σ_3 = 43 MPa
□ σ_3 = 32 MPa
▽ σ_3 = 20 MPa
× σ_3 = 9.8 MPa
◇ σ_3 = 3.9 MPa
○ σ_3 = 0 MPa

A_1 = 18.2195
B_1 = 11.825
A_2 = 11.9162
B_2 = 5.3213
C_2 = 0.66943
D_2 = 11.9162
m = 1
n = 1
RSS = 70.72 MPa^2
M = 95.82 MPa^2

Fjær & Nes

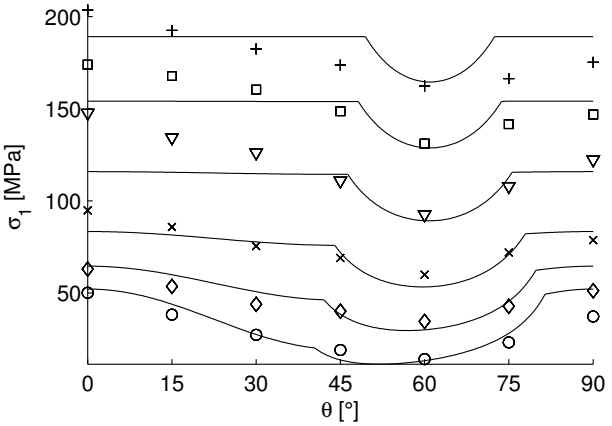

+ σ_3 = 43 MPa
□ σ_3 = 32 MPa
▽ σ_3 = 20 MPa
× σ_3 = 9.8 MPa
◇ σ_3 = 3.9 MPa
○ σ_3 = 0 MPa

S_0 = 14.5948 MPa
ϕ = 31.4851°
S_{0w} = 6.9478 MPa
ϕ_w = 31.9174°
η_0 = 0.62979
σ_c = 5.3891 MPa
RSS = 107.1 MPa^2
M = 128.5 MPa^2

A.2 Stiffness analyses

Green River Shale 1 (Data after McLamore & Gray, 1967)

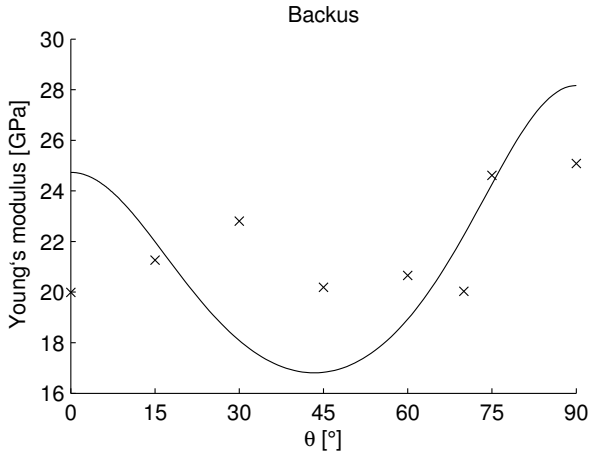

G_1 = 13.9403 GPa
λ_1 = 0 GPa
x = 0.85373
f = 0.32179
g = 0.53464
f = 0.32179
RSS = 32.3 GPa^2
M = 8.074 GPa^2

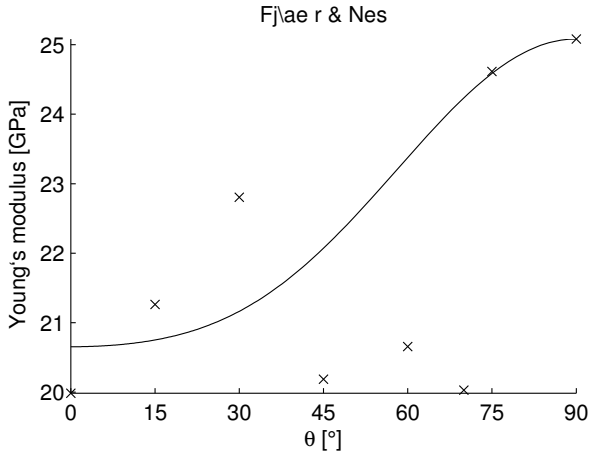

E_0 = 25.0823 GPa
ρ = 0.17654
η_0 = 0.075884
RSS = 4.003 GPa^2
M = 8.006 GPa^2

Green River Shale 2 (Data after McLamore & Gray, 1967)

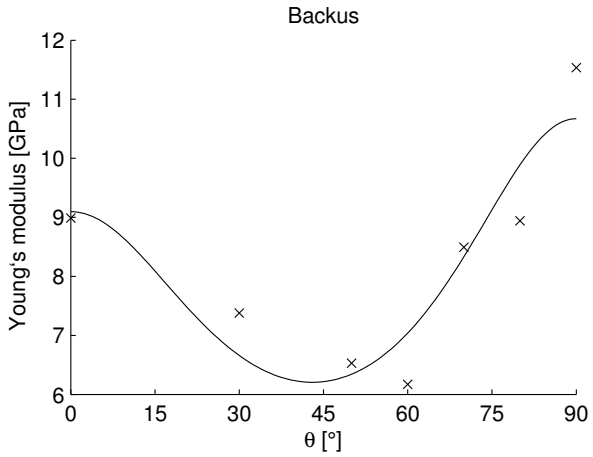

G_1 = 4.3822 GPa
λ_1 = 0.0002081 GPa
x = 0.89271
f = 0.018717
g = 1.5139
f = 0.018717
RSS = 0.4274 GPa^2
M = 2.992 GPa^2

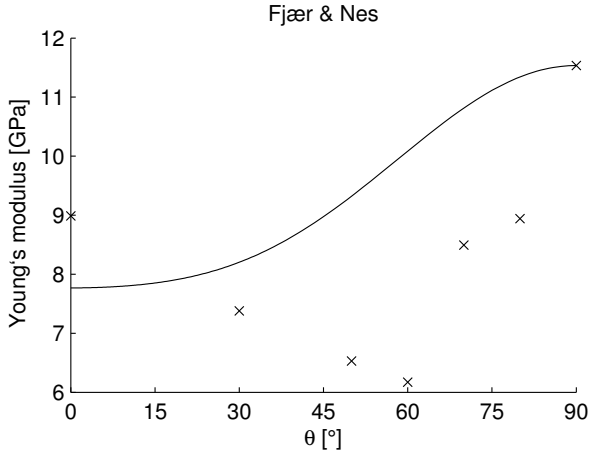

E_0 = 11.5355 GPa
ρ = 0.32661
η_0 = 0.14028
RSS = 5.21 GPa^2
M = 12.156 GPa^2

Tournemire shale (Data after Niandou et al., 1994)

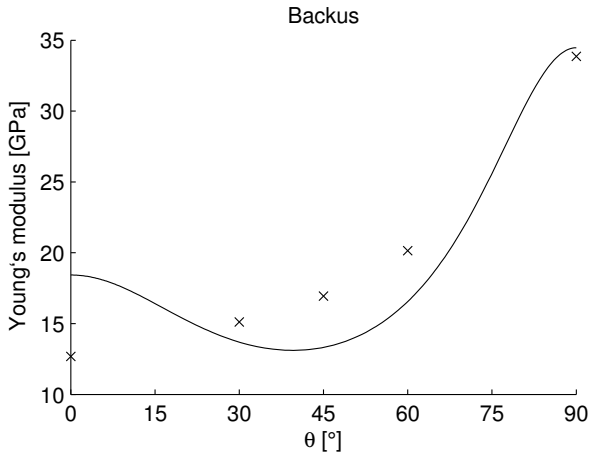

G_1 = 13.8067 GPa
λ_1 = 0 GPa
x = 0.11389
f = 0.018717
g = 0.64011
f = 0.018717
RSS = 12.73 GPa^2
M = –63.64 GPa^2

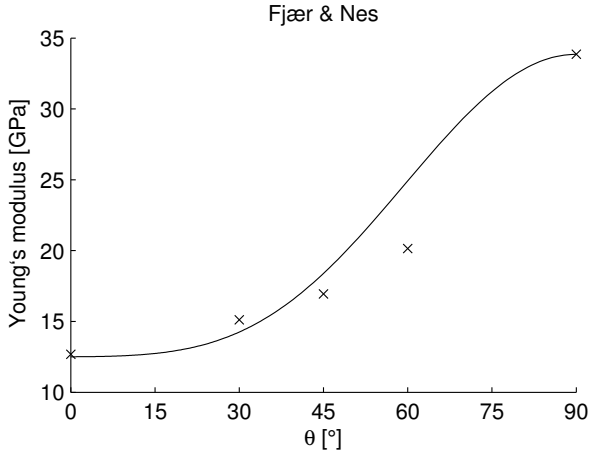

E_0 = 33.855 GPa
ρ = 0.63053
η_0 = 0.29916
RSS = 25.74 GPa^2
M = 5.148 GPa^2

Mancos shale (Data after Fjær & Nes, 2013)

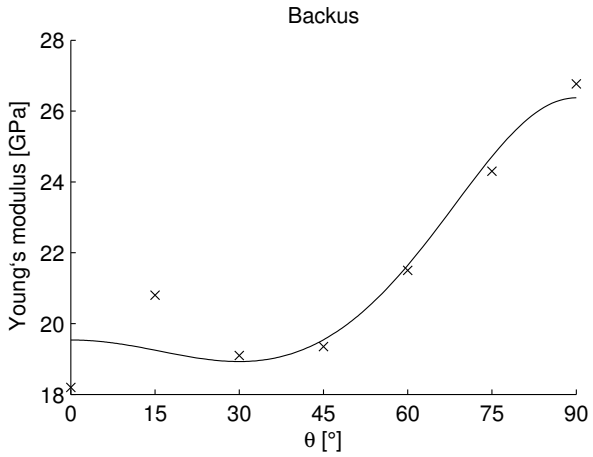

G_1 = 12.9708 GPa
λ_1 = 21.0985 GPa
x = 1.4222
f = 0.1212
g = 1.9441
f = 0.1212
RSS = 0.6583 GPa^2
M = 4.609 GPa^2

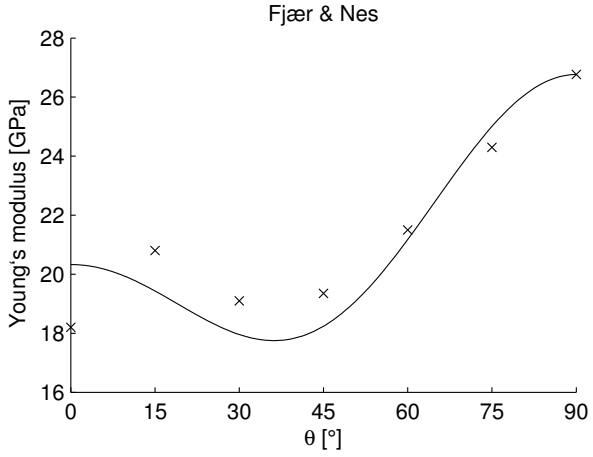

E_0 = 26.7667 GPa
ρ = 0.24054
η_0 = 0.25844
RSS = 1.762 GPa^2
M = 4.111 GPa^2

Appendix B Calculations

B.1 Derivation of effective stiffness in Backus' model

```
> with(linalg) :
> l[xx] := cos(theta); l[yx] := 0; l[zx] := sin(theta); l[xy] := 1; l[yy] := 1; l[zy] := 0; l[xz] :=
      -sin(theta); l[yz] := 0; l[zz] := cos(theta)
```

$$l_{xx} := \cos(\theta)$$
$$l_{yx} := 0$$
$$l_{zx} := \sin(\theta)$$
$$l_{xy} := 1$$
$$l_{yy} := 1$$
$$l_{zy} := 0$$
$$l_{xz} := -\sin(\theta)$$
$$l_{yz} := 0$$
$$l_{zz} := \cos(\theta) \quad (1)$$

```
> l[xX] := cos(-theta); l[yX] := 0; l[zX] := sin(-theta); l[xY] := 1; l[yY] := 1; l[zY] := 0;
      l[xZ] := -sin(-theta); l[yZ] := 0; l[zZ] := cos(-theta)
```

$$l_{xX} := \cos(\theta)$$
$$l_{yX} := 0$$
$$l_{zX} := -\sin(\theta)$$
$$l_{xY} := 1$$
$$l_{yY} := 1$$
$$l_{zY} := 0$$
$$l_{xZ} := \sin(\theta)$$
$$l_{yZ} := 0$$
$$l_{zZ} := \cos(\theta) \quad (2)$$

```
> A := matrix(6, 6, [C[11], C[12], C[13], 0, 0, 0, C[12], C[22], C[23], 0, 0, 0, C[13], C[23],
      C[33], 0, 0, 0, 0, 0, 0, C[44], 0, 0, 0, 0, 0, 0, C[55], 0, 0, 0, 0, 0, 0, C[66]]);
```

$$A := \begin{bmatrix} C_{11} & C_{12} & C_{13} & 0 & 0 & 0 \\ C_{12} & C_{22} & C_{23} & 0 & 0 & 0 \\ C_{13} & C_{23} & C_{33} & 0 & 0 & 0 \\ 0 & 0 & 0 & C_{44} & 0 & 0 \\ 0 & 0 & 0 & 0 & C_{55} & 0 \\ 0 & 0 & 0 & 0 & 0 & C_{66} \end{bmatrix} \quad (3)$$

```
> R1 := matrix(6, 6, [l[xx]^2, l[xy]^2, l[xz]^2, 2·l[xy]·l[xz], 2·l[xx]·l[xz], 2·l[xx]·l[xy], l[yx]^2,
      l[yy]^2, l[yz]^2, 2·l[yy]·l[yz], 2·l[yx]·l[yz], 2·l[yx]·l[yy], l[zx]^2, l[zy]^2, l[zz]^2, 2·l[zy]·l[zz], 2
      ·l[zx]·l[zz], 2·l[zx]·l[zy], l[yx]·l[zx], l[yy]·l[zy], l[yz]·l[zz], l[yy]·l[zz] + l[yz]·l[zy], l[yx]
```

$$\cdot l[zz] + l[yz]\cdot l[zx],\ l[yx]\cdot l[zy] + l[yy]\cdot l[zx],\ l[xx]\cdot l[zx],\ l[xy]\cdot l[zy],\ l[xz]\cdot l[zz],\ l[xy]\cdot l[zz] + l[xz]\cdot l[zy],\ l[xx]\cdot l[zz] + l[xz]\cdot l[zx],\ l[xx]\cdot l[zy] + l[xy]\cdot l[zx],\ l[xx]\cdot l[yx],\ l[xy]\cdot l[yy],\ l[xz]\cdot l[yz],\ l[xy]\cdot l[yz] + l[xz]\cdot l[yy],\ l[xx]\cdot l[yz] + l[xz]\cdot l[yx],\ l[xx]\cdot l[yy] + l[xy]\cdot l[yx]\big]\big)$$

$$R1 := \begin{bmatrix} \cos(\theta)^2 & 1 & \sin(\theta)^2 & -2\sin(\theta) & -2\cos(\theta)\sin(\theta) & 2\cos(\theta) \\ 0 & 1 & 0 & 0 & 0 & 0 \\ \sin(\theta)^2 & 0 & \cos(\theta)^2 & 0 & 2\cos(\theta)\sin(\theta) & 0 \\ 0 & 0 & 0 & \cos(\theta) & 0 & \sin(\theta) \\ \cos(\theta)\sin(\theta) & 0 & -\cos(\theta)\sin(\theta) & \cos(\theta) & \cos(\theta)^2 - \sin(\theta)^2 & \sin(\theta) \\ 0 & 1 & 0 & -\sin(\theta) & 0 & \cos(\theta) \end{bmatrix} \quad (4)$$

> $R2 := matrix\big(6, 6, \big[l[xX]^2, l[xY]^2, l[xZ]^2, 2\cdot l[xY]\cdot l[xZ], 2\cdot l[xX]\cdot l[xZ], 2\cdot l[xX]\cdot l[xY], l[yX]^2, l[yY]^2, l[yZ]^2, 2\cdot l[yY]\cdot l[yZ], 2\cdot l[yX]\cdot l[yZ], 2\cdot l[yX]\cdot l[yY], l[zX]^2, l[zY]^2, l[zZ]^2, 2\cdot l[zY]\cdot l[zZ], 2\cdot l[zX]\cdot l[zZ], 2\cdot l[zX]\cdot l[zY], l[yX]\cdot l[zX], l[yY]\cdot l[zY], l[yZ]\cdot l[zZ], l[yY]\cdot l[zZ] + l[yZ]\cdot l[zY], l[yX]\cdot l[zZ] + l[yZ]\cdot l[zX], l[yX]\cdot l[zY] + l[yY]\cdot l[zX], l[xX]\cdot l[zX], l[xY]\cdot l[zY], l[xZ]\cdot l[zZ], l[xY]\cdot l[zZ] + l[xZ]\cdot l[zY], l[xX]\cdot l[zZ] + l[xZ]\cdot l[zX], l[xX]\cdot l[zY] + l[xY]\cdot l[zX], l[xX]\cdot l[yX], l[xY]\cdot l[yY], l[xZ]\cdot l[yZ], l[xY]\cdot l[yZ] + l[xZ]\cdot l[yY], l[xX]\cdot l[yZ] + l[xZ]\cdot l[yX], l[xX]\cdot l[yY] + l[xY]\cdot l[yX]\big]\big)$

$$R2 := \begin{bmatrix} \cos(\theta)^2 & 1 & \sin(\theta)^2 & 2\sin(\theta) & 2\cos(\theta)\sin(\theta) & 2\cos(\theta) \\ 0 & 1 & 0 & 0 & 0 & 0 \\ \sin(\theta)^2 & 0 & \cos(\theta)^2 & 0 & -2\cos(\theta)\sin(\theta) & 0 \\ 0 & 0 & 0 & \cos(\theta) & 0 & -\sin(\theta) \\ -\cos(\theta)\sin(\theta) & 0 & \cos(\theta)\sin(\theta) & \cos(\theta) & \cos(\theta)^2 - \sin(\theta)^2 & -\sin(\theta) \\ 0 & 1 & 0 & \sin(\theta) & 0 & \cos(\theta) \end{bmatrix} \quad (5)$$

> $C2 := \text{multiply}(R1, A, R2)$:

> $P := linalg['inverse'](C2)$:

> $\sigma xx := sigma3;\ \sigma yy := sigma3;\ \tau yz := 0;\ \tau xz := 0;\ \tau xy := 0;\ sigma3 := 0$

$$\sigma xx := \sigma 3$$
$$\sigma yy := \sigma 3$$
$$\tau yz := 0$$
$$\tau xz := 0$$
$$\tau xy := 0$$
$$\sigma 3 := 0 \quad (6)$$

> $\text{sigma} := matrix(6, 1, [\sigma xx, \sigma yy, \sigma zz, \tau yz, \tau xz, \tau xy])$

$$\sigma := \begin{bmatrix} 0 \\ 0 \\ \sigma zz \\ 0 \\ 0 \\ 0 \end{bmatrix} \tag{7}$$

> epsilon := *multiply*(*P*, sigma) :

>

> lambda[2] := $f \cdot$lambda[1]; $G[2] := G[1] \cdot g$

$$\lambda_2 := f\,\lambda_1$$
$$G_2 := G_1\,g \tag{8}$$

> $C[22] := C[11]$:

> $C[11] := x \cdot \frac{4 \cdot G[1] \cdot (\text{lambda}[1] + G[1])}{\text{lambda}[1] + 2 \cdot G[1]} + (1-x) \cdot \frac{4\,G[2] \cdot (\text{lambda}[2] + G[2])}{\text{lambda}[2] + G[2]} + \left(x \cdot \frac{1}{\text{lambda}[1] + 2 \cdot G[1]} + (1-x) \cdot \frac{1}{\text{lambda}[2] + 2\,G[2]} \right)^{-1} \cdot \left(\frac{x \cdot \text{lambda}[1]}{\text{lambda}[1] + 2 \cdot G[1]} + \frac{(1-x) \cdot \text{lambda}[2]}{\text{lambda}[2] + 2\,G[2]} \right)^2$:

> $C[33] := \left(x \cdot \frac{1}{\text{lambda}[1] + 2 \cdot G[1]} + (1-x) \cdot \frac{1}{\text{lambda}[2] + 2\,G[2]} \right)^{-1}$:

> $C[12] := \left(x \cdot \frac{2 \cdot G[1] \cdot \text{lambda}[1]}{\text{lambda}[1] + 2 \cdot G[1]} + (1-x) \cdot \frac{2 \cdot G[2] \cdot \text{lambda}[2]}{\text{lambda}[2] + 2 \cdot G[2]} \right) + \left(x \cdot \frac{1}{\text{lambda}[1] + 2 \cdot G[1]} + (1-x) \cdot \frac{1}{\text{lambda}[2] + 2\,G[2]} \right)^{-1} \cdot \left(\frac{x \cdot \text{lambda}[1]}{\text{lambda}[1] + 2 \cdot G[1]} + \frac{(1-x) \cdot \text{lambda}[2]}{\text{lambda}[2] + 2\,G[2]} \right)^2$:

> $C[13] := \left(x \cdot \frac{1}{\text{lambda}[1] + 2 \cdot G[1]} + (1-x) \cdot \frac{1}{\text{lambda}[2] + 2\,G[2]} \right)^{-1} \cdot \left(\frac{x \cdot \text{lambda}[1]}{\text{lambda}[1] + 2 \cdot G[1]} + \frac{(1-x) \cdot \text{lambda}[2]}{\text{lambda}[2] + 2\,G[2]} \right)$:

> $C[23] := C[13]$:

> $C[55] := \left(x \cdot \frac{1}{G[1]} + \frac{(1-x) \cdot 1}{G[2]} \right)^{-1}$:

> $C[44] := C[55]$:

> $C[66] := x \cdot G[1] + (1-x) \cdot G[2]$:

> *Eeff* := *simplify*$\left(\frac{\sigma zz}{\text{epsilon}[3,1]}, \text{'size'} \right)$

$$Eeff := \left(2\,g \left(\cos(\theta)^2 + \sin(\theta)^2 \right)^4 \left(\left(\frac{1}{2} f\,(g-1)\,\lambda_1^2 + \left(\frac{2}{3} g^2 + (f-1)\,g - \frac{1}{3} f \right) G_1\,\lambda_1 + \frac{4}{3} g \left(g - \frac{1}{2} \right) G_1^2 \right) x - g \left(f\lambda_1 + \frac{4}{3} G_1 g \right) \left(\frac{1}{2} \lambda_1 + G_1 \right) \right) \left(f\lambda_1 + 2\,g\,G_1 \right) G_1 \right) / \tag{9}$$

$$\left(g\left(\left(f\left(g-1\right)\left(f-1\right)\lambda_1^2+\frac{10}{3}\left(\left(-\frac{4}{5}+f\right)g^2+\left(\frac{3}{5}-f\right)g+\frac{1}{5}f\right)G_1\lambda_1\right.\right.\right.$$
$$\left.+\frac{8}{3}g\left(g-1\right)\left(g-\frac{1}{2}\right)G_1^2\right)G_1x^2-\left(\left(\left(f-\frac{2}{3}\right)g-\frac{4}{3}f+1\right)f\lambda_1^2+\frac{10}{3}\left(\left(-\frac{4}{5}\right.\right.\right.$$
$$\left.+f\right)g^2+\left(\frac{3}{5}-\frac{6}{5}f\right)g+\frac{1}{5}f\right)G_1\lambda_1+\frac{8}{3}g\left(g^2-2g+\frac{1}{2}\right)G_1^2\left.\right)G_1x-\frac{2}{3}\left(f^2\lambda_1^2\right.$$
$$\left.\left.+3fgG_1\lambda_1+4g^2G_1^2\right)\left(\frac{1}{2}\lambda_1+G_1\right)\right)\cos\left(\theta\right)^4+4\sin\left(\theta\right)^2\left(\left(\frac{1}{2}f\left(g-1\right)\lambda_1^2\right.\right.$$
$$\left.+\left(\frac{2}{3}g^2+\left(f-1\right)g-\frac{1}{3}f\right)G_1\lambda_1+\frac{4}{3}g\left(g-\frac{1}{2}\right)G_1^2\right)\left(g-1\right)x^2+\left(-\frac{1}{2}f\left(g\right.\right.$$
$$\left.\left.-1\right)^2\lambda_1^2-\left(\frac{2}{3}g^3+\left(-\frac{19}{12}+f\right)g^2+\left(1-\frac{7}{4}f\right)g+\frac{1}{3}f\right)G_1\lambda_1-\frac{4}{3}g\left(g^2-2g\right.\right.$$
$$\left.\left.\left.+\frac{1}{2}\right)G_1^2\right)x-\frac{3}{4}g\left(f\lambda_1+\frac{16}{9}G_1g\right)\left(\frac{1}{2}\lambda_1+G_1\right)\right)\left(f\lambda_1+2gG_1\right)\cos\left(\theta\right)^2$$
$$\left.-\frac{1}{3}g\sin\left(\theta\right)^4\left(f\lambda_1+2gG_1\right)^2\left(\frac{1}{2}\lambda_1+G_1\right)\right)$$

>

B.2 Derivation of the major principal stress in Cazacu et al.'s model

> $b[1] := (1/X[c]) - (1/X[t])$

$$b_1 := \frac{1}{X_c} - \frac{1}{X_t} \tag{1}$$

> $b[2] := (1/Y[c]) - (1/Y[t])$

$$b_2 := \frac{1}{Y_c} - \frac{1}{Y_t} \tag{2}$$

> $B[11] := 1/(X[t]*X[c])$

$$B_{11} := \frac{1}{X_t X_c} \tag{3}$$

> $B[22] := 1/(Y[t]*Y[c])$

$$B_{22} := \frac{1}{Y_t Y_c} \tag{4}$$

> $B[44] := 4\cdot B[22] - B[11]$

$$B_{44} := \frac{4}{Y_t Y_c} - \frac{1}{X_t X_c} \tag{5}$$

> $B[55] := 3*c\text{^}2$

$$B_{55} := 3\,c^2 \tag{6}$$

> $B[23] := -B[22] + \frac{B[11]}{2}$

$$B_{23} := -\frac{1}{Y_t Y_c} + \frac{1}{2\,X_t X_c} \tag{7}$$

> $B[12] := -\frac{1}{2}\cdot B[11]$

$$B_{12} := -\frac{1}{2\,X_t X_c} \tag{8}$$

> $A[11] := B[11]\cdot\cos(\text{theta})^4 + B[22]\cdot\sin^4(\text{theta}) + (2\cdot B[12] + B[55])\cdot\sin(\text{theta})^2 \cdot\cos(\text{theta})^2$

$$A_{11} := \frac{\cos(\theta)^4}{X_t X_c} + \frac{\sin(\theta)^4}{Y_t Y_c} + \left(-\frac{1}{X_t X_c} + 3\,c^2\right)\sin(\theta)^2\cos(\theta)^2 \tag{9}$$

> $A[22] := B[22]$

$$A_{22} := \frac{1}{Y_t Y_c} \tag{10}$$

> $A[33] := B[11]\cdot\sin(\text{theta})^4 + B[22]\cdot\cos(\text{theta})^4 + (2\cdot B[12] + B[55])\cdot\sin(\text{theta})^2 \cdot\cos(\text{theta})^2$

$$A_{33} := \frac{\sin(\theta)^4}{X_t X_c} + \frac{\cos(\theta)^4}{Y_t Y_c} + \left(-\frac{1}{X_t X_c} + 3\,c^2\right)\sin(\theta)^2\cos(\theta)^2 \tag{11}$$

>

> $A[12] := B[23]\cdot\sin(\text{theta})^2 + B[12]\cdot\cos(\text{theta})^2$

(12)

$$A_{12} := \left(-\frac{1}{Y_t Y_c} + \frac{1}{2 X_t X_c} \right) \sin(\theta)^2 - \frac{1}{2} \frac{\cos(\theta)^2}{X_t X_c} \tag{12}$$

> $A[13] := (B[11] + B[22] - B[55] - 2 \cdot B[12]) \cdot \sin(\text{theta})^2 \cdot \cos(\text{theta})^2 + B[12]$

$$A_{13} := \left(\frac{2}{X_t X_c} + \frac{1}{Y_t Y_c} - 3\,c^2 \right) \sin(\theta)^2 \cos(\theta)^2 - \frac{1}{2 X_t X_c} \tag{13}$$

> $A[23] := B[12] \cdot \sin(\text{theta})^2 + B[23] \cdot \cos(\text{theta})^2$

$$A_{23} := -\frac{1}{2} \frac{\sin(\theta)^2}{X_t X_c} + \left(-\frac{1}{Y_t Y_c} + \frac{1}{2 X_t X_c} \right) \cos(\theta)^2 \tag{14}$$

> $a[1] := b[1] \cdot \cos(\text{theta})^2 + b[2] \cdot \sin(\text{theta})^2$

$$a_1 := \left(\frac{1}{X_c} - \frac{1}{X_t} \right) \cos(\theta)^2 + \left(\frac{1}{Y_c} - \frac{1}{Y_t} \right) \sin(\theta)^2 \tag{15}$$

> $a[2] := b[2]$

$$a_2 := \frac{1}{Y_c} - \frac{1}{Y_t} \tag{16}$$

> $a[3] := b[1] \cdot \sin(\text{theta})^2 + a[2] \cdot \cos(\text{theta})^2$

$$a_3 := \left(\frac{1}{X_c} - \frac{1}{X_t} \right) \sin(\theta)^2 + \left(\frac{1}{Y_c} - \frac{1}{Y_t} \right) \cos(\theta)^2 \tag{17}$$

> $\text{sigma}[2] = \text{sigma}[1]$

$$\sigma_2 = \sigma_1 \tag{18}$$

> $f := a[1] \cdot \text{sigma}[1] + a[2] \cdot \text{sigma}[2] + a[3] \cdot \text{sigma}[3] + A[11] \cdot \text{sigma}[1]^2 + A[22] \cdot \text{sigma}[2]^2 + A[33] \cdot \text{sigma}[3]^2 + 2 \cdot A[12] \cdot \text{sigma}[1] \cdot \text{sigma}[2] + 2 \cdot A[13] \cdot \text{sigma}[3] \cdot \text{sigma}[1] + 2 \cdot A[23] \cdot \text{sigma}[2] \cdot \text{sigma}[3] - 1$

$$f := \left(\frac{\cos(\theta)^4}{X_t X_c} + \frac{\sin(\theta)^4}{Y_t Y_c} + \left(-\frac{1}{X_t X_c} + 3\,c^2 \right) \sin(\theta)^2 \cos(\theta)^2 \right) \sigma_1^2 + 2 \left(\left(-\frac{1}{Y_t Y_c} + \frac{1}{2 X_t X_c} \right) \sin(\theta)^2 - \frac{1}{2} \frac{\cos(\theta)^2}{X_t X_c} \right) \sigma_1 \sigma_2 + 2 \left(\left(\frac{2}{X_t X_c} + \frac{1}{Y_t Y_c} - 3\,c^2 \right) \sin(\theta)^2 \cos(\theta)^2 - \frac{1}{2 X_t X_c} \right) \sigma_1 \sigma_3 + \frac{\sigma_2^2}{Y_t Y_c} + 2 \left(-\frac{1}{2} \frac{\sin(\theta)^2}{X_t X_c} + \left(-\frac{1}{Y_t Y_c} + \frac{1}{2 X_t X_c} \right) \cos(\theta)^2 \right) \sigma_2 \sigma_3 + \left(\frac{\sin(\theta)^4}{X_t X_c} + \frac{\cos(\theta)^4}{Y_t Y_c} + \left(-\frac{1}{X_t X_c} + 3\,c^2 \right) \sin(\theta)^2 \cos(\theta)^2 \right) \sigma_3^2 + \left(\left(\frac{1}{X_c} - \frac{1}{X_t} \right) \cos(\theta)^2 + \left(\frac{1}{Y_c} - \frac{1}{Y_t} \right) \sin(\theta)^2 \right) \sigma_1 + \left(\frac{1}{Y_c} - \frac{1}{Y_t} \right) \sigma_2 + \left(\left(\frac{1}{X_c} - \frac{1}{X_t} \right) \sin(\theta)^2 + \left(\frac{1}{Y_c} - \frac{1}{Y_t} \right) \cos(\theta)^2 \right) \sigma_3 - 1 \tag{19}$$

> $f := solve(f, [\sigma[3]])$:

> $simplify(\{f\}, 'size')$

$$\left\{\left\{\left\{\sigma_3 \right.\right.\right. \tag{20}$$

$$= \left(\left(\left(\left(\left(\left(-12\, c^2 X_t^2 - 12\, c^2 X_t \sigma_1 + 1 \right) X_c^2 + \left(12\, c^2 X_t^2 \sigma_1 + 6 X_t + 4 \sigma_1 + 4 \sigma_2 \right) X_c + \right. \right. \right. \right. \right.$$

$$\left. X_t^2 + \left(-4 \sigma_1 - 4 \sigma_2 \right) X_t + 4 \left(\sigma_1 - \sigma_2 \right)^2 \right) Y_t^2 - 12 X_t \left(\left(\frac{1}{6} + c^2 \left(\sigma_1 + \sigma_2 \right) X_t \right) X_c - \sigma_1 \right.$$

$$\left. - \frac{1}{3} \sigma_2 - \frac{1}{6} X_t \right) X_c Y_t + X_c^2 X_t^2 \Big) Y_c^2 + 12 X_t \left(\left(\left(\frac{1}{6} + c^2 \left(\sigma_1 + \sigma_2 \right) X_t \right) X_c - \sigma_1 - \frac{1}{3} \sigma_2 \right. \right.$$

$$\left. \left. - \frac{1}{6} X_t \right) Y_t^2 + \left(\left(\left(c^2 \sigma_2^2 + \frac{1}{6} - 2\, c^2 \sigma_1 \sigma_2 + c^2 \sigma_1^2 \right) X_t - \frac{1}{3} \sigma_2 + \frac{2}{3} \sigma_1 \right) X_c + \left(-\frac{2}{3} \sigma_1 \right. \right.$$

$$\left. \left. + \frac{1}{3} \sigma_2 \right) X_t - \frac{4}{3} \left(\sigma_1 - \sigma_2 \right)^2 \right) Y_t + \frac{2}{3} \sigma_2 X_t X_c \Big) X_c Y_c + X_c^2 X_t^2 Y_t \left(Y_t - 8 \sigma_2 \right) \Big) \sin(\theta)^4$$

$$+ \left(\left(\left(12\, c^2 X_t \left(X_t + \sigma_1 \right) X_c^2 + \left(-12\, c^2 X_t^2 \sigma_1 - 4 X_t - 2 \sigma_1 - 2 \sigma_2 \right) X_c + \left(2 \sigma_1 + 2 \sigma_2 \right) X_t \right. \right. \right.$$

$$\left. \left. - 4 \left(\sigma_1 - \sigma_2 \right)^2 \right) Y_t^2 + 12 X_t \left(\left(\frac{1}{6} + c^2 \left(\sigma_1 + \sigma_2 \right) X_t \right) X_c - \frac{5}{6} \sigma_1 + \frac{1}{6} \sigma_2 - \frac{1}{6} X_t \right) X_c Y_t \right.$$

$$\left. - 2 X_c^2 X_t^2 \right) Y_c^2 - 12 X_t \left(\left(\left(\frac{1}{6} + c^2 \left(\sigma_1 + \sigma_2 \right) X_t \right) X_c - \frac{5}{6} \sigma_1 + \frac{1}{6} \sigma_2 - \frac{1}{6} X_t \right) Y_t^2 \right.$$

$$+ \left(\left(\left(c^2 \sigma_2^2 + \frac{1}{3} - 2\, c^2 \sigma_1 \sigma_2 + c^2 \sigma_1^2 \right) X_t - \frac{1}{3} \sigma_2 + \sigma_1 \right) X_c + \left(-\sigma_1 + \frac{1}{3} \sigma_2 \right) X_t \right.$$

$$\left. \left. - \frac{4}{3} \left(\sigma_1 - \sigma_2 \right)^2 \right) Y_t + \frac{4}{3} \sigma_2 X_t X_c \Big) X_c Y_c - 2 X_c^2 X_t^2 Y_t \left(Y_t - 8 \sigma_2 \right) \Big) \sin(\theta)^2 + \left(\left(\sigma_1 \right. \right.$$

$$-\sigma_2)\,Y_t + X_t X_c)^2\,Y_c^2 + 2\,X_t\left(\left(-\sigma_1+\sigma_2\right)Y_t^2 + \left(\left(X_t+2\,\sigma_1\right)X_c - 2\,X_t\sigma_1 - 2\,(\sigma_1$$

$$-\sigma_2)^2\right)Y_t + 4\,\sigma_2 X_t X_c\right)X_c Y_c + X_c^2 X_t^2 Y_t\left(Y_t - 8\,\sigma_2\right)\Big)^{1/2} + \left(\left(6\,c^2 Y_c Y_t\sigma_1 - 2\,\sigma_1\right)X_t X_c$$

$$-4\,\sigma_1 Y_t Y_c\right)\sin(\theta)^4 + \left(\left(\left(\left(-6\,c^2 Y_t\sigma_1 + 1\right)Y_c - Y_t + 2\,\sigma_1 + 2\,\sigma_2\right)X_t - Y_t Y_c\right)X_c$$

$$+X_t Y_c Y_t + \left(4\,\sigma_1 - 2\,\sigma_2\right)Y_t Y_c\right)\sin(\theta)^2 + \left(-Y_c + Y_t - 2\,\sigma_2\right)X_t X_c + \left(-\sigma_1+\sigma_2\right)Y_t Y_c\Big)$$

$$\Big/\left(\left(\left(6\,c^2 Y_c Y_t - 2\right)X_t X_c - 4\,Y_t Y_c\right)\sin(\theta)^4 + \left(\left(-6\,c^2 Y_c Y_t + 4\right)X_t X_c + 2\,Y_t Y_c\right)\sin(\theta)^2$$

$$-2\,X_t X_c\right)\Big],\left[\sigma_3 = \Big(\right.$$

$$-\Big(\left(\left(\left(\left(-12\,c^2 X_t^2 - 12\,c^2 X_t\sigma_1 + 1\right)X_c^2 + \left(12\,c^2 X_t^2\sigma_1 + 6\,X_t + 4\,\sigma_1 + 4\,\sigma_2\right)X_c\right.\right.\right.$$

$$\left.+X_t^2 + \left(-4\,\sigma_1 - 4\,\sigma_2\right)X_t + 4\,(\sigma_1-\sigma_2)^2\right)Y_t^2 - 12\,X_t\left(\left(\frac{1}{6} + c^2\left(\sigma_1+\sigma_2\right)X_t\right)X_c - \sigma_1\right.$$

$$\left.-\frac{1}{3}\,\sigma_2 - \frac{1}{6}\,X_t\right)X_c Y_t + X_c^2 X_t^2\Big)Y_c^2 + 12\,X_t\left(\left(\left(\frac{1}{6} + c^2\left(\sigma_1+\sigma_2\right)X_t\right)X_c - \sigma_1 - \frac{1}{3}\,\sigma_2\right.\right.$$

$$\left.-\frac{1}{6}\,X_t\right)Y_t^2 + \left(\left(\left(c^2\sigma_2^2 + \frac{1}{6} - 2\,c^2\sigma_1\sigma_2 + c^2\sigma_1^2\right)X_t - \frac{1}{3}\,\sigma_2 + \frac{2}{3}\,\sigma_1\right)X_c + \left(-\frac{2}{3}\,\sigma_1\right.$$

$$\left.+\frac{1}{3}\,\sigma_2\right)X_t - \frac{4}{3}\,(\sigma_1-\sigma_2)^2\Big)Y_t + \frac{2}{3}\,\sigma_2 X_t X_c\Big)X_c Y_c + X_c^2 X_t^2 Y_t\left(Y_t - 8\,\sigma_2\right)\Big)\sin(\theta)^4$$

$$+\Big(\left(\left(12\,c^2 X_t\left(X_t+\sigma_1\right)X_c^2 + \left(-12\,c^2 X_t^2\sigma_1 - 4\,X_t - 2\,\sigma_1 - 2\,\sigma_2\right)X_c + \left(2\,\sigma_1 + 2\,\sigma_2\right)X_t\right.\right.$$

$$\left.-4\,(\sigma_1-\sigma_2)^2\right)Y_t^2 + 12\,X_t\left(\left(\frac{1}{6} + c^2\left(\sigma_1+\sigma_2\right)X_t\right)X_c - \frac{5}{6}\,\sigma_1 + \frac{1}{6}\,\sigma_2 - \frac{1}{6}\,X_t\right)X_c Y_t$$

$$\left.-2\,X_c^2 X_t^2\right)Y_c^2 - 12\,X_t\left(\left(\left(\frac{1}{6} + c^2\left(\sigma_1+\sigma_2\right)X_t\right)X_c - \frac{5}{6}\,\sigma_1 + \frac{1}{6}\,\sigma_2 - \frac{1}{6}\,X_t\right)Y_t^2\right.$$

$$+\left(\left(\left(c^2\sigma_2^2 + \frac{1}{3} - 2\,c^2\sigma_1\sigma_2 + c^2\sigma_1^2\right)X_t - \frac{1}{3}\,\sigma_2 + \sigma_1\right)X_c + \left(-\sigma_1 + \frac{1}{3}\,\sigma_2\right)X_t\right.$$

$$-\frac{4}{3}\left(\sigma_1-\sigma_2\right)^2\Big)Y_t+\frac{4}{3}\sigma_2 X_t X_c\Big)X_c Y_c-2X_c^2X_t^2Y_t\left(Y_t-8\sigma_2\right)\Big)\sin(\theta)^2+\Big(\left(\sigma_1$$

$$-\sigma_2\right)Y_t+X_t X_c\Big)^2Y_c^2+2X_t\Big(\left(-\sigma_1+\sigma_2\right)Y_t^2+\Big(\left(X_t+2\sigma_1\right)X_c-2X_t\sigma_1-2\left(\sigma_1$$

$$-\sigma_2\right)^2\Big)Y_t+4\sigma_2 X_t X_c\Big)X_c Y_c+X_c^2X_t^2Y_t\left(Y_t-8\sigma_2\right)\Big)^{1/2}+\Big(\left(6c^2Y_c Y_t\sigma_1-2\sigma_1\right)X_t X_c$$

$$-4\sigma_1 Y_t Y_c\Big)\sin(\theta)^4+\Big(\Big(\Big(\left(-6c^2Y_t\sigma_1+1\right)Y_c-Y_t+2\sigma_1+2\sigma_2\Big)X_t-Y_t Y_c\Big)X_c$$

$$+X_t Y_c Y_t+\left(4\sigma_1-2\sigma_2\right)Y_t Y_c\Big)\sin(\theta)^2+\left(-Y_c+Y_t-2\sigma_2\right)X_t X_c+\left(-\sigma_1+\sigma_2\right)Y_t Y_c\Big)$$

$$\Big/\Big(\Big(\left(6c^2Y_c Y_t-2\right)X_t X_c-4Y_t Y_c\Big)\sin(\theta)^4+\Big(\left(-6c^2Y_c Y_t+4\right)X_t X_c+2Y_t Y_c\Big)\sin(\theta)^2$$

$$-2X_t X_c\Big)\Big]\Big]\Big\}$$

>

B.3 Derivation of principal stress directions used in predicting borehole stability

```
> with(linalg):
> R[z](a) := matrix(3, 3, [cos(a), sin(a), 0, -sin(a), cos(a), 0, 0, 0, 1])
```

$$R_z(a) := \begin{bmatrix} \cos(a) & \sin(a) & 0 \\ -\sin(a) & \cos(a) & 0 \\ 0 & 0 & 1 \end{bmatrix} \quad (1)$$

```
> R[y](i) := matrix(3, 3, [cos(i), 0, -sin(i), 0, 1, 0, sin(i), 0, cos(i)])
```

$$R_y(i) := \begin{bmatrix} \cos(i) & 0 & -\sin(i) \\ 0 & 1 & 0 \\ \sin(i) & 0 & \cos(i) \end{bmatrix} \quad (2)$$

```
> R[z](theta) := matrix(3, 3, [cos(theta), sin(theta), 0, -sin(theta), cos(theta), 0, 0, 0, 1])
```

$$R_z(\theta) := \begin{bmatrix} \cos(\theta) & \sin(\theta) & 0 \\ -\sin(\theta) & \cos(\theta) & 0 \\ 0 & 0 & 1 \end{bmatrix} \quad (3)$$

```
> A := multiply(R[z](theta), R[y](i), R[z](a))
```

$$A := [[\cos(\theta)\cos(i)\cos(a) - \sin(\theta)\sin(a), \cos(\theta)\cos(i)\sin(a) + \sin(\theta)\cos(a), -\cos(\theta)\sin(i)], [-\sin(\theta)\cos(i)\cos(a) - \cos(\theta)\sin(a), -\sin(\theta)\cos(i)\sin(a) + \cos(\theta)\cos(a), \sin(\theta)\sin(i)], [\sin(i)\cos(a), \sin(i)\sin(a), \cos(i)]] \quad (4)$$

```
> sigma[r] := Vector([A[1, 1], A[1, 2], A[1, 3]])
```

$$\sigma_r := \begin{bmatrix} \cos(\theta)\cos(i)\cos(a) - \sin(\theta)\sin(a) \\ \cos(\theta)\cos(i)\sin(a) + \sin(\theta)\cos(a) \\ -\cos(\theta)\sin(i) \end{bmatrix} \quad (5)$$

```
> R[x](phi) := matrix(3, 3, [1, 0, 0, 0, cos(phi), -sin(phi), 0, sin(phi), cos(phi)])
```

$$R_x(\phi) := \begin{bmatrix} 1 & 0 & 0 \\ 0 & \cos(\phi) & -\sin(\phi) \\ 0 & \sin(\phi) & \cos(\phi) \end{bmatrix} \quad (6)$$

```
> B := multiply(R[x](phi), R[z](theta), R[y](i), R[z](a))
```

$$B := [[\cos(\theta)\cos(i)\cos(a) - \sin(\theta)\sin(a), \cos(\theta)\cos(i)\sin(a) + \sin(\theta)\cos(a), -\cos(\theta)\sin(i)], [(-\cos(\phi)\sin(\theta)\cos(i) - \sin(\phi)\sin(i))\cos(a) - \cos(\phi)\cos(\theta)\sin(a), (-\cos(\phi)\sin(\theta)\cos(i) - \sin(\phi)\sin(i))\sin(a) + \cos(\phi)\cos(\theta)\cos(a), \cos(\phi)\sin(\theta)\sin(i) - \sin(\phi)\cos(i)], [(-\sin(\phi)\sin(\theta)\cos(i) + \cos(\phi)\sin(i))\cos(a) - \sin(\phi)\cos(\theta)\sin(a), (\quad (7)$$

$$-\sin(\phi)\sin(\theta)\cos(i)+\cos(\phi)\sin(i))\sin(a)+\sin(\phi)\cos(\theta)\cos(a),$$
$$\sin(\phi)\sin(\theta)\sin(i)+\cos(\phi)\cos(i)]]$$

> sigma[theta] := *Vector*([*B*[2, 1], *B*[2, 2], B[2, 3]])

$$\sigma_\theta := \begin{bmatrix} (-\cos(\phi)\sin(\theta)\cos(i)-\sin(\phi)\sin(i))\cos(a)-\cos(\phi)\cos(\theta)\sin(a) \\ (-\cos(\phi)\sin(\theta)\cos(i)-\sin(\phi)\sin(i))\sin(a)+\cos(\phi)\cos(\theta)\cos(a) \\ \cos(\phi)\sin(\theta)\sin(i)-\sin(\phi)\cos(i) \end{bmatrix} \quad (8)$$

> sigma[*z*] := *Vector*([*B*[3, 1], *B*[3, 2], B[3, 3]])

$$\sigma_z := \begin{bmatrix} (-\sin(\phi)\sin(\theta)\cos(i)+\cos(\phi)\sin(i))\cos(a)-\sin(\phi)\cos(\theta)\sin(a) \\ (-\sin(\phi)\sin(\theta)\cos(i)+\cos(\phi)\sin(i))\sin(a)+\sin(\phi)\cos(\theta)\cos(a) \\ \sin(\phi)\sin(\theta)\sin(i)+\cos(\phi)\cos(i) \end{bmatrix} \quad (9)$$

> *n* := *Vector*([sin(*i*[*w*])·cos(*a*[*w*]), sin(*i*[*w*])·sin(*a*[*w*]), cos(*i*[*w*])])

$$n := \begin{bmatrix} \sin(i_w)\cos(a_w) \\ \sin(i_w)\sin(a_w) \\ \cos(i_w) \end{bmatrix} \quad (10)$$

> cos(psi *r*) := *multiply*(*n*, sigma[*r*])

$$\cos(\psi r) := \sin(i_w)\cos(a_w)(\cos(\theta)\cos(i)\cos(a)-\sin(\theta)\sin(a)) \quad (11)$$
$$+\sin(i_w)\sin(a_w)(\cos(\theta)\cos(i)\sin(a)+\sin(\theta)\cos(a))-\cos(i_w)\cos(\theta)\sin(i)$$

> cos(psi theta) := *multiply*(*n*, sigma[theta])

$$\cos(\psi\theta) := \sin(i_w)\cos(a_w)((-\cos(\phi)\sin(\theta)\cos(i)-\sin(\phi)\sin(i))\cos(a) \quad (12)$$
$$-\cos(\phi)\cos(\theta)\sin(a))+\sin(i_w)\sin(a_w)((-\cos(\phi)\sin(\theta)\cos(i)$$
$$-\sin(\phi)\sin(i))\sin(a)+\cos(\phi)\cos(\theta)\cos(a))+\cos(i_w)(\cos(\phi)\sin(\theta)\sin(i)$$
$$-\sin(\phi)\cos(i))$$

> cos(psi z) := *multiply*(*n*, sigma[z])

$$\cos(\psi z) := \sin(i_w)\cos(a_w)((-\sin(\phi)\sin(\theta)\cos(i)+\cos(\phi)\sin(i))\cos(a) \quad (13)$$
$$-\sin(\phi)\cos(\theta)\sin(a))+\sin(i_w)\sin(a_w)((-\sin(\phi)\sin(\theta)\cos(i)$$
$$+\cos(\phi)\sin(i))\sin(a)+\sin(\phi)\cos(\theta)\cos(a))+\cos(i_w)(\sin(\phi)\sin(\theta)\sin(i)$$
$$+\cos(\phi)\cos(i))$$

> *with*(*LinearAlgebra*) :

> *s*[theta] := *CrossProduct*(sigma[theta], *n*)

$$s_\theta := [[((-\cos(\phi)\sin(\theta)\cos(i)-\sin(\phi)\sin(i))\sin(a)+\cos(\phi)\cos(\theta)\cos(a))\cos(i_w) \quad (14)$$
$$-(\cos(\phi)\sin(\theta)\sin(i)-\sin(\phi)\cos(i))\sin(i_w)\sin(a_w)],$$
$$[-((-\cos(\phi)\sin(\theta)\cos(i)-\sin(\phi)\sin(i))\cos(a)-\cos(\phi)\cos(\theta)\sin(a))\cos(i_w)$$

$$+\left(\cos(\phi)\sin(\theta)\sin(i)-\sin(\phi)\cos(i)\right)\sin(i_w)\cos(a_w)\Big],$$
$$\Big[\left(\left(-\cos(\phi)\sin(\theta)\cos(i)-\sin(\phi)\sin(i)\right)\cos(a)$$
$$-\cos(\phi)\cos(\theta)\sin(a)\right)\sin(i_w)\sin(a_w)-\left(\left(-\cos(\phi)\sin(\theta)\cos(i)$$
$$-\sin(\phi)\sin(i)\right)\sin(a)+\cos(\phi)\cos(\theta)\cos(a)\right)\sin(i_w)\cos(a_w)\Big]\Big]$$

> cos(Phi[theta]) = *multiply*(*s*[theta], sigma[*r*])

$$\cos(\Phi_\theta)=\left(\left(\left(-\cos(\phi)\sin(\theta)\cos(i)-\sin(\phi)\sin(i)\right)\sin(a)\right.\right. \tag{15}$$
$$+\cos(\phi)\cos(\theta)\cos(a)\Big)\cos(i_w)-\left(\cos(\phi)\sin(\theta)\sin(i)\right.$$
$$\left.-\sin(\phi)\cos(i)\right)\sin(i_w)\sin(a_w)\Big)\left(\cos(\theta)\cos(i)\cos(a)-\sin(\theta)\sin(a)\right)+\Big(-\big(\big($$
$$-\cos(\phi)\sin(\theta)\cos(i)-\sin(\phi)\sin(i)\big)\cos(a)-\cos(\phi)\cos(\theta)\sin(a)\big)\cos(i_w)$$
$$+\left(\cos(\phi)\sin(\theta)\sin(i)-\sin(\phi)\cos(i)\right)\sin(i_w)\cos(a_w)\Big)\left(\cos(\theta)\cos(i)\sin(a)\right.$$
$$+\sin(\theta)\cos(a)\Big)-\Big(\left(\left(-\cos(\phi)\sin(\theta)\cos(i)-\sin(\phi)\sin(i)\right)\cos(a)\right.$$
$$-\cos(\phi)\cos(\theta)\sin(a)\Big)\sin(i_w)\sin(a_w)-\left(\left(-\cos(\phi)\sin(\theta)\cos(i)\right.\right.$$
$$\left.\left.-\sin(\phi)\sin(i)\right)\sin(a)+\cos(\phi)\cos(\theta)\cos(a)\right)\sin(i_w)\cos(a_w)\Big)\cos(\theta)\sin(i)$$

> *simplify*(**(15)**, '*size*, *trig*')

$$\cos(\Phi_\theta)=-\sin(\theta)\cos(i)\sin(\phi)\sin(a)\sin(i_w)\sin(a_w) \tag{16}$$
$$-\sin(\theta)\cos(i)\sin(\phi)\cos(a)\sin(i_w)\cos(a_w)+\cos(\phi)\sin(i)\sin(a)\sin(i_w)\sin(a_w)$$
$$+\cos(\phi)\sin(i)\cos(a)\sin(i_w)\cos(a_w)-\sin(\phi)\sin(a)\cos(\theta)\sin(i_w)\cos(a_w)$$
$$+\sin(\phi)\cos(\theta)\cos(a)\sin(i_w)\sin(a_w)+\sin(\theta)\sin(\phi)\sin(i)\cos(i_w)$$
$$+\cos(\phi)\cos(i)\cos(i_w)$$

> $s[z] := \mathit{CrossProduct}(\text{sigma}[z], n)$

$$s_z := \Big[\Big[\left(\left(-\sin(\phi)\sin(\theta)\cos(i)+\cos(\phi)\sin(i)\right)\sin(a)+\sin(\phi)\cos(\theta)\cos(a)\right)\cos(i_w) \tag{17}$$
$$-\left(\sin(\phi)\sin(\theta)\sin(i)+\cos(\phi)\cos(i)\right)\sin(i_w)\sin(a_w)\Big],$$
$$\Big[-\left(\left(-\sin(\phi)\sin(\theta)\cos(i)+\cos(\phi)\sin(i)\right)\cos(a)-\sin(\phi)\cos(\theta)\sin(a)\right)\cos(i_w)$$
$$+\left(\sin(\phi)\sin(\theta)\sin(i)+\cos(\phi)\cos(i)\right)\sin(i_w)\cos(a_w)\Big],$$
$$\Big[\left(\left(-\sin(\phi)\sin(\theta)\cos(i)+\cos(\phi)\sin(i)\right)\cos(a)\right.$$
$$-\sin(\phi)\cos(\theta)\sin(a)\Big)\sin(i_w)\sin(a_w)-\left(\left(-\sin(\phi)\sin(\theta)\cos(i)\right.\right.$$
$$\left.\left.+\cos(\phi)\sin(i)\right)\sin(a)+\sin(\phi)\cos(\theta)\cos(a)\right)\sin(i_w)\cos(a_w)\Big]\Big]$$

> cos(Phi[*z*]) = *multiply*(*s*[z], sigma[*r*])

$$\cos(\Phi_z)=\left(\left(\left(-\sin(\phi)\sin(\theta)\cos(i)+\cos(\phi)\sin(i)\right)\sin(a)\right.\right. \tag{18}$$
$$+\sin(\phi)\cos(\theta)\cos(a)\Big)\cos(i_w)-\left(\sin(\phi)\sin(\theta)\sin(i)\right.$$
$$\left.+\cos(\phi)\cos(i)\right)\sin(i_w)\sin(a_w)\Big)\left(\cos(\theta)\cos(i)\cos(a)-\sin(\theta)\sin(a)\right)+\Big(-\big(\big($$
$$-\sin(\phi)\sin(\theta)\cos(i)+\cos(\phi)\sin(i)\big)\cos(a)-\sin(\phi)\cos(\theta)\sin(a)\big)\cos(i_w)$$

$$+\left(\sin(\phi)\sin(\theta)\sin(i)+\cos(\phi)\cos(i)\right)\sin(i_w)\cos(a_w)\Big)\left(\cos(\theta)\cos(i)\sin(a)\right.$$
$$\left.+\sin(\theta)\cos(a)\right)-\Big(\left(\left(-\sin(\phi)\sin(\theta)\cos(i)+\cos(\phi)\sin(i)\right)\cos(a)\right.$$
$$\left.-\sin(\phi)\cos(\theta)\sin(a)\right)\sin(i_w)\sin(a_w)-\left(\left(-\sin(\phi)\sin(\theta)\cos(i)\right.\right.$$
$$\left.\left.+\cos(\phi)\sin(i)\right)\sin(a)+\sin(\phi)\cos(\theta)\cos(a)\right)\sin(i_w)\cos(a_w)\Big)\cos(\theta)\sin(i)$$

> *simplify*(**(18)**, '*size*, *trig*')

$$\cos(\Phi_z)=\cos(\phi)\sin(\theta)\cos(i)\sin(a)\sin(i_w)\sin(a_w) \tag{19}$$
$$+\cos(\phi)\sin(\theta)\cos(i)\cos(a)\sin(i_w)\cos(a_w)$$
$$+\cos(\phi)\sin(a)\cos(\theta)\sin(i_w)\cos(a_w)-\cos(\phi)\cos(\theta)\cos(a)\sin(i_w)\sin(a_w)$$
$$+\sin(\phi)\sin(i)\sin(a)\sin(i_w)\sin(a_w)+\sin(\phi)\sin(i)\cos(a)\sin(i_w)\cos(a_w)$$
$$-\cos(\phi)\sin(\theta)\sin(i)\cos(i_w)+\cos(i)\sin(\phi)\cos(i_w)$$

Appendix C Matlab scripts

C.1 Failure criteria comparison procedure

```
%INPUT
Sig=[Sig1 Sig2 Sig3 Sig4 Sig5]
Pconf=[Pconf1 Pconf2 Pconf3 Pconf4 Pconf5]

%STRENGHT COMPARISON
%CAZACU
FigHandle = figure('Position', [120, 100, 920, 1000]);
subplot(3,2,1)
STR=sprintf('%s ', Rock{:})
annotation('textbox',[0.135 0.85 0.4 0.15],'String',STR,'EdgeColor','none');
Cazacuprocedure_shearstrength
annotation('textbox',[0.67 0.75 0.3 0.15],'String',{['X_t = ' num2str(Xt) ' MPa'],...
    ['Y_t = ' num2str(Yt)  ' MPa'],['X_c = ' num2str(Xc)  ' MPa'],...
    ['Y_c = ' num2str(Yc)  ' MPa'],['c = ' num2str(c)  ' MPa^{-1}'],...
    ['RSS = ' num2str(RSS) ' MPa^2'],['M = ' num2str(mismatch1) ' MPa^2']},...
    'EdgeColor','none');
set(hleg1, 'Position',[0.52 0.76 0.1 0.1])

%MCLAMORE AND GRAY
m=1
n=1
subplot(3,2,3)
McLamoreGrayprocedure_shearstrength
annotation('textbox', [0.67 0.47 0.3 0.15], 'String',{['A_1 = ' num2str(A1)] ;...
    ['B_1 = ' num2str(B1)] ; ['C_1 = ' num2str(C1)];['D_1 = ' num2str(D1)];...
    ['A_2 = ' num2str(A2)];['B_2 = ' num2str(B2)];['C_2 = ' num2str(C2)];...
    ['D_2 = ' num2str(A2)];['m = ' num2str(m)];['n = ' num2str(n)];...
    ['RSS = ' num2str(RSS2) ' MPa^2'];['M = ' num2str(mismatch2) ' MPa^2']},...
    'EdgeColor','none')
set(hleg2, 'Position',[0.52 0.46 0.1 0.1])

%PATCHY WEAKNESS
subplot(3,2,5)
Patchyweaknessprocedure_shearstrength
annotation('textbox',  [0.67 0.13 0.3 0.15], 'String',...
    {['S_0 = ' num2str(Tau0) ' MPa']; ['\phi = ' num2str(phi*180/pi) '\circ'] ;...
    ['S_{0w} = ' num2str(Tau0w) ' MPa'];['\phi_w = ' num2str(phiw*180/pi) '\circ'];...
    ['\eta_0 = ' num2str(eta0)];['\sigma_c = ' num2str(Sc) ' MPa'];...
    ['RSS = ' num2str(RSS3) ' MPa^2'];['M = ' num2str(mismatch3) ' MPa^2']},...
    'EdgeColor','none')
set(hleg3, 'Position',[0.52 0.16 0.1 0.1]);
export_fig('C:\Users\thopaz\Dropbox\Masteroppg\Figs\GRS1results.pdf', '-pdf','-transparent')
```

C.2 Cazacu's model

```
%CAZACU'S MODEL
thetaactual=theta1/180*pi

%INPUT VALUES
syms theta
sigma1=Pconf(1,:); %SIGMA1=MINOR PRINCIPAL STRESS IN THE CAZACU MODEL

%EXCEL PARAMETER INPUT
Xc=124.294607
Yc=226.5253152
Xt=0.00735678
Yt=0.001891737
c=1.377929509

%CRITERION
[y]= @(theta) Cazacu_criterion(theta,Xt,Yt,Xc,Yc,c,sigma1);

%PLOT
hold on
title('Cazacu et al.')
xlabel('\theta [\circ]');
ylabel('\sigma_1 [MPa]');
set(gca,'xTick',0:pi/12:0.5*pi)
set(gca,'xTickLabel',{'0', '15', '30', '45', '60', '75', '90'})
plot(0.5*pi-thetaactual, Sig(:,5),'sk','markers',5)
plot(0.5*pi-thetaactual, Sig(:,4),'vk','markers',5)
plot(0.5*pi-thetaactual, Sig(:,3),'xk','markers',5)
plot(0.5*pi-thetaactual, Sig(:,2),'dk','markers',5)
plot(0.5*pi-thetaactual, Sig(:,1),'ok','markers',5)
hleg1 = legend(['\sigma_3 = ' num2str(Pconf(1,5)) ' MPa'],...
                ['\sigma_3 = ' num2str(Pconf(1,4)) ' MPa'],...
                ['\sigma_3 = ' num2str(Pconf(1,3)) ' MPa'],...
                ['\sigma_3 = ' num2str(Pconf(1,2)) ' MPa'],...
                ['\sigma_3 = ' num2str(Pconf(1,1)) ' MPa'])
legend('boxoff')
fplot(y, [0 0.5*pi],'k');
axis tight
hold off

i=1
while i<=size(Pconf,2)
sigma1=Pconf(1,i)
theta=thetaactual;
[y1]=Cazacu_criterionresiduals(theta,Xt,Yt,Xc,Yc,c,sigma1);
i=i+1
end
```

```
%RSS AND m DATA FROM EXCEL
[r u]=size(Sig)
RSS=2346
mismatch1=2760
```

C.3 McLamore & Gray's model

```
%MCLAMORE AND GRAY'S MODEL
thetaactual=theta1/180*pi
i=1
while i<=size(thetaactual,1)
y=[Sig(i,:)];
x=[Pconf(i,:)];
%LINEAR REGRESSION FOR TAU0 AND TANPHI
p=polyfit(x,y,1)
a=(p(1)-1)/(p(1)+1)
alpha=asin(a)
tanphi(i,1)=tan(alpha)
beta=(pi/4)+alpha/2
Tau0(i,1)=p(2)/(2*tan(beta))
i=i+1;
end

%GLOBAL MINIMUM TAU0 AND TANPHI VALUES AND CORRESPONDING THETA VALUES
[M1, Indices1] = min(Tau0);
[M2, Indices2] = min(tanphi);
Theta_minTau0=thetaactual(Indices1)
Theta_mintanphi=thetaactual(Indices2)

%DEFINING RANGES FOR THE VARIATION LAWS
Tau0A1B1=Tau0(1:Indices1)
ThetaA1B1=thetaactual(1:Indices1)

Tau0A2B2=Tau0(Indices1+1:length(thetaactual))
ThetaA2B2=thetaactual(Indices1+1:length(thetaactual))

tanphiC1D1=tanphi(1:Indices2)
ThetaC1D1=thetaactual(1:Indices2)

tanphiC2D2=tanphi(Indices2+1:length(thetaactual))
ThetaC2D2=thetaactual(Indices2+1:length(thetaactual))

%LINEFITTING USING LSQ
f1 = fittype('A1-B1*cos(2*(Theta_minTau0-ThetaA1B1))^n','coefficients',{'A1','B1'},...
    'problem',{'Theta_minTau0','n'},'independent','ThetaA1B1','dependent',...
    {'Tau0A1B1'})
```

```
[fitresult] = fit( ThetaA1B1, Tau0A1B1, f1,'problem',{Theta_minTau0,n})
Parameterset1 = coeffvalues(fitresult)
A1=Parameterset1(1)
B1=Parameterset1(2)

f2 = fittype('A2-B2*cos(2*(Theta_minTau0-ThetaA2B2))^n','coefficients',{'A2','B2'},...
            'problem',{'Theta_minTau0','n'},'independent','ThetaA2B2','dependent',...
            {'Tau0A2B2'})
[fitresult] = fit( ThetaA2B2, Tau0A2B2, f2,'problem',{Theta_minTau0,n})
Parameterset1 = coeffvalues(fitresult)
A2=Parameterset1(1)
B2=Parameterset1(2)

f3 = fittype('C1-D1*cos(2*(Theta_mintanphi-ThetaC1D1))^m','coefficients',{'C1','D1'},...
            'problem',{'Theta_mintanphi','m'},'independent','ThetaC1D1','dependent',...
            {'tanphiC1D1'})
[fitresult] = fit( ThetaC1D1, tanphiC1D1, f3,'problem',{Theta_mintanphi,m})
Parameterset1 = coeffvalues(fitresult)
C1=Parameterset1(1)
D1=Parameterset1(2)

f4 = fittype('C2-D2*cos(2*(Theta_mintanphi-ThetaC2D2))^m','coefficients',{'C2','D2'},...
           'problem',{'Theta_mintanphi','m'},'independent','ThetaC2D2','dependent',...
           {'tanphiC2D2'})
[fitresult] = fit( ThetaC2D2, tanphiC2D2, f4,'problem',{Theta_mintanphi,m})
Parameterset1 = coeffvalues(fitresult)
C2=Parameterset1(1)
D2=Parameterset1(2)

%RSS AND m DATA FROM EXCEL
[r u]=size(Sig)
RSS2=337.0
mismatch2=465.0

i=1
while i<=size(Pconf,2)
sigma3=Pconf(1,i)

if Indices1>Indices2
    Index1=Indices2;
    Index2=Indices1
else
    Index1=Indices1
    Index2=Indices2
end

%CRITERIA
a= thetaactual(1:Index1);
[y1]= McLamoreGray1( A1,B1,C1,D1,Theta_minTau0,Theta_mintanphi,m,n,a,sigma3 );
```

```
b=thetaactual(Index1+1:Index2);
[y2]= McLamoreGray2( A2,B2,C1,D1,b,Theta_minTau0,Theta_mintanphi,m,n,sigma3 );

cc=thetaactual(Index2+1:(length(thetaactual)));
[y3]= McLamoreGray3( A2,B2,C2,D2,cc,Theta_minTau0,Theta_mintanphi,m,n,sigma3 );

%PLOT MODEL
hold all
title('McLamore & Gray')
xlabel('\theta [\circ]');
ylabel('\sigma_1 [MPa]');
set(gca,'xTick',0:15:90)
set(gca,'xTickLabel',{'0', '15', '30', '45', '60', '75', '90'})

%PLOT EXPERIMENTAL DATA
theta2=90-theta1
t = 0:0.1:90;
ymod=[y1 ; y2 ; y3]
yy = spline(theta2,ymod,t);

plot(theta2, Sig(:,5),'sk','markers',5)
plot(theta2, Sig(:,4),'vk','markers',5)
plot(theta2, Sig(:,3),'xk','markers',5)
plot(theta2, Sig(:,2),'dk','markers',5)
plot(theta2, Sig(:,1),'ok','markers',5)
hleg2 = legend(['\sigma_3 = ' num2str(Pconf(1,5)) ' MPa'],...
                ['\sigma_3 = ' num2str(Pconf(1,4)) ' MPa'],...
                ['\sigma_3 = ' num2str(Pconf(1,3)) ' MPa'],...
                ['\sigma_3 = ' num2str(Pconf(1,2)) ' MPa'],...
                ['\sigma_3 = ' num2str(Pconf(1,1)) ' MPa'])
plot(t,yy,'k')
hold off
axis tight
i=i+1;
end
legend('boxoff')
```

C.4 Fjær & Nes's model

```
%FJAER AND NES' MODEL
thetaactual=0.5*pi-theta1/180*pi

%INPUT FROM EXCEL
Tau0=51.2297482094593
phi=0.52715954
Tau0w=28.3937297534755
phiw=0.570641062
```

```
eta0=0.0758841161825443
Sc=1123365.56503954

syms theta
i=1
while i<=size(Pconf,2)
sigma3=Pconf(1,i)
eta=eta0*exp(-sigma3/Sc)
%INTRINSIC CRITERION
[y1]=@(theta) Patchy_intrinsic( Tau0,phi,eta,theta,sigma3 )
%WEAKPLANE CRITERION
[y2]=@(theta) Patchy_weakplane( Tau0w,phiw,eta,theta,sigma3)

%FIND INTERSECTIONS BETWEEN INTRINSIC AND WP-CRITERIA
Intersection=double(solve(Patchy_intrinsic(Tau0,phi,eta,theta,sigma3)...
            ==Patchy_weakplane(Tau0w,phiw,eta,theta,sigma3),'Real',true))

%PLOT EXPERIMENTAL DATA
title('Fjaer & Nes')
xlabel('\theta [\circ]');
ylabel('\sigma_1 [MPa]');
hold all
set(gca,'xTick',0:pi/12:0.5*pi)
set(gca,'xTickLabel',{'0', '15', '30', '45', '60', '75', '90'})
thetaactual=0.5*pi-theta1*pi/180
plot(thetaactual, Sig(:,5),'sk','markers',5)
plot(thetaactual, Sig(:,4),'vk','markers',5)
plot(thetaactual, Sig(:,3),'xk','markers',5)
plot(thetaactual, Sig(:,2),'dk','markers',5)
plot(thetaactual, Sig(:,1),'ok','markers',5)
hleg3 = legend(['\sigma_3 = ' num2str(Pconf(1,5)) ' MPa'],...
    ['\sigma_3 = ' num2str(Pconf(1,4)) ' MPa'],...
    ['\sigma_3 = ' num2str(Pconf(1,3)) ' MPa'],...
    ['\sigma_3 = ' num2str(Pconf(1,2)) ' MPa'],...
    ['\sigma_3 = ' num2str(Pconf(1,1)) ' MPa'])
legend('boxoff')

%PLOT LOWEST PREDICTED VALUE OF INTRINSIC AND WP-CRITERIA
if isempty(Intersection)==1
    fplot(y1, [0 0.5*pi],'k')
else
    fplot(y1, [0 Intersection(2)],'k');
    fplot(y2, [Intersection(2)  Intersection(1)],'k');
    fplot(y1, [Intersection(1) 0.5*pi],'k');
end

axis tight
hold off
%RSS CALCULATIONS
flip=flipud(thetaactual)
```

```
a=flip([1 2 3 4 6 7 8])
%INTRINSIC CRITERION
y1=sigma3+2*(1-eta0*exp(-sigma3/Sc).*sin(2*a).^2)*(Tau0*cos(phi)...
    +sigma3*sin(phi))/(1-sin(phi));
residuals1=(y1-Sig([8 7 6 5 3 2 1],i)).^2;

b=flip([ 5]);
%WEAKPLANE CRITERION
y2=sigma3+2*(1-eta0*exp(-sigma3/Sc).*sin(2*b).^2)*(Tau0w*cos(phiw)+sigma3*sin(phiw))./...
    (sin(2*b)*cos(phiw)-(cos(2*b)+1)*sin(phiw));
residuals2=(y2-Sig([ 4],i)).^2;
rss=[residuals1;residuals2]
residuals(i,1)=sum(rss)
i=i+1;
end

%RSS AND m DATA FROM EXCEL
[r u]=size(Sig)
RSS3=217.7
mismatch3=263.9
```

C.5 Stiffness models comparison procedure

```
%STIFFNESS COMPARISON

%BACKUS STIFFNESS
FigHandle = figure('Position', [100, 100, 920, 1000]);
subplot(3,2,1)
STR=sprintf('%s ', Rock{:})
annotation('textbox',[0.135 0.85 0.4 0.15],'String',STR,'EdgeColor','none');
Backus_stiffness
annotation('textbox', [0.50 0.75 0.3 0.15], 'String',{['G_1 = ' num2str(G1) ' GPa'];...
    ['\lambda_1 = ' num2str(lambda1) ' GPa'] ;  ['x = ' num2str(x)] ;...
    ['f = ' num2str(f)];['g = ' num2str(g)];['f = ' num2str(f)];...
    ['RSS = ' num2str(RSS1) ' GPa^2'];['M = ' num2str(m1) ' GPa^2'] },'EdgeColor','none')


%PLANE OF PATCHY WEAKNESS STIFFNESS
subplot(3,2,3)
Patchyweakness_stiffness
annotation('textbox',[0.5 0.43 0.3 0.15],'String',{['E_0 = ' num2str(E0) ' GPa'],...
    ['\rho = ' num2str(rho)],['\eta_0 = ' num2str(eta)],['RSS = ' num2str(RSS2) ' GPa^2'],...
    ['M = ' num2str(m2) ' GPa^2']},'EdgeColor','none');
hold off

export_fig('C:\Users\thopaz\Dropbox\Masteroppg\Figs\GRS1resultsstiffness', '-pdf','-transparent')
```

C.6 Backus' model

```
%BACKUS' STIFFNESS MODEL

%INPUT FROM EXCEL
f    =0.32179304
g    =0.53463641
x    =0.853729547
lambda1 =0
G1   =13.94026332
RSS1=32.30
m1=8.074



syms theta
%MODEL
[Eeff]=@(theta) Backus_stiffness_criterion(G1,lambda1,theta,x,f,g )
%PLOT
hold all
title('Backus')
xlabel('\theta [\circ]');
ylabel('Young`s modulus [GPa]');
set(gca,'xTick',0:1/12*pi:0.5*pi)
set(gca,'xTickLabel',{'0', '15', '30', '45', '60', '75', '90'})
fplot(Eeff,[0 0.5*pi],'k')
theta=theta2./180.*pi;
plot(theta,Ei,'xk')
```

C.7 Fjær & Nes' model

```
%INPUT
E0=Ei(size(Ei,1))
theta=theta2/180*pi

%PARAMETER INPUT FROM EXCEL
eta=0.075884116
rho=0.176536517
RSS2=4.003
m2=8.006

syms theta
%STIFFNESS CRITERION
[y3]=@(theta) Patchy_stiffness( eta, theta, rho, E0 );
```

```
%FIGURE
hold all
title('Fj\ae r & Nes')
xlabel('\theta [\circ]')
ylabel('Young`s modulus [GPa]')
set(gca,'xTick',0:1/12*pi:0.5*pi)
set(gca,'xTickLabel',{'0', '15', '30', '45', '60', '75', '90'})
fplot(y3, [0 pi/2],'k')
theta=theta2/180*pi
plot(theta,Ei,'xk')
axis tight
```

Appendix D Strength and stiffness anisotropy data

Green River shale 1
McLamore & Gray

Extrapolated data

beta [deg]	Sig1 [MPa]	Sig3 [MPa]
0	195.9137	0
15	160.9921	0
20	135.8851	0
30	92.1557	0
45	157.1918	0
60	159.613	0
75	155.5814	0
90	173.5632	0

beta [deg]	Sig1-Sig3 [psi]	Sig1-Sig3 [MPa]	Sig1 [MPa]	Sig3 [MPa]
0	28767.45277	198.3446044	205.2393617	6.89475728
15	21486.0756	148.1412762	155.0360335	6.89475728
20	19161.20834	132.1118807	139.006638	6.89475728
30	13433.67571	92.62193339	99.51669067	6.89475728
45	23231.42784	160.1750562	167.0698135	6.89475728
60	23640.31041	162.9942023	169.8889596	6.89475728
75	22820.27622	157.3402656	164.2350229	6.89475728
90	24768.4814	170.7726675	177.6674247	6.89475728
0	39383.42384	271.5391483	306.0129347	34.4737864
15	35330.90293	243.5980002	278.0717866	34.4737864
20	31008.81904	213.7982808	248.2720672	34.4737864
30	25434.22028	175.3627754	209.8365618	34.4737864
45	31691.80268	218.5072873	252.9810737	34.4737864
60	32410.18349	223.4603486	257.934135	34.4737864
75	32666.13218	225.2250527	259.6988391	34.4737864
90	35385.3601	243.9734692	278.4472556	34.4737864
0	49075.4383	338.3632355	407.3108083	68.9475728
15	46100.71551	317.8532439	386.8008167	68.9475728
20	43161.38987	297.587307	366.5348798	68.9475728
30	37741.54023	260.2187593	329.1663321	68.9475728
45	43382.84902	299.1142141	368.0617869	68.9475728
60	46101.16932	317.8563728	386.8039456	68.9475728
75	45743.56725	315.3907933	384.3383661	68.9475728
90	47231.15555	325.6473536	394.5949264	68.9475728
0	59845.25088	412.6184792	516.0398384	103.4213592
15	56564.66032	389.9996036	493.4209628	103.4213592
20	53776.45333	370.7755931	474.1969523	103.4213592
30	48512.26043	334.4802608	437.90162	103.4213592
45	56153.50871	387.164813	490.5861722	103.4213592
60	55333.47452	381.5108763	484.9322355	103.4213592
75	56359.53832	388.5853372	492.0066964	103.4213592
90	58000.06051	399.8963394	503.3176987	103.4213592
0	77537.02331	534.598956	706.967888	172.368932
15	71947.90264	496.0633256	668.4322576	172.368932
20	71008.5165	489.5864861	661.9554181	172.368932
30	68511.65535	472.3712345	644.7401665	172.368932
45	69230.03615	477.3242958	649.6932278	172.368932
60	72256.03945	498.1878541	670.5567861	172.368932
75	73280.28802	505.2497993	677.6187313	172.368932
90	73229.46133	504.8993616	677.2682936	172.368932

Green River shale 2
McLamore & Gray

Extrapolated data

beta [deg]	Sig1 [MPa]	Sig3 [MPa]
0	134.3827	0
10	122.4101	0
20	100.3311	0
30	82.0214	0
40	90.7299	0
60	111.961	0
90	118.5815	0

beta [deg]	Sig1-Sig3 [psi]	Sig1-Sig3 [MPa]	Sig1 [MPa]	Sig3 [MPa]
0	20515.95667	141.4525416	148.3472989	6.89475728
10	18007.05147	124.1542492	131.0490065	6.89475728
20	15175.74149	104.6330542	111.5278114	6.89475728
30	12473.10265	85.99901528	92.89377256	6.89475728
40	13770.89997	94.94701283	101.8417701	6.89475728
60	16558.95609	114.1699831	121.0647403	6.89475728
90	17677.55888	121.8824778	128.7772351	6.89475728
0	24386.99477	168.1424097	202.6161961	34.4737864
10	22329.71067	153.9579352	188.4317216	34.4737864
20	19562.55452	134.8790652	169.3528516	34.4737864
30	16472.9936	113.5772926	148.051079	34.4737864
40	17706.09189	122.0792059	156.5529923	34.4737864
60	20688.24513	142.6404287	177.1142151	34.4737864
90	22322.98633	153.9115725	188.3853589	34.4737864
0	30967.75952	213.5151854	282.4627582	68.9475728
10	28459.03606	196.218146	265.1657188	68.9475728
20	24659.60308	170.0219779	238.9695507	68.9475728
30	20602.1009	142.0464852	210.994058	68.9475728
40	22931.99331	158.1105278	227.0581006	68.9475728
60	26494.98401	182.6764839	251.6240567	68.9475728
90	28129.17999	193.9438686	262.8914414	68.9475728
0	36645.10032	252.6590722	356.0804314	103.4213592
10	33684.574	232.2469618	335.6683211	103.4213592
20	30336.94388	209.1658647	312.5872239	103.4213592
30	25311.68218	174.517905	277.9392642	103.4213592
40	27963.97935	192.8048502	296.2262094	103.4213592
60	31527.15179	217.3720593	320.7934185	103.4213592
90	33032.31317	227.7497817	331.1711409	103.4213592
0	46516.06572	320.7169828	493.0859148	172.368932
10	41426.65019	285.626698	457.99563	172.368932
20	39111.11515	269.6616459	442.0305779	172.368932
30	33505.56121	231.0127121	403.3816441	172.368932
40	36287.07473	250.1905727	422.5595047	172.368932
60	39204.71067	270.3069643	442.6758963	172.368932
90	42451.8392	292.6951274	465.0640594	172.368932

Tournemire shale
Niandou et al.

Extrapolated data

beta [deg]	Sig1 [MPa]	Sig3 [MPa]
0	53.2125	0
10	51.718	0
20	45.7116	0
30	39.0123	0
45	35.3559	0
60	39.6572	0
70	44.78	0
80	48.9352	0
90	54.2941	0

beta [deg]	Sig1 [MPa]	Sig3 [MPa]
0	58.56065333	5
10	56.7306921	5
20	51.10744686	5
30	45.27329649	5
45	42.00309729	5
60	45.27095682	5
70	49.76915192	5
80	54.05844735	5
90	60.45478854	5
0	102.6378181	20
10	99.96523909	20
20	93.28646553	20
30	83.23421275	20
45	78.4876777	20
60	84.49830652	20
70	94.68993716	20
80	100.2446633	20
90	105.1636659	20
0	136.1687241	40
10	128.8592406	40
20	120.282321	40
30	114.4471679	40
45	109.7006328	40
60	113.3903026	40
70	129.0664691	40
80	134.8310976	40
90	144.1801105	40
0	155.1511877	50
10	150.7913677	50
20	144.9562146	50
30	134.9039619	50
45	130.579237	50
60	134.6907171	50
70	146.3596863	50
80	153.3907483	50
90	161.0515174	50

Mancos shale

Fjær & Nes

theta [deg]	Sig1 [MPa]	Sig3 [MPa]
0	63.73333333	0
15	64.5	0
30	54.6	0
45	47.5	0
53	38.4	0
60	46.15	0
75	54.2	0
90	65.13333333	0

theta = 0 deg

Sig1 [MPa]	Sig3 [MPa]
63.73333333	0
67.5	2
88.5	7
98.9	12

theta = 90 deg

Sig1 [MPa]	Sig3 [MPa]
66.2	0
72.2	2
98	7
82.2	10
111.7	12

theta = 52 deg

Sig1 [MPa]	Sig3 [MPa]
53.9	7
70.9	12
67.9	12

theta = 54 deg

Sig1 [MPa]	Sig3 [MPa]
44.6	2

Laminated mudstone

Attewell & Farmer

beta [deg]	Sig1-Sig3 [MPa]	Sig1 [MPa]	Sig3 [MPa]
0	37.21611722	37.21611722	0
15	23.15018315	23.15018315	0
30	14.06593407	14.06593407	0
45	19.04761905	19.04761905	0
60	27.25274725	27.25274725	0
75	38.24175824	38.24175824	0
90	50.10989011	50.10989011	0
0	47.32600733	51.22600733	3.9
15	38.82783883	42.72783883	3.9
30	30.62271062	34.52271062	3.9
45	36.19047619	40.09047619	3.9
60	40	43.9	3.9
75	49.67032967	53.57032967	3.9
90	59.04761905	62.94761905	3.9
0	68.86446886	78.66446886	9.8
15	62.12454212	71.92454212	9.8
30	50.10989011	59.90989011	9.8
45	59.19413919	68.99413919	9.8
60	65.64102564	75.44102564	9.8
75	76.04395604	85.84395604	9.8
90	84.98168498	94.78168498	9.8
0	102.2710623	122.2710623	20
15	87.91208791	107.9120879	20
30	72.57631258	92.57631258	20
45	90.84249084	110.8424908	20
60	106.0805861	126.0805861	20
75	114.2857143	134.2857143	20
90	127.6190476	147.6190476	20
0	114.8717949	146.8717949	32
15	109.5970696	141.5970696	32
30	99.04761905	131.047619	32
45	116.6300366	148.6300366	32
60	128.3516484	160.3516484	32
75	135.6776557	167.6776557	32
90	141.8315018	173.8315018	32
0	132.1611722	175.1611722	43
15	123.3699634	166.3699634	43
30	119.2673993	162.2673993	43
45	130.6959707	173.6959707	43
60	139.4871795	182.4871795	43
75	149.4505495	192.4505495	43
90	160.5860806	203.5860806	43

Green River shale 1
McLamore & Gray

beta [deg]	E-modulus [GPa]
0	25.08225229
15	24.61406392
20	20.03128576
30	20.65667607
45	20.18763334
60	22.80367859
75	21.26156177
90	19.98685912

Green River shale 2
McLamore & Gray

beta [deg]	E-modulus [GPa]
0	11.53554637
10	8.941714439
20	8.494030666
30	6.170175968
40	6.529006473
60	7.377384309
90	8.98784979

Tournemire shale
Niandou et al.

beta [deg]	E-modulus [GPa]
0	33.85496435
30	20.14235182
45	16.94532644
60	15.11866004
90	12.68057619

DATA AVERAGED FOR THE DIFFERENT CONFINING PRESSURES

Mancos shale
Fjær & Nes

theta [deg]	E-modulus [GPa]
0	18
0	18.4
15	20.8
30	19.1
45	18.4
45	20.3
60	21.6
60	21.4
75	24.3
90	28.9
90	25
90	26.4

DATA FROM UNIAXIAL LOADING CONDITIONS